Study of undoped and doped vanadium oxides for application in solid oxide fuel cell (SOFC)

A

Thesis

Submitted for the partial fulfilment

of the requirements for the award of degree of

Doctor of Philosophy

By

Savidh Khan

(Registration No. 901512007)

Under the supervision of

Dr. Kulvir Singh

(Professor & Head)

THAPAR INSTITUTE
OF ENGINEERING & TECHNOLOGY
(Deemed to be University)

School of Physics and Materials Science
Thapar Institute of Engineering & Technology,
Patiala-147004 (Punjab), India

(Deemed to be University)

(2021)

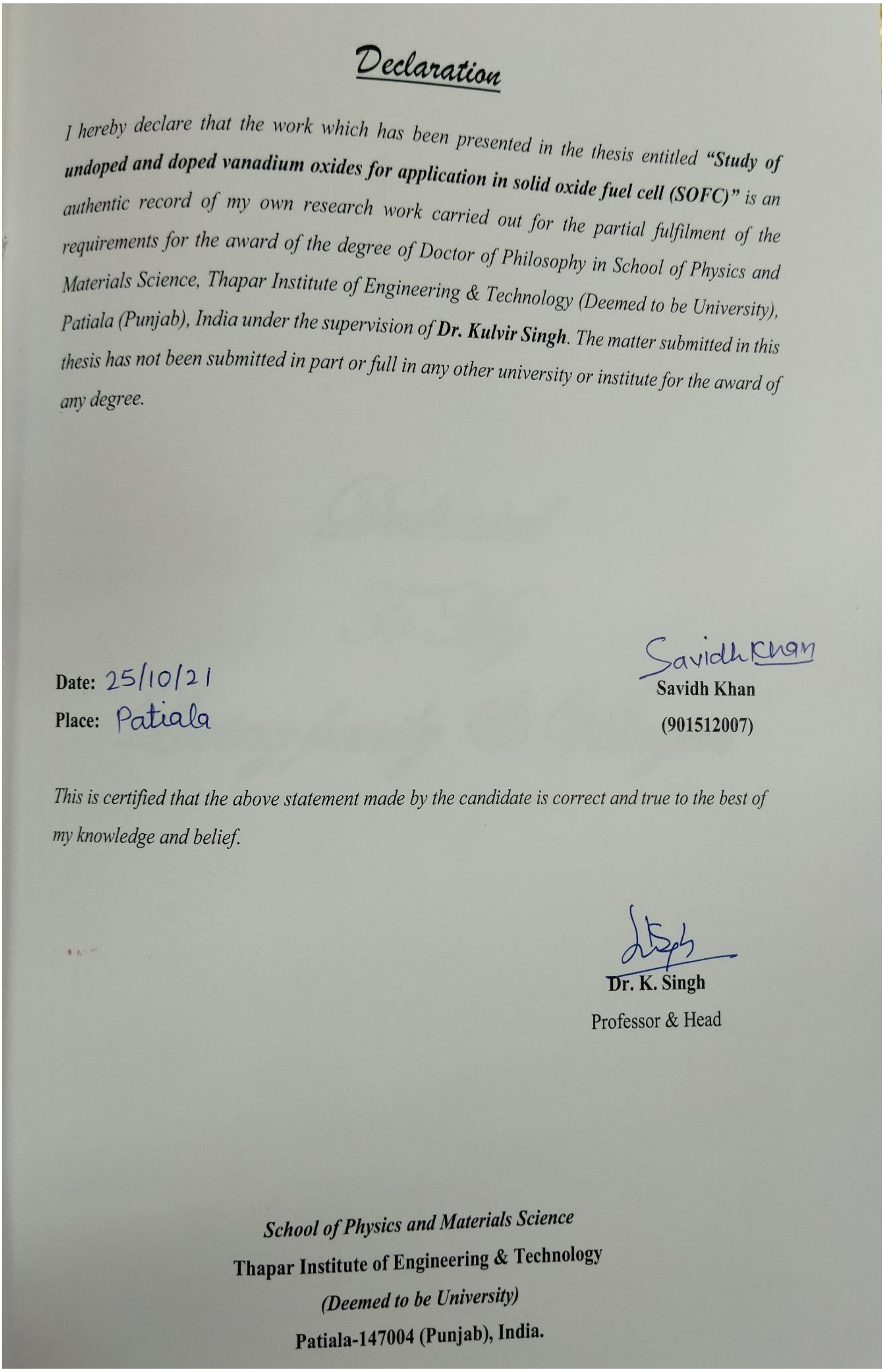

Declaration

I hereby declare that the work which has been presented in the thesis entitled ***"Study of undoped and doped vanadium oxides for application in solid oxide fuel cell (SOFC)"*** *is an authentic record of my own research work carried out for the partial fulfilment of the requirements for the award of the degree of Doctor of Philosophy in School of Physics and Materials Science, Thapar Institute of Engineering & Technology (Deemed to be University), Patiala (Punjab), India under the supervision of* **Dr. Kulvir Singh**. *The matter submitted in this thesis has not been submitted in part or full in any other university or institute for the award of any degree.*

Savidh Khan

Date: 25/10/21

Place: Patiala

Savidh Khan

(901512007)

This is certified that the above statement made by the candidate is correct and true to the best of my knowledge and belief.

Dr. K. Singh

Professor & Head

School of Physics and Materials Science

Thapar Institute of Engineering & Technology

(Deemed to be University)

Patiala-147004 (Punjab), India.

Dedicated

To My

Loving family & Villagers

Acknowledgement

The Doctorate of Philosophy is a journey of lifetime where not only intellectual, but spiritual as well as emotional grooming of the being is accomplished. This realization is incomplete without the surrounding aura of the magnificent people around you, who contribute in one way or the other to nurture you into a better person. This day has arrived after immense waiting that I got the opportunity to express my gratitude towards everyone who stood by my side in the course of this realization.

First and foremost, I am deeply indebted to my supervisor, ***Dr. Kulvir Singh****, who have guided me through the ups and downs in this entire journey of never-ending learning. The deep understanding, motivation and personal attention of my supervisor has provided a smooth base throughout the tenure of PhD. He helped me to bestow a better shape to my complete work into a dissertation.* ***Dr. Kulvir Singh,*** *my Guruji, like a father has always motivated me towards a better understanding of the concepts and problems through his solution-oriented techniques. His noble thoughts and conviction have led me to perform well throughout my journey.*

The track to my doctorate glazed with the financial assistance from direct-SRF Scheme ***(09/677(0037)-2019-EMR-I)****, Council of Scientific & Industrial Research, Govt. of India. Help from various research and academic institutions is highly acknowledged which provided their facilities to carry out the characterisation of materials such as* ***Panjab University, IIT Roorkee and IIT Bombay.***

I take the privilege to thank ***Dr. Prakash Gopalan*** *(Director), Thapar Institute of Engineering & Technology, Patiala for providing me resources in the institution and needful help during various stages of my work. I am thankful to* ***Dr. Rafat Siddique*** *(Dean R&SP) and* ***Dr. O.P. Pandey*** *(HSPMS) for their whole-hearted support and blessings. I thank my IRB Committee members,* ***Dr. O.P. Pandey, Dr. H. Bhunia and Dr. B.C. Mohanty*** *for their helpful suggestions and comments during my progress presentations. I whole-heartedly thank* ***Dr. Manoj Kumar Sharma****,* ***Dr. Bhupendra Chudasama, Dr. D.P. Singh, Dr. Somendu Jana, Dr. Poonam Uniyal, Dr. Jayant Kolte*** *and all the faculty members of SPMS for their timely help, guidance and moral support through different phases of this journey.*

I sincerely thank ***Mr. Purshottam Kumar Singh*** *for his valuable suggestions and help at the technical front of sample preparation and characterization. A special word of thanks goes to* ***Mr. Pardeep Kumar, Mr. Vijay, Ms. Neelam Sadana, Mr. Jant Singh, Mr. Indermani Mishra, Mr. S.P. Verma, Mr. Lalji Verma*** *and* ***Ms. Amandeep Kaur*** *for their valuable official and technical support.* ***Ms. Era, Mr. Ghamshyam Maurya, Mr. Mukesh Aggarwal*** *and* ***Mr. Pardeep Bhatia*** *of SAI Labs, TIET, Patiala for their help and services in carrying out the characterizations.*

I specially thank **Mr. Sameeruddin** and **Mrs. Reshma** for their constant moral support and motivation. I cannot forget the motivation and passion for research instilled in me by **Virender Singh,** and **Dr. Lalit Kumar,** which gave me the courage to begin this journey. Their blessings and zeal for hard work has always enlightened my path.

I express my immense gratitude towards my seniors and mentors **Dr. Gurbinder Kaur** and **Dr. Satwinder Singh** for holding my hand while taking initial steps to the world of research with their moral support and guidance in developing attitude for research. **Dr. Pooja Singla, Dr. Parveen Jha** and **Dr. Devender Kumar** have always provided their guidance in difficult situations evolving through this journey.

This journey of dissertation would have been terrible without the unlimited support, valuable discussions and suggestions from my sister and colleagues **Km. Abida, Neetu Bansal, Gaurav Sharma and Santhosh Kumar Mahadevan.** Without their help this work could never be completed.

I would like to thank **Shivani Punj, Paramvir Kaur, Manmeet Kaur, Trisha Walia, Taranvir Kaur** and **Vimi Dua** for creating a conducive environment in the holy place of work (Ceramic Research Lab). I cannot forget the extreme love and help that I got from my contemporary research fellows, **Dr. Aayush Gupta, Piyush Sharma, Dr. Mir Rameez, Pallavi Gupta** and many others.

I whole-heartedly with immense gratitude dedicate my thesis to my loving and caring family without whom I could not reach this point in my life. Parents can never be thanked in words. Prayers and sacraments of my father **Chhote Khan** and **Mother Jaytoon** have always enlightened my path of life. Love and support of my brothers **Dr. Ameer Khan, Subedar Sameeruddin,** and **Dr. Avidh Khan**, my sisters (-in-law) **Mrs. Sitara, Mrs. Reshma** and **Mrs. Sayma** have always motivated me to keep on moving.

Rather than thanking, I profoundly apologize to my brother son **Victor (Anas Sameer)** and my youngest brother daughter **Victory (Barkha)** for not being with them, when they needed me the most. I lost all their childhood memories in this endeavour towards accomplishing a Doctorate.

Besides this, **Alice (Ms Rinki)** and several near and dear friends & relatives have helped me in successfulcompletion of this work. It is impossible to name everyone in the limited words. I humbly apologizefor the same. I whole-heartedly thank every person who is not mentioned above, but contributed tomy thesis in one or the other way.

Above all! I thank the **Almighty Allah**, who always empowered me with His heavenly blessings, and made me feel His presence every time I felt low!!!

Savidh Khan

Savidh Khan

Date: 25/10/21

Place: Patiala

List of publications

Publications from thesis

1. **Savidh Khan** and K. Singh, Effect of MgO on structural, thermal and conducting properties of $V_{2-x}Mg_xO_{5-\delta}$ (x=0.05-0.30) systems, Ceram. Int. 45 (2019) 695. https://doi.org/10.1016/j.ceramint.2018.09.231 **(4.52)**
2. **Savidh Khan** and K. Singh, Structural, optical, thermal and conducting properties of $V_{2-x}Li_xO_{5-\delta}$ $(0.15 \leq x \leq 0.30)$ systems, Sci. Reps. 10 (2020) (1089) 1. https://doi.org/10.1038/s41598-020-57836-8 **(4.37)**
3. **Savidh Khan** and K. Singh, Influence of Al^{3+} doping for V^{5+} on the structural, optical, thermal and electrical properties of $V_{2-x}Al_xO_{5-\delta}$ (x=0-0.20) ceramics, Ceram. Int. 47 (2021) 10724. https://doi.org/10.1016/j.ceramint.2020.12.188 **(4.52)**
4. **Savidh** Khan and K. Singh, Effect of TiO_2 doping on structural and electrical properties of melt-quench $V_{2-x}Ti_xO_{5-\delta}$, $0.15 \leq x \leq 0.30$ systems, J. Mater. Sci: Mater Electron. 32 (2021) 12594. https://doi.org/10.1007/s10854-021-05896-5 **(2.47)**

Other SCI Publications

5. **Savidh Khan,** G. Kaur, K. Singh, Effect of ZrO_2 on dielectric, optical and structural properties of yttrium calcium borosilicate glasses, Ceram. Int. 43 (2017) 722. https://doi.org/10.1016/j.ceramint.2016.09.219 **(4.52)**
6. N. Kaur, G. Kaur, **Savidh Khan**, K. Singh, Conductivity, dielectric, and structural studies of (30-x)SrO-xBaO-10Al_2O_3-45SiO_2-5B_2O_3-10$Y_2O_3$$(5 \leq x \leq 25)$ glasses, Ionics 24 (2017) 2343. https://doi.org/10.1007/s11581-017-2360-y **(2.81)**
7. S. Jaidka, **Savidh Khan**, K. Singh, Na_2O doped CeO_2 and their structural, optical, conducting and dielectric properties", Physica B 550 (2018) 189. https://doi.org/10.1016/j.physb.2018.08.036 **(2.43)**
8. A. Kaur, **Savidh Khan**, D. Kumar, V. Bhatia, S.M. Rao, N. Kaur, K. Singh, A. Kumar, S.P. Singh, Effect of MnO on structural, optical and thermoluminescence properties of lithium borosilicate glasses, J. Lumin. 219 (2020) 116872. https://doi.org/10.1016/j.jlumin.2019.116872 **(3.59)**
9. S.S. Danewalia, S. Kaur, N. Bansal, **Savidh Khan**, K. Singh, Influence of TiO_2 and thermal processing on morphological, structural and magnetic properties of Fe_2O_3/MnO_2 modified glass-ceramics, J. Non-cryst Solids, 513 (2019) 64. https://doi.org/10.1016/j.jnoncrysol.2019.03.013 **(3.53)**
10. S.S. Danewalia, **Savidh Khan,** S. Dhillon**,** N. Bansal, G. Sharma. K. Singh. Effect of transition metals (MO-TiO_2, MnO_2, Fe_2O_3 and ZnO) on crystallization and electrical conductivity of SiO_2-CaO-Na_2O-P_2O_5-based glass-ceramics, Ionics, 26 (2020) 2959. https://doi.org/10.1007/s11581-019-03311-y **(2.81)**

Papers presented in Conferences

1. “Aluminium doped vanadate systems: structural and optical properties” at **International Symposium on Functional Materials-2018** held on 13-15 April 2018, at Shivalik View, Chandigarh.
2. “Physical, structural, optical and conducting properties of doped vanadate systems” at **International Conference on Materials for Energy Applications** held on 6-8 Dec 2018, at SS Jain Subodh PG College, Jaipur.
3. “Studies of aluminium doped vanadate systems for SOFCs applications” at **in international conference of international academy of physical sciences (IAPS) on innovations in physical sciences** held on August 09-11, 2019 at C.C.S. University, Meerut.

Index

Contents *Page No.*

List of Figures

List of Tables

List of Abbreviations

SOFC	Solid oxide fuel cell
IT-SOFC	Intermediate temperature solid oxide fuel cell
HOR	Hydrogen oxidation reaction
MEIC	Mixed ionic and electronic conductor
CTE	Coefficient of thermal expansion
YSZ	Yttria stabilized zirconia
OCV	Open cell voltage
XRD	X-ray diffraction
DTA	Differential thermal analyser
EDS	Energy dispersive x-ray spectroscopy
SEM	Scanning electron microscopy
UV	Ultra violet
FTIR	Fourier transform infrared
FWHM	Full width at half maxima
PLD	Pulsed laser deposition
TGA	Thermo gravimetric analysis
P	Density
V_m	Molar volume
N_i	Ionic concentration
R_i	Average inter-ionic distance
N_A	Avogadro’s number
r_p	Polaron radius
S	Siemen

GDC	Gadolinium doped ceria
ICDD	International centre for diffraction data
E_g	Optical band gap
E_U	Urbach energy
E_a	Activation energy
AC	Alternating current
DC	Direct current
σ_{ac}	AC conductivity
σ_{dc}	DC conductivity
k_B	Boltzmann's constant
DRS	Diffused reflectance spectra
SEM	Scanning electron microscopy
SPH	Small polarons hopping
NBOs	Non-bridging oxygens
BOs	Bridging oxygens
T_g	Glass transition temperature
T_c	Glass crystallization temperature
T_m	Melting temperature
F	Fragility
Tanδ	Tangent of loss
USM	Uniform strain model
XPS	X-ray photoelectron spectroscopy
Å	Angstrom
MTE	Mix transition effect

Abstract

The present thesis describes the synthesis of $V_{2-x}M_xO_{5-\delta}$ (M=Li_2O, MgO, Al_2O_3 and TiO_2 (x=0.05, 0.10, 0.15, 0.20, 0.25, 0.30) systems by melt-quench technique. The physical, structural, optical, thermal and conducting properties of the prepared samples are studied using various experimental techniques to determine their suitability as an electrolyte for IT-SOFC applications. Based on above properties, some selected samples are used for interaction study with interconnect materials, which is being used in solid oxide fuel cells. The research work carried out for Ph. D. thesis is divided into six chapters along with a list of cited references at the end of each chapter.

- **Chapter 1** describes the background and introduction of various fuel cells particularly SOFCs. The role of different components of solid oxide fuel cell has been discussed. Since the present work is related to develop electrolyte materials, therefore, the main focus has beengiven on the electrolyte materials of SOFCs. The suitability of materials as electrolyte is described in context to specific properties such as thermal stability at fuel cell operating temperature in oxidizing and reducing medium and electrical conductivity. The present studyreveals that the development of newer electrolyte materials with high conductivity at a lowertemperature and thermal stability is required.

- **Chapter 2** deals with the literature survey and gives an idea about the composition-based structure-properties of vanadium and others materials. The effect of various dopants on the different properties of V_2O_5 synthesized by various experimental techniques has been studied. From the literature survey it can be concluded that the ionic conductivity and thermal stability is great concerned at high operating temperature of solid oxide fuel cell (SOFC) in oxidizing and reducing medium. The high operating temperature of SOFC is responsible to degradation, coefficient of thermal expansion (CTE) mismatch, electrodes sintering and catalyst poisoning among the SOFC components. Based on the available literature survey, the

gaps in study and objectives of the present thesis are also given in the end of this chapter.

- **Chapter 3** gives the detail about source of raw materials, synthesis parameters and experimental method employed for samples preparation to achieve the proposed work objectives. The technical details of the used experimental characterizations are also given. It explains the techniques used for structural, optical, thermal and electrical characterization for as-synthesized samples. These techniques comprise X-rays diffraction (XRD) for phase formation, Fourier-transform infrared (FTIR) and Raman spectroscopy for structural vibrations analysis, UV-Visible spectroscopy for optical band gap analysis and scanning electron microscopy (SEM) for morphological study of the interface of diffusion couples. Differential thermal analysis (DTA) and thermo-gravimetric analysis (TGA) are used to analyze thermal stability of the as-synthesized samples. The two-probe impedance analyzer is used to study the electrical properties of the prepared samples.

- **Chapter 4** describes the results and discussion of the prepared samples. In this chapter, interpretations of the data obtained from various characterization techniques have been discussed. This chapter is further divided into five sections.

The first section represents the properties of $V_{2-x}Li_xO_{5-\delta}$ (x=0.15-0.30) systems. X-ray diffraction (XRD) patterns confirm the formation of three different crystalline phases (orthorhombic $Li_{0.04}V_2O_5$, monoclinic and monoclinic $Li_{0.30}V_2O_5$). FTIR and Raman spectra indicate that the doping of Li_2O into V_2O_5 leads to a transition from VO_5 into VO_4 structural unit. The optical band gap (E_g) decreases from 2.2 to 2.08 eV while Urbach energy (E_U) increases (0.31-0.41 eV) with the addition of Li_2O content in place of vanadium. Thermal stability is found to decrease with the Li_2O addition in place of V_2O_5. The DC conductivity is increased from 0.08 to 0.12 Scm^{-1} at 450 ^{o}C with Li_2O doping.

In second section, $V_{2-x}Mg_xO_{5-\delta}$ (x=0.0-0.30) systems has been explained. Density, inter-ionic distance, and fragility index are found to decrease with the addition of MgO content. The IR study suggests that the glass network is made up of VO_4 polyhedra by changing VO_5 structural units in the presence of MgO. Higher content of MgO improves the glass formation tendency and reduces the thermal stability of the samples. VM-0.30 glass shows the highest glass transition temperature (274 ºC) and Hruby's parameter (0.34) as compared to other samples due to its highest rigidity and glass formation ability. The conductivity of the samples decreases to~ 10^{-4} Sm^{-1} for x=0.30 at 300 °C, while activation energy increases to 0.38 eV with MgO content.

The third section describes the properties of $V_{2-x}Al_xO_{5-\delta}$ (x=0.0-0.30) systems. Density and molar volume are decreased with the doping of Al_2O_3 in place of V_2O_5. X-ray diffraction (XRD) pattern confirmed the formation of single phase (orthorhombic V_2O_5). The shifting of X-ray diffraction peak (010) to a higher angle revealed a compressive strain in the present samples due to the size difference of dopant (Al^{3+} ion) and host (V^{5+} ion). The estimated crystallite size was found in the range of 143.25-124.92 nm. Spectroscopic investigations revealed a transformation of the [VO_5] polyhedra into [VO_4] polyhedra on the doping of Al_2O_5 into V_2O_5. Thermal stability of the samples was found to decrease on the doping of Al_2O_3. The optical band gaps of the samples are found in the range of 2.31-2.35 eV. While DC conductivity lies in the range of 0.22-0.36 Sm^{-1} at 400 ºC.

The fourth section describes the properties of $V_{2-x}Ti_xO_{5-\delta}$ (x=0.0-0.30) systems. Density decreases whereas molar volume increases as the Al_2O_3 doping increases on the cost of V_2O_5. The X-ray diffraction peaks reveal a single-phase formation i.e. orthorhombic V_2O_5. Spectroscopic investigation clearly suggests structural changes on the doping of TiO_2 on the cost of V_2O_5 as [VO_5] groups are transformed into [VO_4] groups with formation of V-O-Ti chains. The optical band gap exhibits a decreasing trend as TiO_2 doping concentration increases and lies in the semiconductor range (2.28-2.20 eV). The DC conductivity of the samples increases with an increase in doping of TiO_2. The activation energy of the samples was found in the range of 0.275 to 0.231 eV. All the samples exhibit good DC conductivity (0.34 to 1.12 Scm^{-1}) at 400 ºC and good thermal stability (small weight change < 0.6%) in the temperature range of room temperature to 500 ºC.

This chapter also presents the interaction study between $V_{2-x}Mg_xO_{5-\delta}$ (x=0.20, 0.25) glass samples and AISI 430 steel as interconnect. The interaction between MgO doped V_2O_5 glass samples and SOFC interconnect material at 620 ºC for different time durations has been investigated using SEM experimental technique. $V_{2-x}Mg_xO_{5-\delta}$ (x=0.20, 0.25) glass samples exhibit good interface with AISI 430 steel at 620 ºC for 1, 10, and 100 h. In addition, the X-ray dot mapping also has been studied for better understanding of the morphology of the interfaces and diffusion of the elements from both sides. The formations of crystalline phases during heat treatment duration have also been studied.

Chapter 5 describes the overall conclusion drawn from the physical, structural, optical, thermal, and electrical properties along with interaction study of the prepared samples. To enrich this work, future scope of the present study has also been given at the end of this chapter.

Chapter 1 Introduction

1.1 Background

New energy sources are required to meet the demand of growing population due to the depletion of fossil fuels. Moreover, fossil fuel operated devices like automobiles emit different greenhouse gases such as NO_x, CO_2, CO, SO_2 etc. These greenhouse gases are cause to serious harm for environment [1-4]. Therefore, there is the need to develop low carbon, cleaner, economical and environment friendly renewable and sustainable energy sources to meet future demand of energy [1, 4-7]. Currently, solar cell and wind power have great interest as main stream renewable energy sources. But these renewable energy sources have some draw back such as requirement of huge areas of land and their climate dependency. Also, the poor efficiency of solar cells and high cost is the main hindrance of these energy sources. Therefore, different energy sources are being explored that can meet the demand without harming environment. Fuel cells and batteries could be new sustainable and renewable sources of energy. The fuel cells have shown great potential to become efficient and reliable energy source associated with their high efficiency, simple processing and environment friendly nature [8-10].

1.2 Fuel cells

Fuel cells are the energy conversion device that converts the chemical energy into electrical energy. Fuel cells are being used in a power source for an automobile, stationary power station and small portable electronic devices etc. The energy conversion efficiency of a fuel varies from 40 to 80% [11,12]. A single unit fuel cell comprises of anode, electrolyte and cathode as dipicted in Fig. 1.1. The fuel (typically H_2) is oxidized at anode with lose of electrons and oxygen is reduced at cathode with gain of electrons. The electrolyte is predominantly an ionic conductor which transports O_2 ions from cathode to anode and separates the anode from the cathode as well.

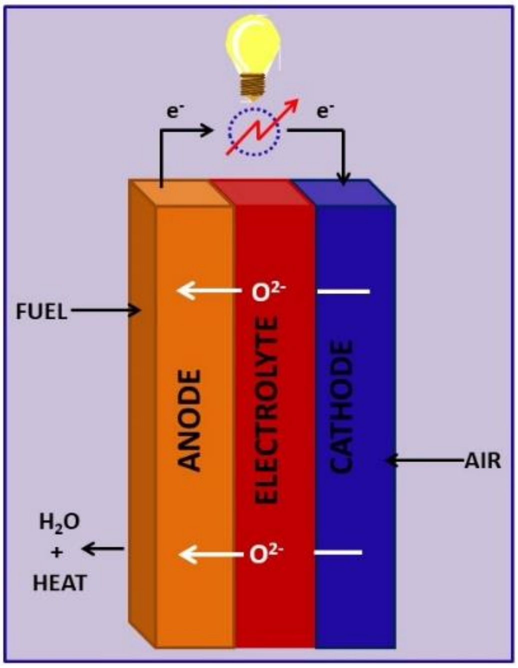

Fig. 1.1 Schematic diagram of a fuel cell.

1.2.1 Types of fuel cell

On the basis of the operating temperature and different electrolytes used, fuel cells are classified mainly into five categories. The salient features of fuel cells are summarized in Table 1.1 [13-18]. Out of these fuel cells, solid oxide fuel cells (SOFCs) are capable associated with their higher efficiency (80%), eco-friendly along with fuel flexibility (H_2, hydrocarbons etc.). Therefore, SOFC can be effective and viable power generated source in coming days. Moreover, SOFC has some additional advantages such as all components are made of solids, low-cost ceramics and alloys. Also, SOFC is not required any external catalyst due to its high working temperature (600-1000 ºC). There are many types of fuel cells such as alkaline fuel cell (AFC), phosphoric acid fuel cell (PAFC), polymer exchange membrane fuel cell (PEMFC) and molten carbonate fuel cell (MCFC). The electrolyte used, working temperature with their applications of these fuel cells are given in Table 1.1. Besides these, the advantages and disadvantages of these fuel cells are also given in Table 1.1. Therefore, the following section is emphasized on the details of SOFC with its components.

Table 1.1 Electrolyte used, working temperature, efficiency, disadvantages, advantages and applications of the different fuel cells [13-18].

Types of fuel cell	Electrolyte	Operating temperature (ºC)	Efficiency (%)	Disadvantage	Advantage	Probable application
Alkaline fuel cell (AFC)	Concentrated potassium hydroxide (L)	50-100	50-55	• Susceptible to CO_2 from air • Management related problems due to liquid form	• Cheapest to produce • Fast kinetics for the O_2 reduction	Military and space
Phosphoric acid fuel cell (PAFC)	Phosphoric acid (L)	150-200	40	• Highly corrosive nature of electrolyte (phosphoric acid) • Long start up time	• Allow use of impure fuels due to higher operation temperature	Distributed generation
Polymer exchange membrane fuel cell (PEMFC)	Sulfonated fluoro polymer membrane (S)	50-100	55	• Costly catalysts are required • Susceptible to fuel impurities owing to low working temperature	• Low working temperature allows fast start up time	Transportation Backup and portable power
Molten carbonate fuel cell (MCFC)	Alkali metal carbonates (L)	600-650	45-50	• High working temperature degrades the components • Corrosion issues • CO_2 feeding is required for cathode	• Allow use of impure H_2 fuels due to higher operation temperature • No poisoning issues by CO and CO_2 • Can use variety of catalysts	Electric utility and distributed generation
Solid oxide fuel cell (SOFC)	Ceramic (S)	600-1000	80	• High working temperature • Long start up time • Thermal expansion incompatibilities issues • Cell sealing issue	• Higher efficiency • Fuel flexibility • Corrosion free due to all solid-state systems	Electric utility and large distributed generation

1.2.2 Solid oxide fuel cell

The present research work is emphasis on the advancement of new materials for IT-SOFCs. SOFCs have been gained much attention as compared to other fuel cell owing to their high efficiency and eco-friendly with fuel flexibility [19]. SOFCs are used an ionically conducting ceramic material as an electrolyte. The use of solid electrolytes eliminates the problems of liquid-based electrolytes such as leakage, handling and high corrosion [20]. The high operating temperature (600-1000 ºC) of SOFCs shows two-fold effect such as allows the rapid reaction kinetics without using any expansive catalyst (platinum) along with cheaper electrodes [21]. SOFCs are solid state device with no moving parts and can generate high quality waste heat which can be used further for increasing efficiency up to 80% [22, 23]. However, the high working temperature of SOFs is responsible to increase the corrosion and fast degradation of components, which leads to decrease the efficiency and life of the cells. Therefore, SOFCs are potentially cheaper and easy to manufacture as compared to other fuel cells. Additionally, the high operating temperature of SOFC invites some problems related to materials compatibility such as degradation, thermal expansion mismatching among components, CO poisonous effect, electrode sintering, requirement of thermally and mechanically stable materials at high temperatures etc. So, SOFCs are prohibitively expensive for most of the applications due to its higher operating temperatures [22,23]. Therefore, the prime goal of the present research is to develop electrolyte materials for IT-SOFC.

1.2.3 Working of a SOFC

The schematic diagram of working operation of the SOFCs is shown in Fig. 1.3. A SOFC comprises of three main parts namely porous cathode (air or reduction electrode), porous anode (fuel or oxidation electrode) and dense electrolyte [24, 25]. The H_2 enters into the anode and undergoes a reaction with O^{2-} ions. Meanwhile, the O_2 comes into the cathode and undergoes a catalytic dissociation which leads to the creation of O_2 ions. The O_2 ions migrate with the help of electrolyte and meet with H_2 ions at triple phase boundary (anode), thereby generating the electrons. Both the ions are consumed at the same time, and combined to generate water vapour as a by-product [26]. The formation of water vapour inspires the consumption reaction on electrodes. The generating electrons are transferred from anode to cathode with the help of an external electrical circuit.

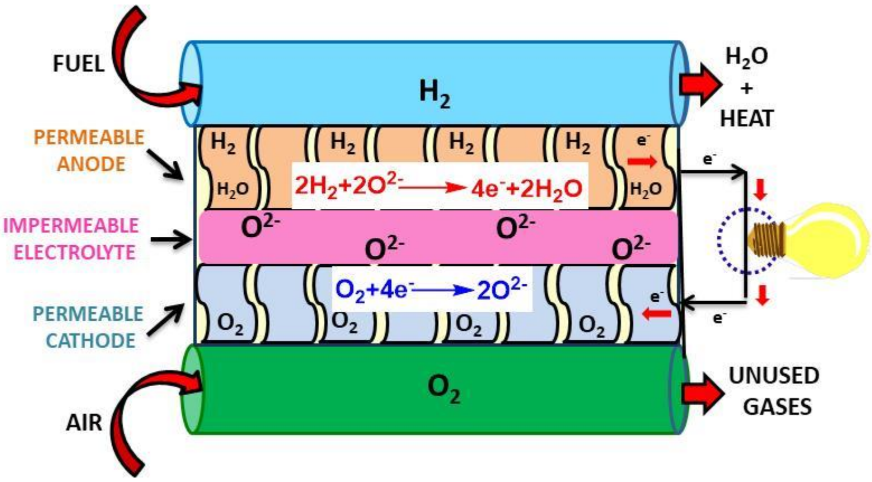

Fig. 1.2 Schematic diagram of working principle of SOFC.

The migration of the O_2 ions from cathode to anode maintains the overall charge balance that produces useful electricity by fuel burning. For simplicity, the electrodes reactions of SOFC for pure H_2 as a fuel are given below.

$$\text{Anode: } 2H_2 + 2O^{2-} \rightarrow 2H_2O + 4e^- \quad (1.1)$$

$$\text{Cathode: } O_2 + 4e^- \rightarrow 2O^{2-} \quad (1.2)$$

$$\text{Overall reaction: } 2H_2 + O_2 \rightarrow 2H_2O + External\ electrical\ energy \quad (1.3)$$

1.3 Required properties for different components of SOFC

There are three major components of SOFCs namely cathode, electrolyte and anode. Additionally, interconnect material is also required to connect the cells in series for increasing the output voltage. Depending on the design of SOFCs, the planar design SOFC is also required sealing materials (glass sealants) to prevent the leakage of the fuel and mechanically support the other components. Therefore, required basic properties and state of the art of these materials are discussed below.

1.3.1 Anode materials

The anode materials must be chemically stable in a reducing oxygen atmosphere and catalytically active for the hydrogen oxidation reaction (HOR). It also requires high electronic and some ionic conductivity with compatible thermal and chemical stability with the other components of SOFCs. The most commonly used anode is some type of ceramic-metal mixture known as cermet. The anode cermet is a mixture of metal (nickel) and electrolyte ceramic material (most common, yttria stabilized zirconia). Nickel metal is usually used due to its high catalytic activity to the HOR and low cost [27]. The combination of Ni and ceramic diminishes the creation of Ni clusters within anode materials, which leads to the decreasing number of reaction sites along with increasing TPB. Additionally, the use of cermet with electrolyte suggests similar coefficient of thermal expansion (CTE) which reduces the possible thermal cracking problems within components. The drawback of the use of nickel cermet is that a non-conducting layer is formed between electrolyte and anode due to the occurrence of a cross reaction with La based electrolytes [28]. Furthermore, the existence of sulphur in natural gas produces stability problem due to the formation of NiS and subsequently poisoning of the anode. Therefore, some newer substitutes (CeO_2, perovskite structured materials) for anodes are under investigation [29, 30]. The perovskites materials ($La_{0.75}Sr_{0.25}Cr_{0.5}Mn_{0.5}O_{3-\delta}$, LSCM) have also been considered as anode material. It shows good electrochemical activity to the HOR similar to the Ni/YSZ cermet. But it shows a lower electronic conductivity and instability with sulphur. The doped strontium titanate ($SrTiO_3$) is another suitable perovskite structured material which exhibits high electronic conductivity in a reducing environment (H_2) along with high chemical stability with sulphur impurities [29, 31]. But titanates show poor ionic conductivity and electrochemical activity towards the HOR required by fuel cells [31, 32]. Lastly, Cu-doped CeO_2 exhibits good electronic and ionic conductivity along with extra sulphur tolerant as compared to Ni/YSZ cermet. The Cu-doped CeO_2 does not show any poising up to 450 ppm (part per millions) H_2S whereas nickel cermet sows poisoning below 15ppm H_2S in the fuel. But, the problem with Cu doped CeO_2 is that the conductivity tends to be lower as compared to ideally required one.

1.3.2 Cathode materials

The cathode materials must be chemically stable in an oxidising medium and catalytically active for the hydrogen oxidation reaction (HOR). It also requires mix (electronic and ionic) conductivity with thermal stability and chemical compatibility with the electrolyte and interconnector material. Platinum was the first material used as a cathode in SOFCs and still has a great interest scientifically. However, the high cost of Pt limits its use as a commercially cathode. Also, Pt cathodes can be poisoned at low temperature with CO fuel in SOFC. It can be reduced the efficiency by blocking the active sites. Pt and Ru containing alloys were studied to solve these issues but these increases cost further. The perovskite structure materials show good potential as a cathode for SOFCs owing to change their structure upon heating, which leads to an increase in the electronic conductivity [33, 34]. $La_{1-x}Sr_xCoO_{3-\delta}$ (LSC) is considered as a perovskite cathode material due to its better catalytic performance as compared to other perovskites. It is an O_2 deficient perovskite with the O_2 vacancies allowing for high oxide ion conduction [35]. But it exhibits CTE mismatch problem when used with commercially available electrolytes (YSZ or CGO), which leads to the cell degradation under fuel cell operation. Another perovskite, $La_{1-x}Sr_xMnO_3$ (LSM) was proposed as a cathode for SOFCs that exhibits high electronic conductivity, high catalytic activity. However, low ionic conductivity at intermediate temperatures and poor chemical compatibility with YSZ at higher temperature of LSM discourage to use as a cathode for SOFCs. The overall performance of the SOFCs is affected by the formation of nonconductive layer of $La_2Zr_2O_7$ at the YSZ/LSM interface at elevated temperatures [36]. $La_{1-x}Sr_xCo_yFe_{1-y}O_3$ (LSCF) is another perovskite material which is under investigation for IT-SOFC that exhibits high electro catalytically activity good chemical stability and CTE matching with commercial electrolytes. But, the formation of $SrCrO_4$ phase could be responsible to decrease the overall performance of the fuel cell [37]. Recently, $Ln_2NiO_{4+\delta}$ materials are investigated as a potential SOFCs cathode due to their suitable electrical and catalytically properties. These materials have K_2NiF_4 type structure in which $LaNiO_3$ layers (perovskite type) are separated by LaO^+ (rock salt type) layers [38]. The perovskite layers are accommodated by the oxygen vacancies whereas the rock salt layers are accommodated by the oxygen interstitials. $Ln_2NiO_{4+\delta}$ (Ln=La and Nd) systems have also been studied widely for SOFCs cathodes associated with their good conductivity along with appreciable activation energy [39]. The coefficient of thermal expansion of $La_2NiO_{4+\delta}$ and $Nd_2NiO_{4+\delta}$ materials is comparable to YSZ and CGO [40-43]. $Nd_2NiO_{4+\delta}$ material responds with YSZ at 1100°C with forming $Nd_2Zr_2O_7$ phase whereas $La_2NiO_{4+\delta}$ reacts with YSZ and CGO at 900°C with forming $La_3Ni_2O_7$ and $La_2Zr_2O_7$, respectively on heating for 2 h [44]. Consequence, the detrimental effect on the stability of the materials associated with the high working temperature of SOFCs has been occurred [45].

1.3.3 Electrolyte materials

The electrolyte material must be thermodynamically and chemically stable in reducing and oxidising medium at cell operating temperatures (600-1000 ºC). It also requires high ionic conductivity (~0.1Scm^{-1}), negligible electronic conductivity, high density and good mechanical properties [46,47]. In electrolyte materials, ionic conductivity is associated with the hoping mechanism between vacant sites and can be enhanced by increasing the fraction of oxygen vacancies/defects [47, 48, 49]. There are a number of electrolyte materials which have been developed for SOFCs application. Based on the structure and type of base materials, the solid-state electrolytes can be divided into following categories.

1.3.3.1 Fluorite structure-based oxides

The zirconia (ZrO_2) based electrolyte which has a fluorite structure is being used most commonly for SOFCs application. ZrO_2 shows poor conductivity below 2300 ºC. But it shows increasing trend of conductivity after 2300 ºC associated with a phase change from monoclinic to cubic structure [50]. To stabilize this cubic structure lower than 2300 ºC temperatures than, the several lower valence dopants (Y^{3+}, Yb^{3+}, Gd^{3+}, Ca^{2+}, Mg^{2+}) on the Zr^{4+} site have been studied. At the same time this process generates O_2 vacancies, which leads to an increase in ionic conductivity [51]. Yttria stabilized zirconia (YSZ) is mostly used as electrolyte in a wide range of temperatures owing to its good mechanical and electrical properties and low cost [52].

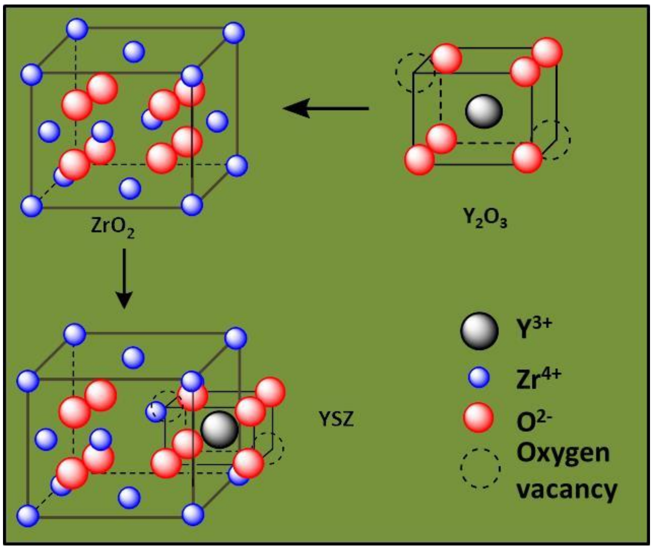

Fig. 1.3 Crystal structure of yttria stabilized zirconia.

YSZ with cubic structure shows very good conductivity and stability in O_2 partial pressure for high temperature SOFC. The crystal structure and hopping mechanism for conduction of 8YSZ is shown in Fig. 1.4 and Fig.1.5, respectively. But it requires operating temperatures from 800 to 1000°C to deliver a acceptable ionic conductivity. The high working temperature is a big challenge in terms of stability and sealing of the SOFC [53,54]. Further scandium stabilized zirconia can be considered as an alternative due to its higher ionic conductivity and low cost as compared to YSZ over an intermediate temperature range. Another fluorite structure electrolyte is doped CeO_2, which shows better ionic conductivity than YSZ at lower temperature ranges (500-700 ºC).

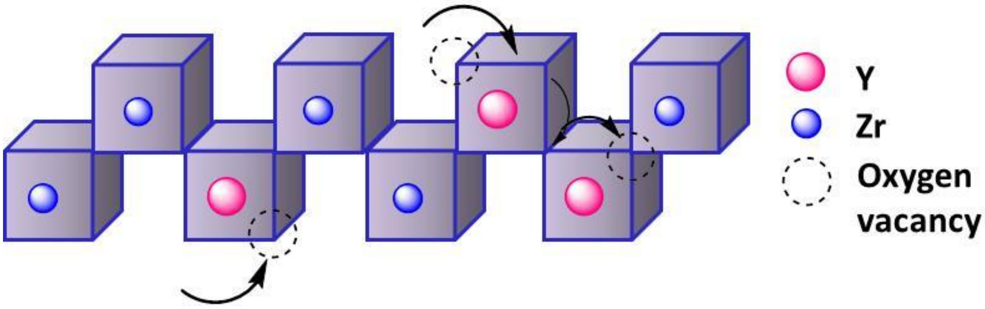

Fig. 1.4 Schematic diagram of vacancy transport process in yttria stabilized zirconia.

The ionic conductivity of CeO_2 increases with doping of Sm^{3+}, Gd^{3+} and Y^{3+} due to formation of O_2 vacancies as given in Fig. 1.5. Sm^{3+}, Gd^{3+} and Y^3 doped CeO_2 show good ionic conductivity and compatibility when used with electrode [53,55,56]. However, ceria shows reduction (from Ce^{4+} to Ce^{3+}) in low O_2 partial pressure at higher temperature (>600 °C), leading to reduce the overall cell voltage. This reduction in cell voltage due to dominating electrical contribution at higher temperature causes partial cell short circuiting [57,58,59].

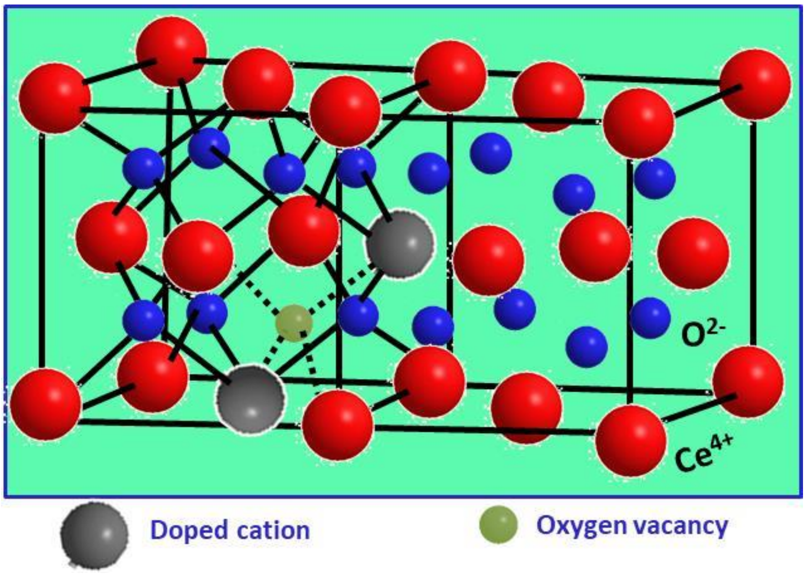

Fig. 1.5 Crystal structure of doped ceria.

1.3.3.2 Apatite electrolytes

Apatite electrolytes having general formula $M_{10-x}X_6O_{26\pm\delta}$, (where, M = alkaline or rare earth metal and X = Si, Ge, P) have been studied widely. It has higher ionic conductivity with low activation energy for ionic conduction at moderate temperatures and low partial pressure. Above mentioned properties of apatite are comparable to the conventional YSZ electrolyte [60,61,62,63]. The Si and Ge based apatite electrolytes show good ionic conductivity. Also, they show flexibility for doping on either the M or X site to produce higher oxygen vacancies [64,65,63]. The silicate and germinate apatite electrolytes have capability to accommodate excess O^{2-}. On the other hand, apatite phosphate electrolytes account for their poor conductivity due to inability to accommodate these excess oxide ions. The silicate apatites have shown great potential than germinate apatites associated with their good ionic conductivity, low activation energy and low cost of the raw materials. The stoichiometric systems such as $La_8Ca_2Si_6O_{26}$, $La_8Sr_2Si_6O_{26}$ and $La_8Ba_2Si_6O_{26}$ exhibit extremely poor conductivity (5.6×10^{-4} Scm^{-1}) at 800 ºC [66,67]. However, the conductivity can be improved by introduce the oxygen vacancies or cation vacancies by selecting lower valence/higher valence dopants. The doping of $Al^{3+}/Mg^{2+}/Ga^{3+}$ on Si^{4+} site with charge balancing by adjusting the lanthanum content has been delivered good conductivity due to excess oxygen vacancies. The $La_{9.8}Si_{5.7}Mg_{0.3}O_{26.4}$ system exhibits good conductivity (0.07 Scm^{-1}) at 800 ºC [68]. The CTE of these apatite materials also matches with the other components of the SOFCs. The demerit of these apatites is that they require high processing temperature (>1600 ºC) to produce large grain size and dense membrane, which is needed for a SOFCs electrolyte [69]. In addition, silicon containing materials have chemical compatibility issues with conventional perovskite materials are being used as other components of SOFCs. Additionally, the larger unit cells of these materials could lead to lower power density. For instance, the fuel cell with $La_{0.8}Sr_{0.2}CoO_3$ cathode,

$La_{9.8}Si_{5.7}Mg_{0.3}O_{26.4}$ electrolyte, and Ni-Sm doped ceria anode is produced a low power density (120 mW cm^{-2} at 800°C) than currently available YSZ based systems [68].

1.3.3.3 Bismuth based electrolytes

Bi_2O_3 is another best ionic conductor having fluorite structure. It shows high ionic conductivity due to high fraction of vacancies and good catalytic activity in air between 300-350 ºC temperature. Bi_2O_3 consist of two stable polymorphs monoclinic (α) and cubic (δ), in which δ-Bi_2O_3 shows the highest conductivity (1.0 Scm^{-1}) at 800 ºC. The δ-Bi_2O_3 phase is stable in the range of 730-804 ºC, which shows around 2 orders higher ionic conductivity as compared to YSZ electrolyte [70]. The δ-Bi_2O_3 phase might be stabilized at room temperature by partially substituting of bismuth with Y^{3+}, La^{3+}, Er^{3+} or Dy^{3+} cations [71]. However, it exhibits 3 orders drop in conductivity upon cooling below 600 ºC associated with the ordering of O_2 vacancies [72]. On the other hand, to stabilize δ-Bi_2O_3 phase at room temperature, the size difference between Bi^{3+} and dopants is also important factor. It is observed that the partial substitution of Bi-sites with 25-43 mol% of Y_2O_3 stabilizes the conducting δ-Bi_2O_3 phase between 500-700 ºC temperature [73,74]. The composite of $(Bi_2O_3)_{0.75}$ $(Y_2O_3)_{0.20}$ $(Nb_2O_5)_{0.05}$ composition shows good conductivity than YSZ. The Y and Er-doped bismuth namely, $Bi_{1-x}Y_xO_{1.5}$(x=0.23-0.25) and $Bi_{1-x}Er_xO_{1.5}$(x=0.20), shows good ionic conductivity of 0.023 Scm^{-1} and 0.37 Scm^{-1} at 500 ºC and 700 ºC, respectively [75,76].

The main drawback of stabilized-Bi_2O_3 based systems is their tendency to reduce bismuth metal in a reducing atmosphere [77,78,79]. Some other drawbacks such as volatilization at moderate temperature, corrosion, poor thermal and electrical stability of Bi_2O_3 limit their practical applicability.

The Rhenium (Re) stabilized δ-Bi_2O_3 phase ($Bi_{12.5}La_{1.5}ReO_{24.5}$) has higher conductivity (0.001 Scm^{-1}) at 300 ºC than stabilized by Dy/W co-doping. These are known to have the highest conductivity in bismuth-based systems [80].

1.3.3.4 $La_2Mo_2O_9$ (LAMOX) electrolyte

$La_2Mo_2O_9$ is a fast O_2 ionic conductor than YSZ. $La_2Mo_2O_9$ does not show a irreversible phase change from nonconducting monoclinic phase (α) to a high conducting cubic phase (β) at about 580 ºC. It shows good conductivity 0.01 Scm^{-1} at 800 ºC. However, the phase change is the first restriction for this material because it can experience a mechanical breakdown owing to frequent phase change with thermal cycle [81,82]. Therefore, a wide range of substitutions such as Gd and Y for La have been studied to stabilize the high conducting β phase at lower temperature. Bismuth and molybdate-doped $La_2Mo_2O_9$ are found to be stable at room temperature. The tungsten-doped LAMOX exhibits decent conductivity and stability at 600 ºC. Pr can also be used as $La_2Mo_2O_9$ to avoid the phase change tendency. However, no suppression in phase change has been observed with Pr doping [82]. Moreover, LAMOX shows high CTE of 13.6 and 16.8 $\times 10^{-6}$ /K at high and low temperature phase, respectively, which is not well-suited with the other components of SOFCs [83]. Additionally, Mo_2 is susceptible to reduction at low O_2 pressure. LAMOX has high ionic transference number (0.98) in moderate reducing environment. However, at O_2 partial pressure (10^{-8} Pa at 800 ºC), it shows phase transition [84].

1.3.3.5 Perovskite structure-based electrolytes

Perovskites (ABO_3) structure have been gained great attention due to their used as electrolytes in SOFCs application. Perovskite comprises of a larger corner cation A, which is coordinated with 12 anions around it and a smaller cations B are on the corners of the cell with octahedral co-ordination to the anions (BO_6) as shown in Fig. 1.7. The oxygen stoichiometric of these perovskites can be changed by the doping either on site A or site B. Generally, perovskite electrolytes are made by doping of the A and B sites with aliovalent cations, leading to the higher ionic conductivity associated with the formation of O_2 vacancies. The addition of Sr^{2+}, Mg^{2+}, Ba^{2+}, Ca^{2+} cations at La^{3+} sites to $LaBO_3$ oxides enhance the ionic conductivity and catalytic activity associated with creation of O_2 vacancies for compensating defects [35]. The highest conductivity is found with Sr^{2+} doping due to the creation of low pair cluster except for $LaCoO_3$ [35]. The produced O_2 vacancies get stuck between host cations and dopant owing to elastic and electrostatic interactions between host and dopant, which decreases the concentration of O_2 vacancies in the system. The presence of ordered O_2 vacancies in microdomains has also been observed. The Sr^{2+} and Mg^{2+} doped $LaGaO_3$ facilitates the oxide ion conduction at high level associated with the creation of more O_2 vacancies, resulting in a good ionic conductivity. In case of LSGM ($La_{1-x}Sr_xGa_{1-x}Mg_yO_{3-\delta}$) series, maximum ionic transport has been found for x=0.10-0.20 and y=0.15-0.20 [35, 85]. The LSGM thin film shows good conductivity (0.1 Scm^{-1}) at 800 ºC. The power density for single cell performance is 0.4 Wcm^{-1} at 700 ºC. Further, it is reported that the ionic conductivity enhances along with slightly enhance in electronic conductivity with replacing of Ga^{3+} by CO^{3+}. There are several drawbacks with gallium such as volatilization, reaction with perovskite cathode and formation of secondary phase which is stable stable during processing restricts adaptation of $LaGaO_3$ based ceramics as potential electrolytes. The $LnBO_3$ (B=Al, In, Sc and Y) based perovskites show better properties than $LaGaO_{3-\delta}$ and $CeO_{2-\delta}$.

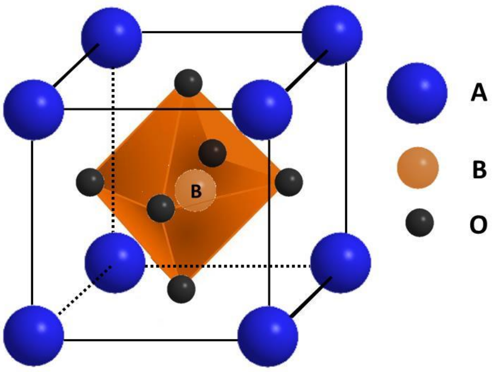

Fig. 1.6 Perovskite (ABO_3) crystal structure.

These materials also offer good thermal (CTE=10.4-10.6×10^{-6} /K) mechanical and compatibility. However, these materials show high p-type electronic conductivity and low ionic conductivity in oxidizing environment. The main drawbacks of these materials are their high grain boundary resistivity and poor sinter ability [35]. Perovskite aluminate ($La_{0.9}Sr_{0.1}AlO_{3-\delta}$)

has maximum conductivity as compared to the Sr^{2+} doped $LaGO_3$ systems. Though, Mg^{2+} doping on B site is enhanced creation of oxygen vacancies, but it has a negative impact on ionic conductivity (decreases) due to ordering of oxygen vacancies. In this category, $LnBO_3$ (B=In, Sc/Y) based materials like $La_{0.09}Sr_{0.1}InO_{3-\delta}$, $La_{0.09}Sr_{0.1}AlO_{3-\delta}$ and $La_{0.09}Sr_{0.1}ScO_{3-\delta}$ show electrical conductivity in both N_2 and air environment [35]. All the system shows around 0.5 orders of lower conductivity in N_2 than air, which is associated with the large p-type conductivity over the high O_2 partial pressure. $La_{0.09}Sr_{0.1}InO_{3-\delta}$ shows the highest ionic conductivity at 800 ºC in N_2 environment whereas $La_{0.09}Sr_{0.1}ScO_{3-\delta}$ shows the highest conductivity below 800 ºC. Sr-doped $LaScO_3$ is not pure ionic conductor [35, 86]. Literature validates that the scandate systems show the lowest ionic conductivity than $La_{0.09}Sr_{0.1}Al_{0.9}Mg_{0.1}O_{3-\delta}$, $La_{0.09}Sr_{0.1}Sc_{0.9}Mg_{0.1}O_{3-\delta}$ and $La_{0.09}Sr_{0.1}In_{0.9}Mg_{0.1}O_{3-\delta}$. Similarly, $LaYO_3$ based electrolytes exhibit considerable protonic and p-type conduction as well. The $La_{1-x}Sr_xYO_{3-\delta}$ solid solutions have been investigated and found that the proton conduction is dominated over the ionic conduction below 550 ºC. Some perovskite oxides such as cerates and zerconates show proton conduction in hydrogen environment at high temperatures. Gd^{3+}/Y^{3+}-doped $BaCeO_3$ and $SrCeO_3$ systems show high protonic conductivity. However, cremates like $BaCeO_3$ and $SrCeO_3$ show poor mechanical and chemical stability due to the formation of non-conducting barium carbonate ($BaCO_3$) phase below 800 ºC [35]. On the other hand, zerconates such as $BaZrO_3$ have higher chemical and mechanical stability. However, it exhibits lower protonic conductivity owing to the high grain boundary resistance. $BaCeO_3$ exhibits an enhancement in the conductivity with the doping of Y on site B while decreases with doping of Sr on site A and Y on site B. The rare earth doped materials like $BaCe_{0.8}Gd_{0.2}O_{3-\delta}$ (BCG) and $BaCe_{0.7}Sn_{0.1}Gd_{0.2}O_{3-\delta}$ (BCSG) show good conductivity (0.01 Scm^{-1}) at 700 ºC. While $BaCe_{0.9-x}Zr_{0.x}Y_{0.1}O_{3-\delta}$ (x=0.2-0.8) sintered (at 1700 ºC) systems show decreasing trend of conductivity with increasing content of CeO_2.

1.3.4 Interconnects

A single SOFC unit produces open cell voltage (OCV) of ~1 volt only. An SOFC array (stack) is thus used to create a high voltage for real life applications. Interconnects are used for stacking of the various SOFCs. The interconnect materials are provided an electrical contact between anode of one individual cell to the cathode of the adjacent cell. Therefore, interconnect must be stable in both reducing and oxidizing medium along with good electronic conductor. Furthermore, the CTE must be matched with the other SOFC components to avoid the stress generation at the cell working temperature. In addition, low cost and ease of fabrication are also important for the cost-effective production of fuel cells. Generally, SOFC interconnect materials can be either ceramic or metals/alloys. Ceramic materials are generally employed between 800-1000°C as interconnects. While metallic interconnects are used below 750 °C. Generally, strontium/calcium doped-$LaCrO_3$ is used as ceramic interconnect with YSZ electrolyte. But the high cost and decreasing conductivity with decreasing temperature limit their usages as interconnect for SOFCs applications. So, the metallic interconnects (Cr-based alloys and ferritic steels) are also developed. They exhibit high electrical and thermal conductivity and ability to accommodate thermal stresses as compared to ceramic interconnects. They are attractive but the fabrication cost is relatively high as compared to ceramic interconnects. Presently, the ferritic stainless steels are the most striking metallic interconnect for SOFC application [19]. Though, they have some drawbacks such as poor electrical contacts between metallic interconnect and ceramic electrodes, matching of CTE and cathode poisoning.

1.3.5 Sealants

The seal is required for planar SOFC to avoid the mixing of fuel and air for preventing the direct combustion of fuel and leakage of the fuel. Sealant must be chemically and thermally stable in both oxidising and reducing medium at cell working temperature. The CTE of the sealants should be matched with the other components of SOFC. There are two types of seals such as compressive and rigid for SOFCs application. A major advantage of compressive seals is that the seals are not required exactly match of CTE. Generally, the metal gaskets (silver, mica-based materials) are used as compressive seals. But they required load continuous during cell operation. On the other hand, rigid seals do not require continuous load but CTE must be matched with the other SOFC components. Glasses and glass-ceramics are employed as rigid seals for SOFCs application. The CTE mismatching and stress related problems at cell operation are occurred in most of the rigid glass seals. Metallic brazes are also considered as rigid seals with accommodating of stress than glass-ceramics. But cost of metallic brazes is a challenge for commercialize the SOFCs.

As discussed in electrolytes section of this chapter, a lot of research work going on various structured materials with variety of different dopants. YSZ is good electrolyte material for high temperature (800-1000 ˚C) SOFC. Perovskite structured and cerium doped materials are being investigated for electrolyte application in SOFC. Recent time, vanadium-based materials have also been investigated as electrolyte for SOFC applications. The literature survey of these systems is given in the next chapter.

References

1. D. Cheney, P. O'Neill, G. Norton, A. Veneman, D. Evans, N. Mineta, S. Abraham, S. Allbaugh, National energy policy, 2001, 1, 7-25.
2. E. Kendrick, M.S. Islam, P.R. Slater, J. Mater. Chem. 17 (2007) 3104.
3. A. Onishi, J. Policy Model. 29 (2007) 797.
4. A. Yamasaki, J. Chem. Eng. Jpn. 36 (2003) 361.
5. K.T. Lee, H.S. Yoon, E.D. Wachsman, J. Mater. Res. 27 (2012) 2063.
6. M.A. Schilling, M. Esmundo, Energ. Policy 37 (2009) 1767.
7. S.F. Tie, C.W. Tan, Renew. Sust. Energ. Rev. 20 (2013) 82.
8. S.C. Singhal, Solid State Ionics 135 (2000) 305.
9. S.M. Haile, Acta Mater. 51 (2003) 5981.
10. B.C.H. Steele, Nature 400 (1999) 619.
11. N.Q. Minh, T. Takahashi, Science and Technology of Ceramic Fuel Cells (1995) Elsevier Science Amsterdam.
12. N.Q. Minh, J. Ceram. Soc. 76 (1993) 563.
13. C.S. Song, Catal. Today 77 (2002) 17.
14. L. Carrette, K.A. Friedrich, U. Stimming, Chemphyschem 1 (2000) 162.
15. G.F. McLean, T. Niet, S. Prince-Richard, N. Djilali, Int. J. Hydrogen Energ. 27 (2002) 507.
16. A. Kulkarni, S. Giddey, J. Solid State Electrochem. 16 (2012) 3123.
17. S. F. Au, S. J. McPhail, N. Woudstra, K. Hemmes, J. Power Sources 122 (2003) 37.
18. S. Authayanun, K. Im-Orb, A. Arpornwichanop, Chinese J. Catal. 36 (2015) 473.
19. S.C. Singhal, K. Kendall, High temperature solid oxide fuel cells: fundamentals (2000) Elsevier New York.
20. Nagamoto, Encyclopedia of Material Science, 1st ed, (2001) 3359.
21. D.J. L. Brett, A. Atkinson, N.P. Brandon, S. J. Skinner, Chem. Soc. Rev. 37 (2008) 1568.
22. A. Weber, E.I. Tiffee, J. Power Sources 127(2004) 273.
23. H. Tu, U. Stimming, J. Power Sources 127 (2004) 284.
24. J. Larminie and A. Dicks, Wiley Fuel Cells Systems Explained, 2nd ed (2003) 406.
25. K. Kordesch, G. Simader, Fuel cells: and their applications, 1st ed (2006) 23.
26. M. Liu, M.E. Lynch, K. Blinn, F. Alamgir, Y. Choi, Mater. Today 14 (2011) 534.

27. M. Mukhopadhyay, J. Mukhopadhyay, R.N. Basu, Trans. Indian Ceram. Soc. 72 (2013) 145.
28. D. Marrero-Lopez, M. C. Martin-Sedeno, J. Pena-Martinez, J. C. Ruiz-Morales, P. Nunez, M.A.G. Aranda, J.R. Ramos-Barrado, J. Power Sources 195 (2010) 2496.
29. O.A. Marina, N.L. Canfield, J.W. Stevenson, Solid State Ionics 149 (2002) 21.
30. X. Li, H. Zhao, N. Xu, X. Zhou, C. Zhany, N. Chen, Int. J. Hydrogen Energ. 34 (2009) 6407.
31. M.C. Verbraeken, T. Ramos, K. Agersted, Q. Ma, C.D. Savaniu, B.R. Sudireddy, J.T.S. Irvine, P. Holtappels, F. Tietz, RSC Adv. 5 (2015) 1168.
32. X.W. Zhou, N. Yan, K.T. Chuang, J.L. Luo, RSC Adv. 4 (2014) 118.
33. M. Gazda, P. Jasinski, B. Kusz, B. Bochentyn, K. Gdula-Kasica, T. Lendze, W. LewandowskaIwaniak, A. Mielewczyk-Gryn, S. Molin, Environmental Degradation of Engineering & Materials Engineering and Technologies 183 (2012) 65.
34. C.D.L. Calle, A. Aguadero, J.A. Alonso, M.T. Fernandez-Diaz, Solid State Sci. 10 (2008) 1924.
35. N. Mahato, A. Banerjee, A. Gupta, S. Omar, K. Balani, Prog. Mater. Sci. 72 (2015) 141.
36. A. Mitterdorfer, L.J. Gauckler, Solid State Ionics 111 (1998) 185.
37. S.P. Jiang, X.B. Chen, Int. J. Hydrogen Energ. 39 (2014) 505.
38. H. Zhao, Q. Li, L.P. Sun, Sci. China Chem. 54 (2011) 898.
39. F. Chauveau, J. Mougin, F. Mauvy, J.M. Bassat, J.C. Grenier, T. Electrochem. Soc. 25 (2009) 2557.
40. E. Boehm, J.M. Bassat, P. Dordor, F. Mauvy, J.C. Grenier, P. Stevens, Solid State Ionics 176 (2005) 2717.
41. A.J. Jacobson, Chem. Mater. 22 (2010) 660.
42. H. Ullmann, N. Trofimenko, F. Tietz, D. Stover, A. Ahmad-Khanlou, Solid State Ionics 138 (2010) 79.
43. V.V. Kharton, A.V. Kovalevsky, M. Avdeev, E.V. Tsipis, M.V. Patrakeev, A.A. Yaremchenko, E.N. Naumovich, J.R. Frade, Chem. Mater. 19 (2007) 2027.
44. F. Mauvy, C. Lalanne, J.M. Bassat, J.C. Grenier, H. Zhao, L.H. Huo, P. Stevens, J. Electrochem. Soc. 153 (2006) A1547.
45. A.M. Hernandez, L. Mogni, Caneiro, Int. J. Hydrogen Energ. 35 (2010) 6031.
46. E. Kendrick, M.S. Islam, P.R. Slater, J. Mater. Chem. 17 (2007) 3104.
47. A. Orera, P.R. Slater, Chem. Mater. 22 (2010) 675.

48. E. Kendrick, A. Orera, P.R. Slater, J. Mater. Chem. 19 (2009) 7955.
49. E. Kendrick, J. Kendrick, A. Orera, P. Panchmatia, M.S. Islam, A.R. Slater, Fuel Cells 11 (2011) 38.
50. H.G. Scott, J. Mater. Sci. 10 (1975) 1527.
51. D.J.L. Brett, A. Atkinson, N.P. Brandon, S.J. Skinner, Chem. Soc. Revi. 37 (2008) 1568.
52. V.V. Kharton, E.N. Naumovich, A.A. Vecher, J. Solid State Electr. 3 (1999) 61.
53. A. Orera, P.R. Slater, Chemistry of materials 22 (2010) 675.
54. E R. Losilla, M.A.G. Aranda, I. Santacruz, L. Santos-Gomes, J. M. Porras Vazquez, Ceram. Int. 2012, 38, 3327-3335.
55. S. Omar, E.D. Wachsman, J.L. Jones, J.C. Nino, J. Am. Ceram. Soc. 92 (2009) 2674.
56. H.L. Tuller, A.S. Nowick, J. Electrochem. Soc. 122 (1975) 255.
57. L. Leon-Reina, J.M. Porras-Vazquez, E.R. Losilla, D.V. Sheptyakov, A. Llobet, M.A.G. Aranda, RSC Dalton Trans. 20 (2007) 2058.
58. H. Yoshioka, S. Tanase, Solid State Ionics 176 (2005) 2395.
59. D. Marrero-Lopez, M.C. Martin-Sedeno, J. Pena-Martinez, J. Ruiz-Morales, P. Nunez, M.A.G. Aranda, J.R. Ramos-Barrado, J. Power Sources 195 (2010) 2496.
60. A. Orera, P.R. Slater, Chem. Mater. 22 (2010) 675.
61. E. Kendrick, A. Orera, P.R. Slater, J. Mater. Chem. 19 (2009) 7955.
62. H. Gasparyan, S. Neophytides, D. Niakolas, V. Stathopoulos, T. Kharlamova, V. Sadykov, O. Van der Biest, E. Jothinathan, E. Louradour, J.P. Joulin, S. Bebelis, Solid State Ionics 192 (2011) 158.
63. J.R. Tolchard, M.S. Islam, P.R. Slater, J. Mater. Chem. 13 (2003) 1956.
64. E. Kendrick, M.S. Islam, P.R. Slater, J. Mater. Chem. 17 (2007) 3104.
65. E. Kendrick, J. Kendrick, A. Orera, P. Panchmatia, M. S. Islam, A.R. Slater, Fuel Cells 11 (2011) 38.
66. P.R. Slater, J.E.H. Sansom, J.R. Tolchard, Chem. Rec. 4 (2004) 373.
67. E. Bechade, O. Masson, T. Iwata, I. Julien, K. Fukuda, P. Thomas, E. Champion, Chem. Mater. 21 (2009) 2508.
68. H. Yoshioka, Y. Nojiri, S. Tanase, Solid State Ionics 179 (2008) 2165.
69. J.M. Porras-Vazquez, E.R. Losilla, L. Leon-Reina, D. Marrero-Lopez, M.A.G. Aranda, J. Am. Ceram. Soc. 92 (2009) 1062.
70. N. Jiang, R.M. Buchanan, D.A. Stevenson, W.D. Nix, J.Z. Li, J.L. Yang. Mater. Lett. 22 (1995) 215.

71. T. Takahashi, T. Esaka, Iwahara, J. Appl. Electrochem. 5 (1975) 197.
72. T. Takahashi, H. Iwahara, Mater. Res. Bullet. 13 (1978) 1447.
73. T. Takahashi, H. Iwahara, T. Arao. J. Appl. Electrochem. 5 (1975) 187.
74. N. Jiang, E.D. Wachsman, S.H. Jung, Solid State Ionics 150 (2002) 347.
75. G. Pasciak, K. Prociow, W. Mielcarek, B. Gornicka, B. Mazurek, J. Euro. Ceram. Soc. 21 (2001)1867.
76. S. Lazure, C. Vernochet, R.N. Vannier, G. Nowogrocki, G. Mairesse, Solid State Ionics 90 (1996) 117.
77. A.A. Yaremchenko, V.V. Kharton, E.N. Naumovich, A.A. Tonoyan, Mater. Res. Bullet. 35 (2000) 515.
78. F. Krok, I. Abrahams, M. Malys, W. Bogusz, J.R. Dygas, J.A.G. Nelstrop, A. J. Bush, Solid State Ionics 136-137 (2000)119.
79. C. Pirovano, R.N. Vannier, E. Capoen, G. Nowogrocki, J.C. Boivin, G. Mairesse, M. Anne, E. Dooryhee, P. Strobel, Solid State Ionics 159 (2003)167.
80. F. Abraham, J.C. Boivin, G. Mairesse, G. Nowogrocki, Solid State Ionics 40-41 (1990) 934.
81. F. Goutenoire, O. Isnard, R. Retoux, P. Lacorre, Chem. Mater. 12 (2000) 2575.
82. A. Subramania, T. Saradha, S. Muzhumathi, J. Power Sources 167 (2007) 319.
83. H. Hayashi, T. Saitou, N. Maruyama, H. Inaba, K. Kawamura, M. Mori, Solid State Ionics 176 (2005) 613.
84. D. Marrero-López, J.C. Ruiz-Morales, D. Pérez-Coll, P. Nunez, J.C.C. Abrantes, J.R. Farade, J. Solid State Electr. 8 (2004) 638.
85. T.L. Nguyen, M. Dokiya, S. Wang, H. Tagawa, T. Hashimoto, Solid State Ionics 130 (2000) 229.
86. V.V. Kharton, A.L. Shaula, M.V. Patrakeev, J.C. Waerenborgh, D.P. Rojas, N.P. Vyshatko, E.V. Tsipis, A.A. Yaremchenko, F.M.B. Marques, J. Electrochem. Soc. 151 (2004) A1236.

Chapter 2 Literature review

This chapter deals with the literature review on undoped and doped vanadium-based systems. The physical, structural, optical, thermal and conducting properties of these materials are discussed in light of various processing parameters, dopants and their concentrations. Based on literature review, the motivation of the present study along with objectives are also given in the last of this chapter.

2.1 Crystal structure of V_2O_5

Vanadium oxide is a complex class of materials and exhibited layered-type crystal structure as shown in Fig. 1 [1, 2, 3]. V_2O_5 crystal structure consists of weakly bonded layers but has orthorhombic symmetry. It comprises of zigzag double chains bonded with oxygens.

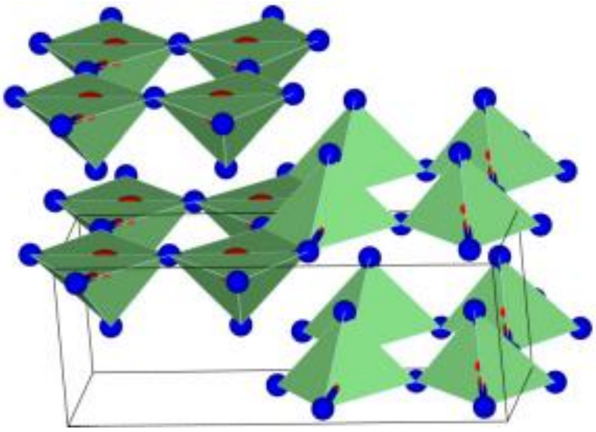

Fig. 2.1 Crystal structure of vanadium pentoxide (V_2O_5): large red spheres inside the nearest neighbor coordination pyramids represent vanadium ion (V), small blue spheres represent oxygen ion (O) [3].

The structure of vanadium oxide can be viewed as consisting of chains of square-based pyramids of five oxygens surrounding each V. This point alternately up and down and share an edge along the chain direction and these double chains are connected through a corner shared bridge oxygen. Hence, it has three different types of oxygen in this structure. The vanadyl oxygen (O_v) is bonded with a single vanadium which forms the apex of the pyramids. The bridge oxygen (O_b) is bonded with the two vanadium and couples the chains together. While the chain oxygen (O_c) connects with three vanadium, two along the chain direction and one in the adjacent chain. Therefore, they form the shared edge between the pyramids in the double chain. Thus, it can be manifested itself in the electronic and transport properties of the systems [3]. It exists in various chemical forms such as VO, V_2O_3, VO_2, V_4O_9 and V_2O_5 in which last one is the most stable form chemically and thermally than other allotropes of vanadate [4]. Therefore, vanadium oxide specially V_2O_5 has been used for several solid-state devices such as high capacity lithium ion batteries, catalysts, smart windows, gas sensor and many more applications [5, 6]. Moreover, vanadates have been used as engineering materials due to their better electrical properties at low temperature [7]. V_2O_5 is the predominantly electronic conductor and electrical conduction arises due to hopping of unpaired electron ($3d^1$) between V^{4+} and V^{5+} states, leading to the formation of a small polaron [8]. Additionally, oxygen vacancies could be generated with the doping of lower valance cations, which would help to enhance the ionic conductivity and make them mixed ionic-electronic conductor (MIEC) [9]. Moreover, various properties of the vanadate could be tuned mainly by compositional changes and processing parameters and depend on the chemical nature and concentration of the dopants [10, 11]. The structure of vanadate is also played a very crucial role in the transport process owing to ions surrounding vanadium-oxygen polyhedral, which leads to change in the hopping mechanism.

2.2 Effect of dopants on various properties

Alhajry *et al.* [8] investigated the effects of composition on the physical, structural, thermal and electrical properties of barium doped vanadate systems of composition xBaO-(100-x)V_2O_5 (where, x=30, 35, 40, 45, 50 mol%). It is observed that density increases (3.69-3.91 gcm^{-3}) with increasing barium oxide content whereas molar volume decreases (46.96-42.86 cm^3mol^{-1}). In addition to this, vanadium ion concentration decreases while inter-ionic distance increases with increasing content of BaO. The increase in glass transition temperature indicates the formation of complicated network structure in the glassy matrix with increasing BaO content. The Fourier transform infrared spectroscopy results of the systems indicate that the network is built up of mainly VO_4 polyhedra.

The dc conductivity is observed in the range of 0.02 Sm^{-1} to 0.007 Sm^{-1} at 140 ˚C. Whereas the activation energy is in the range of 0.35-0.95 eV. Finally, they found that all the properties are depends on the chemical nature of the dopant.

Gouda *et al.* [12] synthesized manganese doped vanadium and found that the resistivity of the mixed phase $Mn_2V_2O_7$ is higher than vanadium and binary/ternary oxides of manganese, nickel and cobalt. Manganese vanadate with monoclinic crystalline structure in brannerite-type MnV_2O_6 is produced through solid state reaction at an elevated temperature between manganese and vanadium oxide. The activation energy is in the range of 0.12-0.17 eV for the thermistor sample with structure MnV_2O_6. It suggests the small polaron hopping process in these samples. MnO_2, V_2O_5 and MnO_2 doped V_2O_5 have been used to compared their conductivity [13]. It is observed that MnO_2 has higher ac conductivity ($23\times10^{-3}Sm^{-1}$) than V_2O_5 ($1.23\times10^{-3}Sm^{-1}$) at 40 Hz frequency and 250 °C temperature. On the other hand, the ac conductivity of the MnO_2 doped V_2O_5 samples sintered at 500 and 550 ºC falls between undoped MnO_2 and V_2O_5, respectively. Also, samples sintered at 550 ºC shows lower ac conductivity than sintered at 500 ºC, which can be associated with the higher phase purity of MnV_2O_6 in sample sintered at 550 ºC. In addition, MnO_2 has higher activation energy (0.81 eV) than V_2O_5 (0.34 eV) at 1MHz frequency. The activation energy of MnO_2 doped V_2O_5 samples sintered at 500 °C (0.19 eV) is higher than sintered at 550 °C (0.14 eV) for 1MHz frequency. Khattak *et al.* [14] synthesized (1-x)SrO-xV_2O_5 (x=0.5-0.8) compositions have been prepared by melt and quench method. An attempt has been made to understand the doping effect of vanadium oxide on structure and electrical properties to understand the nature of the mechanism governing the dc electrical conductivity. Sr-vanadate systems, with 20 mol% SrO and greater would comprise of mixture of VO_5 groups (Probably trigonal bipyramids) and VO_4 metavanadate chains with the Sr^{2+} ions occupying interstitial sites between these chains. It is observed that dc conductivity increases from 5.3×10^{-5} to 2.6×10^{-1} Sm^{-1} at 127 ˚C whereas the activation energy decreases from 0.59 to 0.22 eV with the addition of vanadium oxide content in these systems. Another samples with compositions (100-x)-V_2O_5-xCaO (x=30-50 mol%, with step size 5) have been prepared by the melt-quench method to study their physical, structural and electrical properties [15]. The density decreases from 3.96 to 3.75 gcm^{-3} while molar volume increases from 29.99 to 38.43 cm^3mol^{-1} with the addition of CaO content in place of V_2O_5. The dc conductivity shows decreasing trend from 4.8×10^{-1} to 1.06×10^{-2} Sm^{-1} at 50 ˚C with increasing content of CaO. While activation energy shows increasing trend (0.43-0.53 eV) with increasing dopant concentration of CaO. The multi-phase material of Mn-V oxide (MnV_2O_6, $Mn_2V_2O_7$, MnO_2) has been successfully prepared by solid state reaction method. According to XRD study, the MnV_2O_6 and $Mn_2V_2O_7$ are the Mn-V oxide which is 61.7% and 19.3%, respectively. The starting material (MnO_2) is remained around 19%. Mn-V oxide shows low conductivity (10^{-6} to 10^{-9} Sm^{-1}) which is same as for insulator at low temperature [16]. The ac conductivity shows increasing trend with increasing frequency as temperature rises, consequently, ac conductivity is a thermally activated process. Apparently, at 40 Hz, ac conductivity is almost the same as dc conductivity the lowest value of conductivity is 59.66×10^{-9} Sm^{-1} at 50 °C whereas the highest value is found to be 41.43×10^{-6} $S\,m^{-1}$ at 250 °C. The activation energy of ac conduction decreases with an increase in frequency due to dominating of hoping mechanism. The highest activation energy of ac conduction at 40 Hz is 0.50 eV, which is lower than the activation energy of dc conduction (0.54 eV). Structural and physical properties of (100-x)MgO-xV_2O_5 (where, x=60, 70, 80, 90) compositions prepared by melt and quenched process have also been studied by Sen *et al* [17]. The presence of both V^{5+} and V^{4+} ions is confirmed in all the samples. The density of the prepared samples decreases from 2.93 to 2.92 gcm^{-3} with increasing V_2O_5 in place of MgO. While molar volume is found to be increased. The average vanadium site separation, glass transition temperature and crystallization temperature are found to be decreased with increasing concentration of V_2O_5 on the cost of MgO. Infrared studies confirmed that the glass network is built up of mainly VO_4 polyhedra. Tsuzuki *et al.* [18] synthesized rapidly quenched glasses in the V_2O_5-MO (M =Mg, Ca and Ba) systems by a twin-roller method. the structural changes in the system have been charecterized by IR spectroscopy. The electrical properties of V_2O_5-MO (M =Mg, Ca and Ba) systems has been studied in context to the structural changes. The electrical conduction in the vanadate glasses is predominantly electronic due to hoping of electron between V^{5+} and V^{4+} ions by the V-O-V bond. The electrical conductivity is influenced by the concentration of V^{4+} ions and the number of the V-O-V hopping path. Though, the concentration of V^{4+} ions is too small as confirmed by the thermogravimetric (TG) measurements. The concentration of V^{4+} ions decrease with increasing dopant, as the color change is observed for the systems. The V-O-V bonds are responsible for the electron hopping, it decreases with increasing dopant, which is associated with the structural change of the systems. The glass-formation regions in the Ca and Ba containing systems were found to be little wider as compared to Mg containing systems. The crystallization temperature of the glasses increases with increasing MO content. No metastable phase was observed to form in the crystallization processes. In the TG measurements, there is no weight change observed that confirmed no oxidation and reduction of the vanadium ion is taken place in the systems. The electrical conductivity of all the prepared samples is found to be decreased with increasing MO content (M =Mg, Ca and Ba). The V_2O_5-MgO systems show electrical conductivity in the of 6.1×10^{-4} to 2.0×10^{-1} Sm^{-1} at 200 ˚C. While the V_2O_5-CaO systems exhibit electrical conductivity in the of 6.1×0^{-4} to 2.0×10^{-1} Sm^{-1} at 200 ˚C. On the other hand, the V_2O_5-BaO systems have electrical conductivity in the of 5.5 to 6.1×10^{-3} Sm^{-1} at 200 ˚C. The activation energy for the V_2O_5 glass was 0.40 eV, which increases with increasing x. The activation energies for the glasses of x = 0.20 were about 0.42 eV in all the three systems. But the activation energies for x=0.40 and 0.50 in the V_2O_5-BaO system is about 0.70 eV, which is much higher than 0.50 eV for the glasses of the same x in the other two systems.

Chakrabarty *et al.* [19] studied the doping effect of Na^{1+} on conducting properties of V_2O_5 systems and found an enhancement in conductivity (0.05×10^{-1}-19.5×10^{-2} Sm^{-1}) with increasing concentration of Na^{1+} at room temperature. Furthermore, Ag^{1+}, Cu^{2+}, Fe^{3+}, Al^{3+} and Na^{1+} as dopant improves the electrochemical behavior of the V_2O_5, while Ag^{1+}, Na^{1+} and Li^{1+} doping decreases the optical band gap of the V_2O_5 [20-23]. Thin films of V_2O_5 were deposited on glass substrate using thermal evaporation method by Raja *et al* [24]. They studied structural and optical properties of the prepared thin films. The optical band gap was found to decrease from 2.40 eV (110 nm) to 2.02 eV (365 nm) with increasing thickness of the film. the composition xV_2O_5-$(1-x)TeO_2$ (where, x=50, 60, 70 ,80 mol%) has been prepared by melt and quench method at 900 ˚C. After that prepared samples were annealed about 250°C causes the appearance of a crystalline phase resulting in an increase in conductivity. The dc conductivity of semiconducting vanadium tellurite systems has been obtained in the temperature range between -196 to 127 ˚C. The conductivity of V_2O_5-TeO_2 systems is slightly higher than the corresponding composition of V_2O_5-P_2O_5 systems. The conductivity shows increasing trend whereas activation energy decreases in glass-ceramics. The increase in conductivity and decrease in high temperature activation energy with increasing content of V_2O_5 is similar in both the systems. It is observed that the crystallization temperature decreased with increasing concentration of V_2O_5 content [25]. Chung and Mackenzie [26] have been found crystallization in V_2O_5-TeO_2 glasses at about 270 °C. The density of the samples decreases from 4.25 to 3.99 gcm^{-3} while ionic concentration increases from 1.49 to 2.16×10^{22} cm^{-3} with increasing concentration of V_2O_5. The dc conductivity found to be highest 2.4×10^{-3} Sm^{-1} with the highest content of V_2O_5 (80 mol%) whereas activation energy found to be lowest i.e. 0.23 eV at 27 ˚C. Flynn *et al.* [27] has been observed the highest dc conductivity (1.31×10^{-3} Sm^{-1}) and lowest activation energy (0.25 eV) at -73 ˚C temperature for 50 mol% of V_2O_5. Iwanaga *et al.* [28] investigated electrical conductivity of sodium doped vanadium pentoxide thin film prepared by a solution method. X-ray diffraction (XRD) results revealed successive incorporation of Na^+ to V_2O_5, forming β-Na$x$$V_2O$ ($0.22\leq x\leq 0.4$) together with γ phase at annealing below 400 °C temperatures. The pure V_2O_5 thin film sample has an electrical conductivity of 4×10^{-2} Sm^{-1}. The electrical conductivity dramatically increased by a factor of ∼10^4 with Na doping. Electrical conductivity is increased due to the increase in the polaron hoping and the reduction of the activation energy due to formation of β-Na$x$$V_2O$ phase. Turkoglu *et al.* [29] have been discussed electrical conductivity of V_2O_5 doped Bi_2O_3systems in the composition range of 1-7 mol% of V_2O_5 at different temperatures. Phase transformation is also studied with compositions variation and change in process parameters. The body centered cubic (bcc) type solid solution was stable up to 720°C and the solubility limit was found at ∼7 mol% V_2O_5 in γ-phase of Bi_2O_3. The γ-form changes into δ-form which gives and endothermic peak in DSC/DTA at 720°C and then δ-form melted at 832°C. The electrical conductivity of γ-Bi_2O_3 doped V_2O_5 (1-7 mol%) is increased with increasing temperature up to about 700°C and then sharply decreased up to about 720°C, after that electrical conductivity is increased quickly up to about 820°C. A marked drop in total conductivity between 700 and 720°C is ascribed to the phase transition from γ-Bi_2O_3 to δ-Bi_2O_3. The electrical conductivity of V_2O_5 doped γ-Bi_2O_3 systems have been increased with the addition of vanadium ion and reaches to a maximum for 5 mol% V_2O_5. The conductivity values are 3.5 and 2.8×10^{-1} Sm^{-1} at 600 and 400°C, respectively which is due to the intermediary role of interstitial oxygen ions. The highest ionic conductivity (8.31 Sm^{-1}) is observed for 5 mol% of V_2O_5 at 700°C. The obtained activation energy values are found to be approximately constant (0.652-0.654 eV) for all the samples. Chakraborty *et al.* [30] prepared thin films of V_2O_5-Sb_2O_3 by vacuum evaporation method. The molar ratio of V_2O_5:Sb_2O_3 was 100:0, 98:2, 94:6, and 92:8, respectively. The dc conductivity and activation energy of the film was obtained in the temperature range of 30-150 ˚C. The conductivity was decreased with Sb_2O_3 content from 8.12×10^{-3} to 2.47×10^{-4} Sm^{-1} whereas activation energy was increased with Sb_2O_3 content from 0.36 to 0.43 eV in the temperature range of 30-150 ˚C. Sinha [31] studied structural, optical and electrical properties of W-doped V_2O_5 (x)W-(1-x)V_2O_5, x = 3 wt%) nanostructured films synthesized by pulsed laser deposition (PLD) technique. There is a strong influence of deposition temperature has been occurred on structural, optical and electrical properties of W-doped vanadium pentoxide nanostructured thin film. The films deposited at 150 ˚C temperature exhibits amorphous nature with diffused hollow diffraction patterns whereas the films show crystalline nature with an increase in deposition temperature. The direct optical band gap of the films is decreased from 2.61 eV (at 350 ˚C) to 2.18 eV (at 150 ˚C). The electrical conductivity of the W-doped V_2O_5 films is found to be 24 Sm^{-1} at room temperature and approaches 145 Sm^{-1} at 277 ˚C. It is much higher than that of bulk V_2O_5 (10^{-2} Sm^{-1}) [32]. The activation energy is found to be 0.049, 0.0513, 0.0697 eV deposited at 150 ˚C, 250 ˚C and 350 ˚C, respectively. Sen *et al.* [33] have been prepared samples of compositions (100-x)MgO-(x)V_2O_5, where x=50-90 mol%. They studied the composition effect on physical thermal and electrical properties of vanadium doped magnesium. It is observed that the conductivity increases whereas the activation energy decreases with increasing vanadium oxide content into magnesium oxide. The density of the prepared sample is highest (2.94 gcm^{-3}) for the highest content of V_2O_5 (50 mol%). The ionic concentration decreases from 1.89×10^{22} to 1.59×10^{22} cm^{-3} while inter-ionic distance increases from 0.375 to 0.397 nm with increasing content of vanadium oxide. The high temperature activation energy is found to be decreases from 0.57 eV to 0.36 eV while conductivity is found to be increases from 0.0003 to 0.008 Scm^{-1} at 100 ˚C temperature. Seethalakshmi *et al*. [34] have prepared Al_2O_3-V_2O_5 solid solution under solid sintering at 600 ºC lead to the liquid phase sintering 850 ºC. The solid-state sintering leaves a very porous network of dense alumina particles surrounded by smaller facetted vanadia. While in liquid phase sintering, the V_2O_5 recrystallizes over the relatively inert Al_2O_3, resulting connected network structure. The ac conductivity of the sintered pellets was investigated from room temperature to 400 ºC. The dc conductivity values for the solid-state phase sintering and liquid phase sintering are found to be similar at room temperature. The dc conductivity of solid-state sintered pellets for room temperature is 10^{-5} Sm^{-1} and for 600 ºC is 0.01 Sm^{-1}. The dc conductivity of liquid phase sintered pellets for room temperature is 10^{-5} Sm^{-1} and for 600 ºC is 0.01 Sm^{-1} for 600 ºC. The activation energy of dc conduction for solid state sintering pellets are found to be 0.45 eV from room temperature to 230 ºC and 0.25 eV from 230 ºC to 380 ºC, respectively. While the activation energy of dc conduction for liquid state sintering pellets are found to be 0.35 eV from room temperature to 380 ºC. Bi_2O_3 doped V_2O_5 systems ($Bi_4V_2O_{11}$, BIVOX) have been shown good conductivity ($\sim 0.2\times10^2$ Sm^{-1}) at 500 °C temperature [35]. This high conductivity at lower temperature is associated with unique structure and properties of $Bi_4V_2O_{11}$ phase. The BIVOX having Aurivillius-type structure with alternating layers of $(Bi_2O_2)^{2+}$ and $[VO_{3.5-\delta}Ve_{0.5-\delta}]^{2-}$ (where, Ve represents an oxide ion vacancy). The bismuthate layers are sandwiched between the vanadate layers. The oxide ion conductivity associated with the vacancies in the vanadate layers. In $Bi_4V_2O_{11}$, the bismuthate layers are remaining unchanged [36]. However, various vacancies are spread over the perovskite (vanadate) layers. The rate of oxygen vacancies is 12.5% in the perovskite layer [37-39]. The conductivity is the highest ever reported for an oxide ion conductor ($\sigma_{600°C}=0.2\times10^2$ Sm^{-1}).

In view of this, the $Bi_4V_{2-x}Co_xO_{11-\delta}$ (0.0-0.2) compositions have been prepared by Kim *et al.* [39] and they found that the high conducting γ phase is stabilized at room temperature for x=0.2. It also shows electrical anisotropy between the directions parallel and perpendicular to $(Bi_2O_2)^{2+}$ layers in which conductivity in the direction parallel to $(Bi_2O_2)^{2+}$ layers are three times greater than perpendicular direction. The high conducting γ- phase is also stabilized at room temperature in $Bi_2V_{0.9}Co_{0.1}O_{5.35}$ with small grain size [40]. Similarly, $Bi_2V_{1-x}Ni_xO_{5.5-\delta}$ system also shows high conducting γ- phase stabilization above x = 0.10. The conductivity is 0.12×10^2 Sm^{-1} at 300 °C for x =0.12 [41]. Krok *et al.* [42] have been reported that oxide ion vacancies are exclusively to equatorial position around Ni/V atoms. The ionic conductivity of $Bi_{2-x}La_xV_{1-y-z}Cu_yNi_zO_{5.5-\delta}$ (x=0.10-0.20; y=0-0.10; z=0.0-0.20) systems have been decreased with lanthanum (La) and nickel (Ni) doping. La_2O_3-doped $Bi_4V_2O_{11}$ compound show an increasing trend in conductivity and melting point with increasing content of La_2O_3. Jacobsoone *et al.* [43] have been developed a new family of compounds namely BIMEVOF (where ME = ZnF_2; BIZNVOF) in which a mixed anion phase is formed on the substitution of oxygen by fluorine. It is observed that the oxygen vacancies decrease with ZnF_2 doping whereas thermal stability increases. The $Bi_2V_{1-x}Zn_xO_{5.5-x/2}$ (x=0.0-0.27) system shows highest conductivity (4×10^{-1} Sm^{-1}) at 300 ºC for x= 0.10 [44]. The doping of rare earth elements such as Nd, Gd, Er and Yb in $Bi_{4+y}V_{2-x-y}M_xO_{11-y-x}$ gives the maximum conductivity about 2×10^{-2} Sm^{-1}at 300 °C for y = 0.0 and x = 0.2 [45]. The substitution of Ge at V site in $Bi_2V_{1-x}Ge_xO_{5.5-x/2}$ (where x=0.2-0.6) has been shown phase transition from orthorhombic to tetragonal and tetragonal to orthorhombic with increasing dopant concentration. The high conducting γ- phase is stabilized only for x = 0.4 [46]. On the other hand, the substitution of Cu at V site in $Bi_4V_{2-x}Cu_xO_{511-x}$ (x=0.07-0.20) has been shown high electrical conductivity in the temperature range of 100-400 °C. While, the conductivity above x=0.15, decreases as the interaction between defects increases [47]. The conductivity of the CuF_2 substituted BIMEVOX; $Bi_2V_{1-x}Cu_xO_{5.5-5x/2}F_{2x}$ (BICUVOF, $0.10 \leq x \leq 0.20$) systems are found to decrease which can be associated with that the fluorine does not enter into the defect layers as BIZNVOF [48]. The comparison of $Bi_4Cu_{0.2}V_{1.8}O_{11-x}$ and $Bi_4Co_{0.2}V_{1.8}O_{11-x}$ systems has been done by Guillodo *et al.* [49]. It is observed that Cu-doped system shows pure oxide ionic conductivity whereas Co-doped system shows p-type conductivity. The conductivity of the Cu-doped system was found to be 2 to 3 order higher than Co-doped system. In other report, Guillodo *et al.* [50] have been reported higher conductivity for $Bi_4Cu_{0.2}V_{1.8}O_{11-x}$ and $Bi_4Co_{0.2}V_{1.8}O_{11-x}$ systems as compared to yttria stabilized zirconia (YSZ) and gadolinium doped ceria (GDC) conventional electrolytes. However, their oxygen surface exchange coefficient was found to low. In another study, the n-type electronic conductivity in $Bi_4Cu_{0.2}V_{1.8}O_{11-x}$ system increases on reducing partial pressure up to 10 kPa with decomposition of γ- phase. While, neither the electron-hole conduction nor the decomposition of γ- phase are observed during the annealing at 12 MPa pressure. Furthermore, the increase in partial pressure lowers the conductivity due to the higher pressure. Moreover, it is increased the ordering of oxygen vacancies [51]. In another report, the effect of Mg doping in $Bi_2Mg_xV_{1-x}O_{5-3x/2}$ ($0.05 \leq x \leq 0.40$) systems has been investigated. It is observed that the secondary phase at x = 0.40 is observed. The high conducting γ- phase is stabilized in the magnesium range $0.13 \leq x \leq 0.25$ whereas below and above this composition range the orthorhombic β-phase is observed [52]. The substitution of P for Bi site in $Bi_4V_{2-x}P_xO_{11}$ ($0.05 \leq x \leq 0.50$) compositions has not been shown high conductivity γ- phase stabilization. But, a secondary phase (BiPO4) has also been occurred. Therefore, the conductivity is less dependent on the concentration of P [53]. Paydar *et al.* [54] prepared Ti and Ti-Cu substituted $Bi_2V_{1-x}Ti_xO_{(11-x)/2}$ (BITIVOX, $0.085 \leq x \leq 0.15$) and $Bi_2V_{0.9}Cu_{0.1-x}Ti_xO_{5.35+x}$ (BICUTIVOX, $0 \leq x \leq 0.1$). In the case of BICUTIVOX, the conductivity increases whereas activation energy decreases with decreasing content of Ti. The $Bi_2V_{0.9}Cu_{0.1}Ti_xO_{5.35}$ and $Bi_2V_{0.9}Cu_{0.05}Ti_{0.05}O_{5.4}$ show the highest conductivity at different temperatures. The BICUTIVOX compound shows higher electronic contribution at high temperature as compared to BITIVOX compound. The conductivity of the

$Bi_4V_{1.8}Cu_{0.2-x}Nb_xO_{10.7+3x/2}$ (x =0.05-0.15) compositions increase with increasing content of Nb. The maximum conductivity has been reported for x = 0.5 system [55]. The conductivity is supposed to be on higher side as compared to the $Bi_4V_{1.8}Cu_{0.2}O_{10.7}$. In order to get high conductivity at lower temperature, a thin film of $Bi_2V_{0.9}Cu_{0.1}O_{5.35}$ composition has been deposited on a glass substrate by spray pyrolysis method. The thin film shows good electrical conductivity about 5.7 Sm^{-1} at 475 °C, which can be used for IT-SOFC application [56]. In another case, the same composition thin film ($Bi_2V_{0.9}Cu_{0.1}O_{5.35}$) has been deposited on an alumina substrate. The thermal studies are confirmed desired phase formation at 650 °C. The electrical conductivity reveals grains contribution on large scale, which is studied by impedance spectroscopy. The temperature-dependent conductivity behavior confirms the use of $Bi_2V_{0.9}Cu_{0.1}O_{5.35}$ thin film in low temperature SOFCs application [57]. But it is observed that this thin film shows better electrical conductivity for alumina than glass substrate for SOFC applications. The effect of Cd doping in $Bi_4V_{2-x}Cd_xO_{11-\delta}$; ($0 \leq x \leq 0.25$) system has been investigated by Beg *et al.* [58]. The high conducting γ-phase is stabilized at $x \geq 0.175$ and the highest conductivity (about 1.30×10^{-2} Sm^{-1} at 420 °C) is observed for x = 0.20. On the other hand, Al doping in $Bi_4V_{2-x}Al_xO_{11-\delta}$ ($0 \leq x \leq 0.4$) systems shows the highest conductivity for x = 0.2 and then decreases. In addition to this, the samples with x=0.2 has been sintered at 750, 800 and 825 °C because processing parameters also effects the conductivity. The highest conductivity is observed for the sample sintered at 800 °C for 12h [59]. In another study, a series of Zr, Ga and Fe substitution for V site in $Bi_4(V_{1-x}Mx)_2O_{11-y}$ (x = 0-0.3, M=Zr, Ga, Fe) system has been prepared by the solid-state reaction method. It is observed that electrical conductivity decreases with increasing value of x for all the samples. Malys *et al.* [60] have been reported the effect of temperature on the $Bi_2V_{0.7}Mg_{0.3}O_{5.395-\delta}$ system and they found a phase separation above 650 °C. However, the $Bi_2V_{0.7}Mg_{0.3}O_{5.395-\delta}$ phase is prepared at 840 °C and can also be preserved on cooling. This phase shows low value of conductivity which can be due to the trapping of oxygen ions in V^{5+} and Mg^{2+}. The Ce doping for V site in $Bi_4V_{2-x}Ce_xO_{11-x/2-\delta}$ ($0.0 \leq x \leq 0.30$) systems has been studied by Beg *et al.* [61]. It has been observed that the conductivity of the prepared samples decreases upto x = 0.25. This decrease in conductivity reveals the anisotropic interaction between Ce^{4+} ion and oxide ion vacancy. At, high temperature, the conductivity decreases with dopant concentration [62]. The effect of doping concentration of Hf with same valence as that of Ce has also studied. The $Bi_4V_{2-x}Hf_xO_{11-x/2-\delta}$ ($0.0 \leq x \leq 0.40$) systems have been prepared via solid state reaction method. It is observed that the low temperature conductivity decreases accompanying the increase in activation energy. A series of La and Gd doping at Bi site in $Bi_{4-x}M_xV_2O_{11}$ ($0 \leq x \leq 0.4$) compositions has been prepared by the solid-state route. The total conductivity of the prepared samples increases with increasing dopant concentration which is associated with the increasing disorder in the system [63].

The conductivity behaviour of the Ti^{3+} doped bismuth vanadate ($Bi_4V_{2-x}Ti_xO_{11-\delta}$; $0 \leq x \leq 0.4$) has been investigated [64]. The conductivity of the prepared samples increases with increasing Ti^{3+} ions. The $Bi_4V_{1.6}Ti_{0.4}O_{11-\delta}$ compound shows the highest conductivity when sintered at 800 °C for 12h. Taninouchi *et al.* [65] investigated the behaviour of Li and Ag doped $Bi_2VO_{5.5}$ system. The conductivity of the samples increases with increasing dopants concentration. It is observed that the samples prepared at 500 °C shows better conductivity as compared to well-known ionic conducting systems ($La_{0.8}Sr_{0.2}Ga_{0.8}Mg_{0.115}Co_{0.085}O_3$). Though, the co-doping usually increases the coefficient of thermal expansion. The Ba doping at V site for $Bi_4Ba_xV_{2-x}O_{11-3x/2-\delta}$; ($0.07 \leq x \leq 0.30$) systems has been investigated [66]. The conductivity is increased with dopant concentration and the highest conductivity (about 4.45×10^{-3} Sm^{-1} is observed for x = 0.17 at 300 °C. In another study, the effect of Na doping in bismuth vanadate system ($Bi_2V_{1-x}Na_xO_{5.5-2x}$; $0 \leq x \leq 0.20$) prepared via sol- gel method has been studied [67]. The highest conductivity about 1.34×10^{-3} Sm^{-1} is observed at 300 °C for x = 0.13 sample. The doping of

Ca for V site in $Bi_4Ca_xV_{2-x}O_{11-3x/2-\delta}$; $0.07 \le x \le 0.30$ has been studied. It is observed that the conductivity of the samples increases with increasing doping of Ca due to the increasing disordering in the systems [68]. The structural and conducting properties of $Bi_4V_{2-x}Ga_xO_{11-\delta}$; $0 \le x \le 0.4$ systems are studied and found that the conductivity increases with increasing Ga doping for $x<0.2$ and then decreases due to the formation of impurity phase (secondary phases) [69]. The solid solutions of the $Bi_4V_{2-x}Me_xO_{11-\delta}$, (Me=Fe, Cr, Nb) compositions has been prepared by the hydrochemical, mechanochemical citrate-nitrate, and pyrolysis of polymeric-salt compositions route. The γ- phase stabilization is observed for Fe (x=0.2-0.5) and Nb (x=0.2-0.6) doped systems. However, Fe doped samples shows the highest conductivity value [70]. Various vanadium containing systems and conductivity are given in Table 2.1.

Table 2.1 Different compositions vanadate conductivity, reported temperature along with activation energy.

Composition	**Conductivity (Sm^{-1})**	**Temperature (ºC)**	**Activation energy (eV)**	**References**
$30BaO\text{-}70V_2O_5$	2×10^{-2}	140	0.35	8
V_2O_5	1.2×10^{-3}	250	0.34	13
$0.2SrO\text{-}0.8V_2O_5$	26×10^{-2}	127	0.22	14
$70V_2O_5\text{-}30CaO$	4.8×10^{-1}	50	0.43	15
Mn-V	4.1×10^{-7}	250	0.50	16
$V_2O_5\text{-}MgO$	2.0×10^{-1}	200	0.42	18
$V_2O_5\text{-}BaO$	55×10^{-1}	200	0.70	18
$Bi_4V_{1.94}Nb_{0.06}O_{11}$	3.09×10^{-4}	300	1.61	71
$Bi_4V_{1.94}Zr_{0.06}O_{11}$	5.43×10^{-4}	300	2.05	71
$Bi_4V_{1.94}Y_{0.06}O_{11}$	2.61×10^{-4}	300	1.97	71
$Bi_4V_{1.94}Cu_{0.06}O_{11}$	5.78×10^{-4}	300	1.10	71
$Bi_4Ag_{0.30}V_{1.70}O_{10.4-\delta}$	4.56×10^{-2}	300	0.27	72
$Bi_4Mg_{0.26}V_{1.74}O_{10.6}$	1.51×10^{-1}	300	0.68	73
$Bi_4V_{1.9}Li_{0.1}O_{10.8}$	3.98×10^{-3}	300	0.38	74
$Bi_4V_{1.9}Ag_{0.1}O_{10.8}$	6.82×10^{-3}	300	0.49	74
$Bi_4V_{1.8}Li_{0.2}O_{10.6}$	2.57×10^{-2}	300	0.52	74
$Bi_4V_{1.8}Ag_{0.2}O_{10.6}$	2.57×10^{-2}	300	0.85	74
$Bi_4Ca_{0.17}V_{1.83}O_{10.745}$	3.27×10^{-2}	300	0.61	75
$Bi_4Ce_{0.25}V_{1.75}O_{10.875}$	4.81×10^{-4}	300	0.56	76
$Bi_4V_{1.5}Fe_{0.5}O_{10.5}$	1.08×10^{-3}	300	0.78	77
$Bi_4Mg_{0.6}V_{1.4}O_{10.79-\delta}$	2.25×10^{-4}	300	1.01	78
$Bi_4Ba_{0.17}V_{1.83}O_{10.74}$	4.46×10^{-3}	300	0.80	79
$Bi_4Cd_{0.20}V_{1.8}O_{10.7}$	2.05×10^{-2}	300	0.24	80
$Bi_4Sr_{0.20}V_{1.8}O_{10.7-\delta}$	7.70×10^{-2}	300	0.48	81

2.3 Motivation of the present study

According to the above discussion numerous researchers have been reported the doping effect of various dopants along with processing parameters on conductivity and other properties of the vanadate systems. Many techniques have been employed to prepared doped vanadate systems. But as the literature validates melt-quench technique produces more oxygen vacancies and accommodate higher concentration of dopants which directly affect the overall conductivity of doped vanadates. The quenching rate (from high temperature to room temperature) also will help to reduce the vanadium and other transition element dopants in various oxidation states and hence increasing the oxygen vacancies.

Mostly, doped vanadate systems have been prepared by solid state reaction method as observed in the literature survey. Very few reports have been reported on synthesis of doped vanadate systems via melt-quench technique. Moreover, Li_2O and Al_2O_3 containing V_2O_5 is not reported yet as far as our knowledge. Based on this motivation, the objectives of the present study are given below.

2.4 Objectives

- To synthesize $V_{2-x}M_xO_{5-\delta}$ (M=Li_2O, MgO, Al_2O_3 and TiO_2, x=0.05, 0.10, 0.15, 0.20) systems by melt-quench or solid oxide reaction method.
- As prepared samples will be characterized by X-ray diffraction (XRD), thermal analysis, Fourier transform infra-red (FTIR) spectroscopy, scanning electron microscopy (SEM) and impedance spectroscopy for application in SOFC.
- Selected samples will be used for interfacial study with interconnect.

References

1. Z. Luo, Z. Wu, X. Xu, Vacuum 85 (2010) 145.
2. S. Beke, Thin Solid Films 519 (2010) 1761.
3. C. Bhandari, W.R.L. Lambrecht, Phys. Rev. B 91 (2015) 125116.
4. M. Mousavi A. Kompany, N. Shahtahmasebi, M.M. Bagheri-Mohagheghi, Adv. Manuf. 1 (2013) 320.
5. A. Bouzidi, N. Benramdane, A. Nakrela, Mater. Sci. Eng, B 95 (2002) 141.
6. Y. Fujita, K. Miyazaki, C. Tatsuyama, Jpn. J. Appl. Phys. 24 (1985) 1082.
7. S. Mandal, A. Ghosh, Phys. Rev. B 48 (1993) 9388.
8. A. Al-Hajry, A. Al-Shahrani, M.M. El-Desoky, Mater. Chem. Phys. 95 (2006) 300.
9. S. Gupta, K. Singh, Solid State Ionics 278 (2015) 233.
10. R.N. Vannier, E. Pernot, M. Anne, O. Isnard, G. Nowogrocki, G. Mairesse, Solid State Ionics 157 (2003) 147.
11. I. Abrahams, A.J. Bush, F. Krok, G.E. Hawkes, K.D. Sales, P. Thorton, W. Bogusz, J. Mater. Chem. 8 (1998) 1213.
12. G.M. Gouda, C.L. Nagendra, Sensor. Actuat. A 155 (2009) 263-271.
13. T.F. Khoon, J. Hassan, Z.A. Wahab, R.S. Azis, Results Phys. 6 (2016) 420.
14. G.D. Khattak, A. Mekki, M.N. Siddiqui, Solid State Ionics, 211 (2012) 5.
15. N. Tashtoush, A.M.Qudah, M.M. El-Desoky, J. Phys. Chem. Solids, 68 (2007) 1926.
16. T.F. Khoon, J. Hassan, Z.A. Wahab, R.S. Azis, **Eng. Sci. Technol. an Int. J.** 19 (2016) 2081.
17. S. Sen, A. Ghosh, J. Non-Cryst solids, 258 (1999) 29.
18. A. Tsuzuki, K. Kani, K. Watari, Y. Torii, J. Mater. Sci. 28 (1993) 4063.
19. D.K. Chakrabarty, D. Guha, A.B. Biswas, J. Mater. Sci. 11 (1976)1347.
20. F. Coustier, S. Passerini, W.H. Smyrl, Solid State Ionics 100 (1997) 247.
21. M. Giorgetti, M. Berrettoni, W.H. Smyrl, Chem. Mater. 19 (2007) 5991.
22. J. Farcy, S. Maingot, P. Soudan, J.P. Pereira-Ramos, N. Baffier, Solid State Ionics 99 (1997) 61.
23. Y. Iida, Y. Kanno, J. Mater. Process Tech. 209 (2009) 2421.
24. S. Raja, G. Subramani, D. Bheeman, R. Rajamani, C. Bellan, Optik 127 (2016) 461.
25. V.K. Dhavan, A. mansingh. J. Non-Cryst Solids 51 (1982) 87.
26. C.H. Chung, J.D. Mackenzie, J. Non-Cryst Solids 42 (1980) 357.

27. B.W. Flynn, A.E. Owen and J.M. Robertson, Proc. 7th Int. Conf. on Amorphous and liquid semiconductors, ed. W.E. Spear (CICL, Edinburgh, 1977) 678.
28. S. Iwanaga, M. Marciniak, R.B. Darling, F.S. Ohuchi, Journal of applied physics 101 (2007) 123709.
29. Turkoglu, I. Belenli, Journal of Thermal Analysis and Calorimetry 73 (2003) 1001.
30. S. Chakraborty, K. Suzuki, H. Sakata, Materials Letters 34 (1998) 341.
31. S.K. Sinha, Superlattices and Microstructures 125 (2019)88.
32. K. Honma, M. Yoshinaka, K. Hirota, O. Yamaguchi, Mater. Res. Bull. 31 (1996) 531.
33. A.S. Sen, A. Ghosh, J. Appl. Phys. 86 (1999) 278.
34. S. Seethalakshmia, B. Subramanianb, A. Bendavidc, A.K.N. Kumar, Ceram. Int. 43 (2017) 3202.
35. F. Abraham, M. F. Debreuille-Gresse, G. Mairesse, G. Nowogrocki, Solid State Ionics, 529 (1998) 28.
36. J.A. Kilner, Solid State Ionics 8 (1983) 201.
37. B.C.H. Steele, Oxygen ion conductors. In: Takahashi T, editor. High conductivity solid ionic conductors, recent trends and applications, Singapore: World Scientific Publishing Co., 1989: 402.
38. J.C. Boivin, Int. J. Inorg. Mater. 3 (2001) 1261.
39. S.K. Kim, M. Miyayama Solid State Ionics 104 (1997) 295.
40. A. Kezionis, W. Bogusz, F. Krok, J. Dygas, A. Orliukas, I. Abrahams, W. Gebicki, Solid State Ionics 119 (1999) 145.
41. M.C. Steil, J. Fouletier, M. Kleitza, P. Labrune, J. Eur. Ceram. Soc. 19 (1999) 815.
42. F. Krok, I. Abrahams, D. Bangobango, W. Bogusz, J.A.G. Nelstrop, Solid State Ionics 111 (1998) 37.
43. V. Jacobsoone, C. Follet-Houttemane, J.C. Boivin, Solid State Ionics, 607 (1998) 113.
44. C.K. Lee, C.S. Ong, Solid State Ionics 117 (1999) 301.
45. K. Sooryanarayana, T.N. Guru Row, K.B.R. Varma, Mater. Res. Bull. 34 (1999) 425.
46. F. Krok, I. Abrahams, A. Zadrozna, M. Małys, W. Bogusz, J.A.G. Nelstrop, A.J. Bush, Solid State Ionics 119 (1999) 139.
47. P.I. Paulin F., M.R. Morelli, S.C. Maestrelli, Mat. Res. Innovat. 3 (2000) 292.
48. I. Abrahams, J.A.G. Nelstrop, F. Krok, Solid State Ionics 61 (2000) 136.
49. M. Guillodo, J. Fouletier, L. Dessemond, P. Del Gallo, J. Eur. Ceram. Soc. 21 (2001) 2331.

50. M. Guillodo, J.M. Bassat, J. Fouletier, L. Dessemonda, P. Del Gallo, Solid State Ionics 164 (2003) 87.
51. A.A. Yaremchenko, M. Avdeev, V.V. Kharton, A.V. Kovalevsky, E.N. Naumovich, F.M.B. Marques, Mater. Chem. Phys. 77 (2002) 552.
52. F. Krok, I. Abrahams, M. Malys, W. Bogusz, J.R. Dygas, J.A.G. Nelstrop, A.J. Bush, Solid State Ionics 119 (2000) 136.
53. M. Alga, A. Ammar, R. Essalim, B. Tanouti, F. Mauvy, R. Decourt, Solid State Sci. 7 (2005) 1173.
54. M.H. Paydar, A.M. Hadian, G. Fafilek, J. Mater. Sci. 39 (2004) 1357.
55. M. Alga, A. Ammar, B. Tanouti, A. Outzourhit, F. Mauvy, R. Decourt, J. Solid State Chem. 178 (2005) 2873.
56. R.K. Nimat, C.A. Betty, S.H. Pawar, Appl. Surf. Sci. 253 (2006) 2702.
57. R.K. Nimat, R. S. Joshi, S.H. Pawar, Mater. Sci. Eng. B 137 (2007) 93.
58. S. Beg, N.A.S. Al-Areqi, S. Haneef, Solid State Ionics 179 (2008) 2260.
59. R. Kant, K. Singh, O.P. Pandey, Int. J. Hydrogen Energ. 33 (2008) 455.
60. M. Malys, I. Abrahams, F. Krok, W. Wrobel, J.R. Dygas, Solid State Ionics 179 (2008) 82.
61. N.A.S. Al-Areqi, S. Beg, Mater. Chem. Phys. 115 (2009) 5.
62. S. Beg, N.A.S. Al-Areqi Mater. Chem. Phys. 118 (2009) 15.
63. Deepti, R. Kant, M.L. Singla, K. Singh, Curr. Appl. Phys. 9 (2009) 1467.
64. R. Kant, K. Singh, O.P. Pandey, Mater. Sci. Eng. B 158 (2009) 63.
65. Yu-ki Taninouchi, T. Uda, T. Ichitsubo, Y. Awakura, E. Matsubara, Solid State Ionics 181 (2010) 719.
66. S. Beg, S. Hafeez, N.A.S. Al-Areqi, Physica B 405 (2010) 4370.
67. S. Beg, A. Al-Alas, N.A.S. Al-Areqi, Mater. Chem. Phys. 124 (2010) 305.
68. S. Beg, S. Hafeez, N.A.S. Al-Areqi, Phase Transitions 83 (2010) 169.
69. R. Kant, K. Singh, O. P. Pandey, Ionics 16 (2010) 277.
70. M.V. Morozova, E.S. Buyanova, Ju. V. Emelyanova, V.M. Zhukovskiy, S.A. Petrova, Solid State Ionics 192 (2011) 153.
71. M. Roy, S. Sahu, A. Awasthi, S. Bharadwaj, J. Therm. Anal. Calorim. 115 (2014) 1265.
72. N.A.S. Al-Areqi, S. Beg, A. Al-Alas, J. Phys. Chem. Solids 73 (2012)730.
73. F. Krok, I. Abrahams, M. Malys, W. Bogusz, J.R. Dygas, J.A.G. Nelstrop, A.J. Bush, Solid State Ionics 136e137 (2000) 119.

74. Y.-K. Taninouchi, T. Uda, T. Ichitsubo, Y. Awakura, E. Matsubara, Solid State Ionics 181 (2010) 719.
75. S. Beg, S. Hafeez, N.A.S. Al-Areqi, Phase Trans. 83 (2010) 169.
76. N.A.S. Al-Areqi, S. Beg, Mater. Chem. Phys. 115 (2009) 5.
77. M.V. Morozova, E.S. Buyanova, JuV. Emelyanova, V.M. Zhukovskiy, S.A. Petrova, Solid State Ionics 192 (2011) 153.
78. M. Malys, I. Abrahams, F. Krok, W. Wrobel, J.R. Dygas, Solid State Ionics 179 (2008) 82.
79. S. Beg, S. Hafeez, N.A.S. Al-Areqi, Phys. B 405 (2010) 4370.
80. A. Al-Alas, S. Beg, N.A.S. Al-Areqi, Mater. Chem. Phys. 136 (2012) 15.
81. E. Pernot, M. Anne, M. Bacmann, P. Strobel, J. Fouletier, R.N. Vannier, G. Mairesse, F. Abraham, G. Nowogrocki, Solid State Ionics 70 (1994) 259.

Chapter 3 Materials and techniques

In this chapter the details of samples preparation, their nomenclature and technical details of experimental techniques are given.

3.1 Raw materials

The stoichiometric amounts of V_2O_5 (99%, Loba Chemie), MgO (99%, Loba Chemie), Al_2O_3 (99%, Loba Chemie), TiO_2 (99%, Loba Chemie) and Li_2O (97%, Sigma Aldrich) chemicals were used for preparing all the samples. Steel 430 was used as interconnect material for interaction study with selected samples. These chemicals for sample preparation were used in as received condition.

3.2 Samples preparation

The four series of nominal compositions of $V_{2-x}M_xO_{5-\delta}$ (M=Li, Mg, Al and Ti, where x=0.0-0.30, step size=0.05) were prepared by the melt and quench methods.

Table 3.1 $V_{2-x}M_xO_{5-\delta}$ series along with their labels and chemical compositions.

Sample series	Sample label	Chemical composition
$V_{2-x}Li_xO_{5-\delta}$	VL-0.15	$V_{1.85}Li_{0.15}O_{5-\delta}$
	VL-0.20	$V_{1.80}Li_{0.20}O_{5-\delta}$
	VL-0.25	$V_{1.75}Li_{0.5}O_{5-\delta}$
	VL-0.30	$V_{1.70}Li_{0.30}O_{5-\delta}$
$V_{2-x}Mg_xO_{5-\delta}$	VM-0.05	$V_{1.95}Li_{0.05}O_{5-\delta}$
	VM-0.10	$V_{1.90}Li_{0.10}O_{5-\delta}$
	VM-0.15	$V_{1.85}Li_{0.15}O_{5-\delta}$
	VM-0.20	$V_{1.80}Li_{0.20}O_{5-\delta}$
	VM-0.25	$V_{1.75}Li_{0.25}O_{5-\delta}$
	VM-0.30	$V_{1.70}Li_{0.30}O_{5-\delta}$
$V_{2-x}Al_xO_{5-\delta}$	VA-0.05	$V_{1.95}Al_{0.05}O_{5-\delta}$
	VA-0.10	$V_{1.90}Al_{0.10}O_{5-\delta}$
	VA-0.15	$V_{1.85}Al_{0.15}O_{5-\delta}$
	VA-0.20	$V_{1.80}Al_{0.20}O_{5-\delta}$
$V_{2-x}Ti_xO_{5-\delta}$	VT-0.15	$V_{1.85}Ti_{0.15}O_{5-\delta}$
	VT-0.20	$V_{1.80}Ti_{0.20}O_{5-\delta}$
	VT-0.25	$V_{1.75}Ti_{0.25}O_{5-\delta}$
	VT-0.30	$V_{1.70}Ti_{0.30}O_{5-\delta}$

In addition to these samples, V_2O_5 was also synthesized by similar processing conditions to compare the results with doped samples. The sample compositions of the prepared series and their labels are given in Table 3.1. To obtain homogeneous powder, the stoichiometric amounts of the chemicals were mixed in acetone medium for 2h using an agate mortar pestle followed by melting in recrystallized alumina crucibles at 900 °C using a high resistance electric furnace.

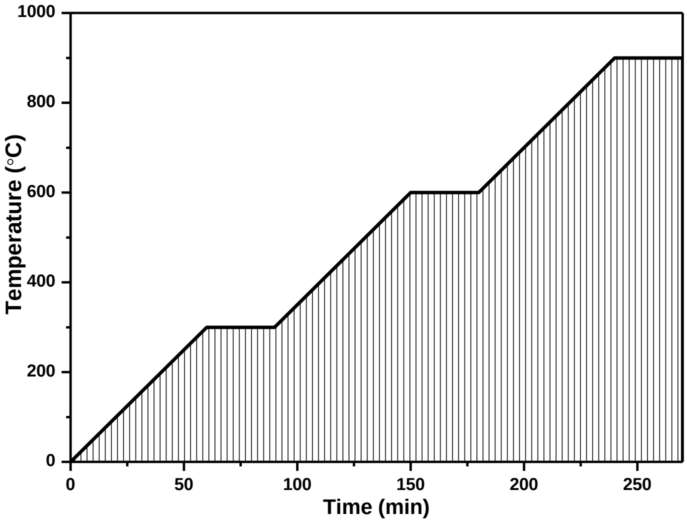

Fig. 3.1 Schedule followed for the melting samples.

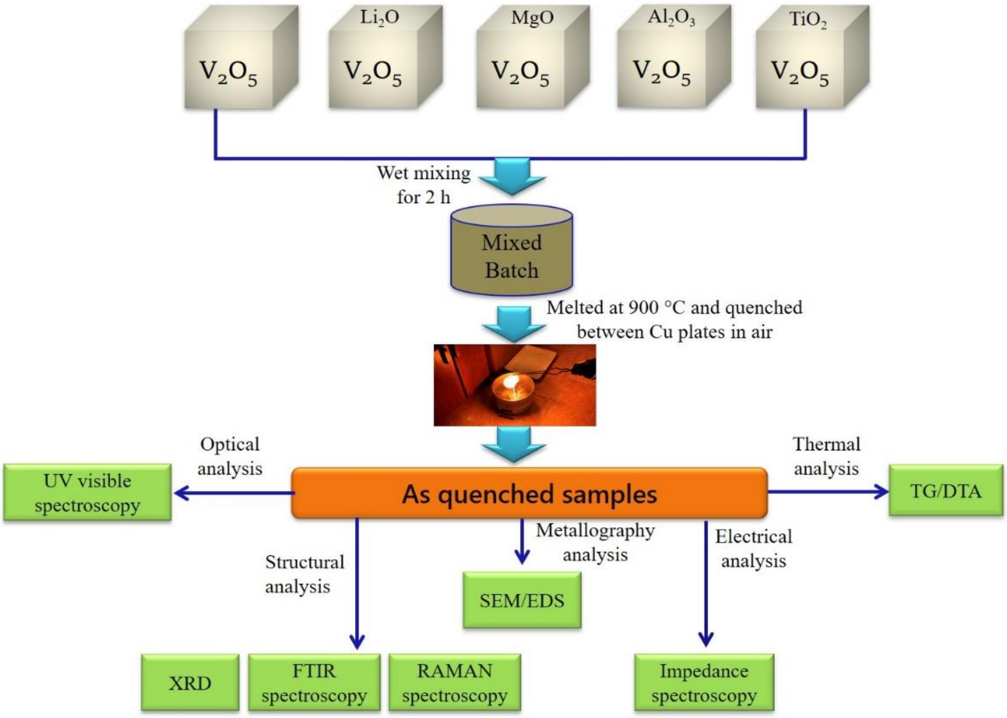

Fig. 3.2 Flow charts that depicting various stages of samples preparation and experimental techniques used for characterization and measurement.

In order to increase the inter diffusion of the initial constituents; the furnace was kept at 300 and 600 °C for 0.5 h. Finally, the melt was kept at 900 °C for 0.5 h to achieve homogeneous melt followed by quenching between two thick copper plates in the air. The graphical representation of melting schedule is shown in Fig. 3.1. The as-quenched samples were ground to form fine powders for various experimental characterizations. The details samples preparation and adopted experimental characterization techniques are shown in a flow chart (Fig. 3.2).

3.3 Preparation of diffusion couples

The pieces of steel 430 as interconnect materials were cut into 9mm × 8mm ×3mm dimensions. After that these pieces were ultrasonically cleaned in acetone medium for 0.5 h. The glass powder was mixed in ethanol and was kept as sandwich between two steel 420 plates for interaction study. These diffusion couples were heat treated in furnace at 620 ºC for different time periods (1, 10 and 100 h). After that the diffusion couples were mechanically polished followed by microstructural and interfacial analysis. The schematic representation for preparation of diffusion couples is shown in Fig. 3.3.

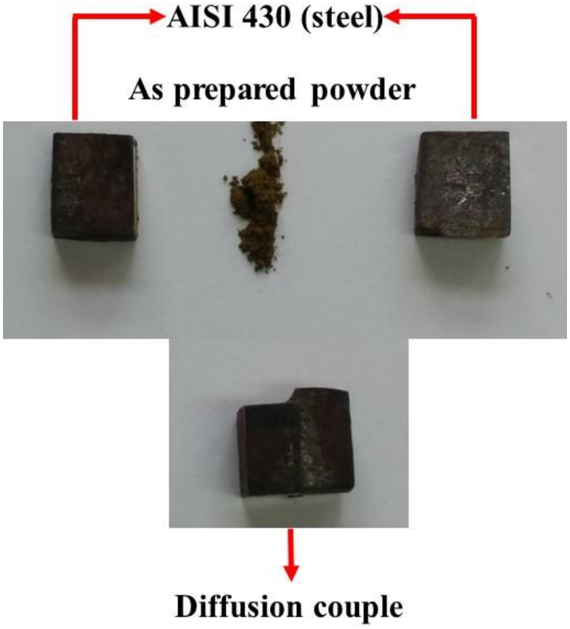

Fig. 3.3 Schematic representation for preparation of diffusion couples for interaction study.

3.4 Characterizations

The as quenched samples were characterized to investigate the nature and crystalline phase formation, structural morphology, optical properties, thermal stability and conductivity behaviour of as prepared samples. The as quenched samples were characterized using X-ray diffraction (XRD), Fourier transform infrared (FTIR) spectroscopy, Raman spectroscopy, UV-visible spectroscopy, differential thermal analysis (DTA) with thermo gravimetric analysis (TGA), impedance spectroscopy, scanning electron microscopy (SEM) with attached energy dispersive spectroscopy (EDS) and X-ray photoelectron spectroscopy (XPS). The technical details and parameters used to characterize the samples of these techniques are given in the following section.

3.4.1 Density measurement

The standard Archimedes principle was used to measure the density of the as quenched samples with Xylene as an immersion liquid ($\rho_{xylene} = 0.863$ gcm^{-3}). The density (ρ) of the prepared samples was calculated by the following equation.

$$\rho = \frac{W_{air}}{(W_{air} - W_{xylene})} \times \rho_{xylene} \tag{3.1}$$

Where, W_{air} and W_{xylene} are the weight of the sample in air and xylene, respectively. The molar volume (V_m) of the as quenched samples was calculated using the following equation.

$$V_m = \sum_i M_i / \rho \tag{3.2}$$

Where, ρ and M_i are the density and molar mass of the samples, respectively. The concentration of dopants ions (N) was also calculated by the following equation.

$$N_i = N_A \times mol\%\ of\ cation \times valency / V_m \tag{3.3}$$

Here, N_A and M are the Avogadro's number and molecular weight, respectively. The average inter-ionic distance (R_i) was also calculated using following equation.

$$R_i = (1/N)^{1/3}. \tag{3.4}$$

The polaron radius (r_p) was calculated by the well-known formula as given below.

$$r_p = (R_i/2) \times (\pi/6)^{1/3} \quad (3.5)$$

3.4.2 Structural analysis

3.4.2.1 X-ray diffraction

The X-ray diffraction is a versatile technique for qualitative and quantitative analysis of the materials. It was used for primary investigation to confirm the nature like amorphous, nanocrystalline and crystalline of as prepared samples as well as heat treated samples. Furthermore, the crystalline phase identification, their volume fractions and crystallite size of the samples were also calculated using X-ray diffraction patterns of the samples. In the present case, PANalytical X'Pert PRO system with Cu- K_α radiations (λ=1.5406Å) with scan rate of 2° min^{-1} in the range of 10-90° diffraction angle is used for X-ray diffraction of the powder samples. For crystalline materials, XRD patterns show sharp peaks at Bragg's angle (2θ) corresponding to the diffraction planes characteristic of the crystal structure of the samples. The inter-planar distance (d) is calculated using Bragg's law. Crystalline phase identification has been done using Xpert pro high-score software. The crystallite size (t) of samples were calculated using Debye Sherrer's formula

$$t = \frac{K\lambda}{\beta cos\theta} \quad (3.6)$$

Where, K is the shape factor (~0.9), λ is the wavelength of the monochromatic x-ray, β is the full width at half maxima (in radians) and θ is the Bragg's diffraction angle.

3.4.2.2 Fourier transform infrared spectroscopy

Fourier transform infrared (FTIR) spectroscopy is a technique in which data acquisition based on the interference patterns produced by the interaction among molecules of samples with infra-red radiations and then collected data is converted into a spectrum. The incident infrared radiations on the sample become partially absorbed and partially transmitted depending upon the nature of the samples. The spectrum obtained in the form of bands corresponding to the molecular vibrations of specific functional group. Hence, we can recognise the types of functional group present in the given materials and their vibrations. It is very informative technique particularly for polymer and glass samples. Since, in case of glasses, various structural units of network formers are usually present with different non-bridging oxygens (NBOs) and bridging oxygens (BOs) in various structural group of glasses. Perkin Elmer-Spectrum-RF-1 FTIR spectrometer is performed to record infrared spectra of the present samples in the range of 400-4000 cm^{-1}. KBr powder is used to make the pellets for FTIR measurements. 5% powder of powder samples was mixed in 95% KBr powder. After proper mixing, powder was pelletized under 5 KN/m^2 pressure.

3.4.2.3 Raman spectroscopy

Raman spectroscopy is used to study vibrational, rotational and low frequency modes in the materials. It is commonly used to observe vibrational modes. The vibrational modes are specific to chemical bonds and symmetry of molecules. Therefore, it gives the fingerprint for the molecules. Raman scattering is the example of inelastic scattering as, during the interaction of photons and molecules, energy transfer between them. In Raman spectroscopy, a laser beam is directed on a sample and then light from the illuminated spot is collected with the help of a lens. The laser light interacts with phonons/other excitations source present in the system, which results energy of the laser photons being changed up or down. The change in molecular polarization potential is essential for the molecules to show a Raman effect. The change in energy provides information about the phonon modes in a material. Due to elastic scattering, the wavelength near to laser light are filtered out whereas the rest of the light is dispersed onto a detector. In present study, the Raman spectra of the prepared samples are carried out in the spectral range of 100-5000 cm^{-1} by Features STR 500 Airix Raman system equipped with Nd-YAG (532 nm) as an excitation source.

3.4.3 Optical analysis

3.4.3.1 UV-Vis spectroscopy

The working principle of UV-Vis spectroscopy is based on the interaction of samples with the electromagnetic radiations in the ultraviolet, visible and near infrared region. The absorption, reflection and transmission of incident UV-Vis radiations on the sample depend on the electronic transitions in the sample. The element/compound absorbs radiations matching to the optical band gap energy of the material and various electronic transition or defect states. In addition, the transmission and reflection spectra give information about the optical properties (% reflection and transmission of visible radiations) of the samples. UV-Visible spectroscopy will provide the fair idea about narrow and wide band gap of materials. In the present study, the powder samples are used to perform UV-Visible spectrophotometer at room temperature in reflectance mode using a double beam Hitachi (3900H) spectrophotometer with spectral range of 200-800 nm. The Kubelka-Munk function ($F(R) = (1 - R)^2/2R$) was used to obtain the optical band gap E_g of the samples. The optical band gap energy was calculated by applying Tauc plots between $(F(R)h\nu)^2$ and photon energy ($h\nu$).

3.4.4 Thermal analysis

3.4.4.1 Differential thermal analysis

Differential Thermal Analyzer (DTA) is an analytical technique. It is used to examine the phase transitions, melting and characteristic temperatures of glasses and polymers. In this technique, thermal characteristics of a sample are measured with reference to standard materials i.e. (Al_2O_3), which results into endothermic and exothermic characteristic peaks. The differential temperature is plotted with respect to the temperature, corresponding to the various events with respect to reference sample. In addition, thermogravimetry (TG) measures the mass change in sample with reference to a standard sample as a function of temperature by a thermo-balance. Thermal gravimetric analysis (TGA) is done to examine the oxidation, reduction and thermal stability of the samples. The TG and DTA of the samples were analysed using Perkin Elmer (model: Diamond Pyris) equipment with a heating rate of 10 ºC from room temperature to 1000 ºC in N_2 atmosphere. All the analysis of the samples has been performed using alumina (Al_2O_3) as a reference sample. The sample quantity was taken from 5 to 10 mg for every TG/DTA measurement.

3.4.5 Microstructural analysis

3.4.5.1 Scanning electron microscopy/energy dispersive spectroscopy (EDS)

The scanning electron microscope is a very useful technique in which morphological features of the samples are studied using high energy electrons beam. In SEM, the electrons are interacted with materials and generate information in the form of signals about topography of the surface of the sample, composition and morphology of the present phases. The different types of signals which are generated by the interaction in SEM include common mode such as secondary electrons (SE), back scattered electrons (BSE), characteristic X-ray and transmitted electrons. To detect these signals, the specialized detectors are required that are positioned at different place in SEM instrument. The X-ray detector was used to analysis the compositions of given sample using EDS. It is involved the addition of an assembly to SEM and is known as EDS. In the present study, SEM of the prepared samples was carried out with the help of scanning electron microscope JEOL/EO (version 1.0). In order to see the interaction between prepared samples and interconnect, SEM along with EPMA/X-ray dot mapping was done. The SEM study was carried out on platinum-sputtered powders/pellets and fractured surface of the samples.

3.4.6 X-ray photoelectron spectroscopy (XPS)

The XPS is a surface sensitive technique to precisely estimate the chemical state of elements. The sample material is irradiated with X-rays (hν) to eject out photoelectrons from the core-levels of the element. The kinetic energy (KE) of the ejected photoelectrons is measured to calculate the binding energy. The binding energy of electrons in the inner shell is a unique feature of an element. Thus, a shift in the binding energy of any element provides information about its chemical state in the material network. However, a shift in peak is also observed due to the sample charging effect. To compensate for this shift, a correction is applied. C1s peak due to the presence of carbon monolayer in vacuum on the surface of the samples has standard binding energy of 284.8eV. Therefore, it is adjusted to this value to correct the BE for other elements. In the present work, XPS was performed on selected samples using an X-ray Photoelectron Spectrometer (model: PHI VersaProbe II with AES). The XPS measurements were carried out with monochromatic AlKα radiation ($h\nu$=1486.60 eV). The purpose of XPS analysis was to understand the effect of dopant on the chemical state of vanadium in the present samples.

3.4.7 Electrical analysis

3.4.7.1 Impedance spectroscopy

Impedance spectroscopy is a versatile technique to examine the frequency and temperature dependent electrical properties of the ceramic materials. In this technique, the sample in the form of disk mounted between the two electrodes which act as a RC circuit. The resistive-capacitive measurement provides the result in the form of real and imaginary impedance and permittivity. Thus, to understand the transport properties of the materials, the AC conductivity is obtained with respect to frequency and temperature. In the present study, the samples are polished with fine emery papers and then coated with Platinum on both sides using 3000-FC auto fine coater from JEOL. It has been done to form a parallel plate capacitor with prepared samples as dielectric medium. The electrical properties of the samples are examined by impedance analyser from SOLARTRON (SI-1260). The frequency and temperature dependent conductivity is studied in the frequency range from 100Hz-1MHz at temperatures range of 25-400°C.

Chapter 4 Results and discussion

This chapter contains four series of samples i.e. $V_{2-x}M_xO_{5-\delta}$, where M=Li, Mg, Al and Ti and $0.0 \leq x \leq 0.30$). All the samples were synthesized by melt and quench technique. These as prepared samples were characterized using various experimental techniques. The results are discussed in light of chemical nature of dopants, their concentration, creation of oxygen vacancies and defects, change in crystal structure and mechanism of conductions. In last, the selected samples were used to carry out the interaction study with steel 430 interconnect material for different time duration at 620 ˚C.

4.1 Lithium doped V_2O_5 ($V_{2-x}Li_xO_{5-\delta}$; $0.15 \leq x \leq 0.30$)

4.1.1 Physical properties

Various physical parameters such as apparent density, molar volume and ionic concentration and their inter-ionic distance and polaron radius are calculated for the as-quenched samples and given in Table 4.1.

Table 4.1. Various physical parameters calculated using apparent density with their labels of the as quenched samples.

Sample ID	M (gmol^{-1})	ρ (gcm^{-3})	V_m (cm^{3}mol^{-1})	N_i ($\times10^{23}$cm^{-3})	R_i (Å)	r_p (Å)
VL-0.15	170.48	3.09	55.17	1.63	1.82	0.73
VL-0.20	166.68	3.00	55.56	2.16	1.66	0.67
VL-0.25	162.88	2.93	55.59	2.70	1.54	0.62
VL-0.30	159.08	2.86	55.62	3.24	1.45	0.58

Fig. 4.1 shows the variation of density (ρ) and molar volume (V_m) with Li_2O dopant concentration of as-quenched samples. It is observed (Fig. 4.1) that the density decreases while molar volume increases with increasing Li_2O content. This decrement in the density is due to the replacement of the heavier density of V_2O_5 (3.36 gcm^{-3}) by the lighter density of Li_2O (2.01 gcm^{-3}) [1, 2]. On the other hand, the doping of Li^{1+} into V^{5+} also creates oxygen vacancies in

the system. The size of oxygen vacancy is smaller as compared to the size of the oxygen anion O^{2-}. So, the volume of the samples with dopant also decreases which leads to increase in the density. However, a lower density of dopant Li_2O as compared to parent V_2O_5 influences the density of samples more efficiently than decrease the volume due to creation of vacancies and ionicity in the samples [3].

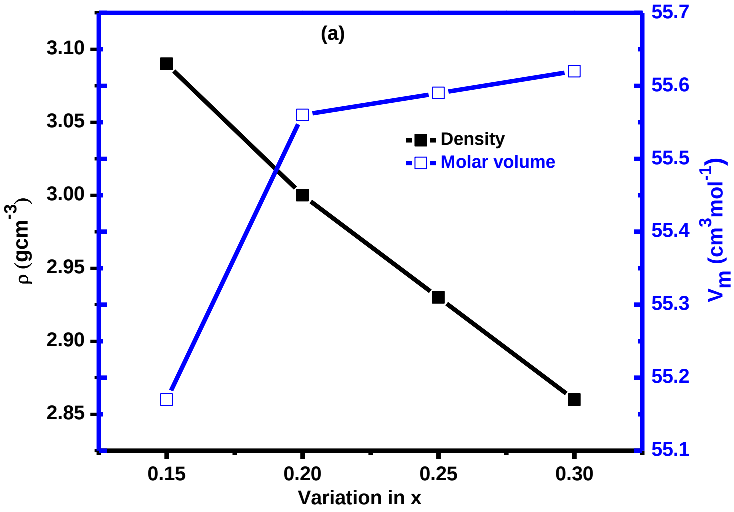

Fig. 4.1. Change in density and molecular volume of $V_{2-x}Li_xO_{5-\delta}$.

Hence, the density of samples decreases with the addition of dopant (Li_2O) in place of vanadium. On the other hand, the increase in molar volume is ascribed to the rearrangement of the lattice which leads to creating oxygen vacancies due to $VO_5 \rightarrow VO_4$ conversion and the substitution of Li^{1+} for V^{5+} (as discussed in FTIR and TGA section) [2].

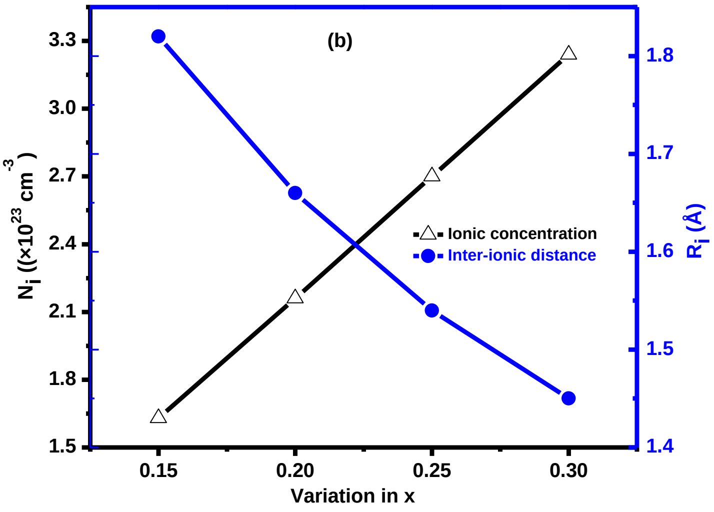

Fig. 4.2. Change in ionic concentration and interionic distance of $V_{2-x}Li_xO_{5-\delta}$.

The increment in molar volume supports that the Li^{1+} enters the network and occupy the interstitial space, which leads to an increase in overall free volume of doped V_2O_5. Fig. 4.2 shows the change in ionic concentration (N_i) and their inter-ionic distance (R_i) with lithium concentration on the cost of vanadium for all the samples. The ionic concentration increases whereas inter-ionic distance decreases (1.8-1.4 Ǻ) with increasing Li_2O content. Decrement in the inter-ionic distance might be increased the localization effect as also confirmed by the polarization radius values (Table 4.1). Usually, the decrease in molar volume is responsible for the decrease in inter-ionic distance [2]. The polaron radius (r_p) values are also calculated using R_i (Table 4.1). These polaron radius values decrease from 0.7 to 0.5 Ǻ (Table 4.1) with Li^{1+} dopant due to increases R_i. The magnitude of polaron radius values suggested that they are highly localized and this localization effect increases with dopant (Li^{1+}) concentration and it could also affect the other properties like electrical properties of doped V_2O_5 system.

4.1.2 X-ray diffraction (XRD) analysis

Fig. 4.3 represents the XRD patterns of the Li_2O modified V_2O_5 as-quenched samples.

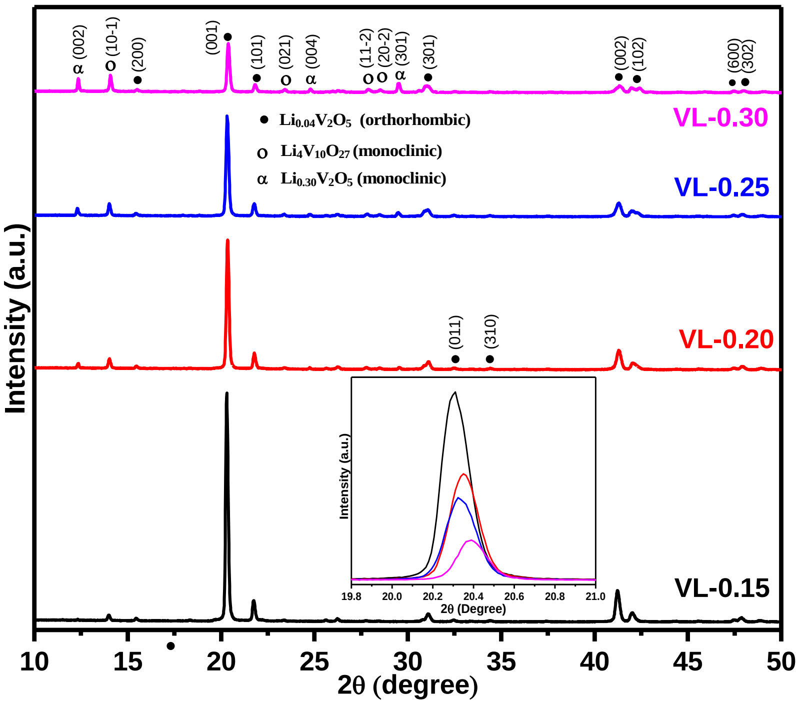

Fig. 4.3. XRD patterns of Li_2O doped V_2O_5 as quenched samples. Inset shows highest intense peak shifting towards higher diffraction angle.

The as-quenched samples exhibit three crystalline phases i.e. major orthorhombic $Li_{0.04}V_2O_5$ (ICDD: 01-085-0608), minor monoclinic $Li_4V_{10}O_{27}$ (ICDD: 00-046-0187) and minor monoclinic $Li_{0.30}V_2O_5$ (ICDD: 00-018-0755), respectively. The diffraction peak (001) at 20.3° corresponds to $Li_{0.04}V_2O_5$ major phase, which shows higher diffraction angle shift with Li_2O content as shown in the inset of Fig. 4.3. The shifting of peak towards higher diffraction angle side is the evidence of lattice contractions [4]. This is due to the smaller cationic radius Li^{1+} (0.167 nm) in comparison to V^{5+} (0.171 nm). As a result of the substitution of the larger cationic radius of V by the smaller cationic radius of Li, the lattice compression (compressive strain) arises in the $Li_{0.04}V_2O_5$ crystalline phase [4]. Further comparing the peak intensities of the phases, it is observed that the intensity of the major phase ($Li_{0.04}V_2O_5$) at 20.3° decreases whereas the intensity of the two other phases i.e. ($Li_{0.30}V_2O_5$ and $Li_4V_{10}O_{27}$) at 12.3° and 14.0° increases caused by doping of Li_2O into the V_2O_5 lattice. The relative volume fraction of different phases is calculated using direct comparison method. So, the higher concentration of Li_2O increases the volume fraction of minor phases i.e. $Li_{0.30}V_2O_5$ and $Li_4V_{10}O_{27}$ phases as given in Table 4.2. So, the volume fraction of less symmetric phases (monoclinic) increases as dopant concentration increases.

Table 4.2. Optical, conductivity parameters and volume fractions of different crystalline phases of the as quenched samples.

Sample ID	E_g (eV)	E_u (eV)	σ_{ac} at 450 °C and 10^7 Hz ($10^2\times Sm^{-1}$)	σ_{dc} at 450 °C ($10^2\times Sm^{-1}$)	E_a (eV) between 50-250 °C	Present phases	Volume fraction (%)
VL-0.15	2.22	0.31	0.11	0.08	0.26	$Li_{0.04}V_2O_5$	95.35
						$Li_4V_{10}O_{27}$	3.05
						$Li_{0.30}V_2O_5$	1.58
VL-0.20	2.16	0.37	0.17	0.09	0.21	,,	86.45
						,,	8.30
						,,	5.10
VL-0.25	2.14	0.40	0.21	0.11	0.31	,,	80.74
						,,	11.97
						,,	7.27
VL-0.30	2.08	0.41	0.29	0.12	0.43	,,	60.26
						,,	20.70
						,,	18.00

4.1.3 FTIR spectroscopy analysis

Fig. 4.4 shows infrared (IR) spectra at room temperature to investigate the structural changes with increasing concentration of Li_2O dopant. The IR spectra exhibited prominent absorption bands at 1022, 1000, 957, 916, 819, 753, 602 and 488 cm^{-1}. The absorption bands at 1022 and 1000 cm^{-1} are ascribed to the vibrations of isolated V=O vanadyl groups in VO_5 trigonal bipyramids [5-7]. These characteristics stretching bands are associated with the layer structure of the V_2O_5 in present samples, is [5-8].

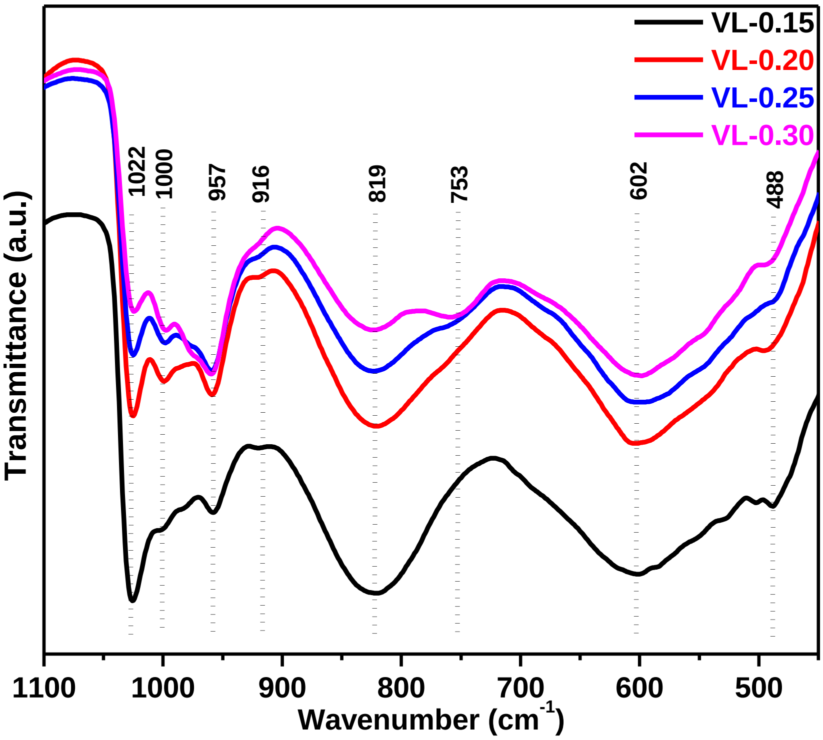

Fig. 4.4. FTIR spectra of $V_{2-x}Li_xO_{5-\delta}$ ($0.15 \leq x \leq 0.30$) as quenched samples.

The broadness of 1022 cm^{-1} band decreases with increasing Li_2O content due to the decrease in the number of ionic groups and V=O bonds. Additionally, this band has a small shift to the lower wavenumber, which suggests the reduction of vanadium (V^{5+} to V^{4+}/ V^{3+}) due to the addition of lithium content [9]. The V-O bond length increases due to the larger size of V^{4+} (0.67 Å) than V^{5+} (0.60 Å), results in requiring lower energy for the lattice vibration. [10]. The high-temperature melt quenching of the present samples could be responsible for the reduction of vanadium due to scarcity of oxygen in the furnace at high temperature [9]. The band at 957

cm^{-1} assigned to the symmetric and anti-symmetric stretching vibration of the isolated VO_2 groups in the VO_4 polyhedra [5, 11]. A small kink at 916 cm^{-1} has appeared with the addition of Li_2O content. It is also assigned to the asymmetric stretching vibrations of the isolated VO_2 groups in VO_4 polyhedra [5, 9]. Another band at about 819 cm^{-1} is attributed to the vibrations of isolated [VO_4] tetrahedral. The broadness of this band decreases with Li_2O content and splits into two bands (819 and 753 cm^{-1}) at maximum Li_2O content sample (VL-0.30). This new generated band is assigned to V-O-V stretching [1, 5, 11]. The broadening of the bands is directly related to the existence of different structural units of the same element with variable oxygens [1]. Thus, in the present case, the different structural units of vanadium decrease with the addition of Li_2O content. The band at 602 cm^{-1} is ascribed to the bending vibrations of V-O-V units. The band at 488 cm^{-1} could be assigned to the bending modes of the V_2O_5 network consisting of [VO_5] polyhedral and a characteristic vibration of Li^+ cations [5, 8, 12]. This band shows a small shift to the higher wavenumber with the highest doping of Li_2O (VL-0.30 sample), which shows that some portion of V^{3+}/V^{4+} oxidized to V^{5+}. The bond length between vanadium and oxygen decreases due to the smaller size of V^{5+} as compared to V^{4+}/V^{3+}, which leads to strengthening of this vibration [1, 10, 13]. According to Dimitriv *et* al. [11], the vanadates can exist in the form of layers and chains and smaller complexes, which depends on the ratio of V_2O_5 and Li_2O in the samples. The Li^{1+} ions can be situated between the vanadate chains, whereas some Li^{1+} ion can be form independent polyhedra (LiO_n), which can be located in the chains themselves [11]. This assumption suggests two different forms of Li ions distribution in the V-O polyhedra (interstitial sites or substitutional sites) as shown in Fig. 4.5 (a) & (b). In interstitial condition, the Li ions can be located between vanadate chains and layers. Li ions can interact with the isolated V=O bonds, which leads to the longer bond length (Fig. 4.5 (a)). In substitutional condition, Li ions can occupy positions in the vanadate chain, which leads to break the some of the weaker V-O-V bonds and form new V-O-Li bridges (Fig.

4.5 (b)) [11]. Also, there is a possibility to take place a redox reaction ($2V^{5+} + O^{2-} \rightarrow 2V^{4+} + O_2 \uparrow$) during the melting of the batches at 900 °C. The V^{5+} ions take a part as a network forming positions with VO_5 structural units which can be formed V-O-Li linkages [9]. Therefore, the influence of Li ions on the V=O bond is restricted and have an indirect manifestation which leads to preserve this band at ~1022 cm^{-1} [11]. Thus, the V=O band is partially affected by Li_2O doping in the present samples.

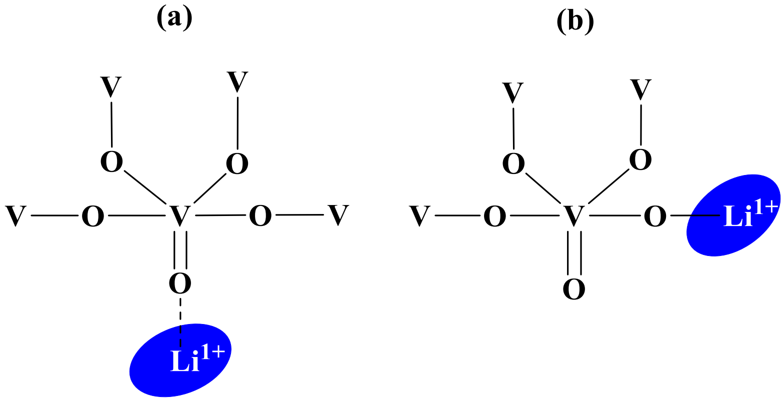

Fig. 4.5. Proposed mechanism of possible positions of the Li^{1+-} ions into vanadium oxygen polyhedra: (a) interstitial sites; (b) substitutional sites.

4.1.4 Raman spectroscopy analysis

Raman spectra of as-quenched samples are shown in Fig. 4.6. Raman bands around 139, 191, 279, 400, 484, 516, 689 and 988 cm^{-1} are observed. The sharp Raman band at 988 cm^{-1} is attributed to the symmetric stretching of V=O groups in undoped V_2O_5 [14, 15]. The intensity of this sharp V=O band increases with lithium content, establishes the formation of multilayer structures of V_2O_5 [8]. The other Raman bands around 400 and 516 cm^{-1} are attributed to the existence of the characteristic layer structure of crystalline V_2O_5. Besides these, a small shoulder at 484 cm^{-1} is also observed, which can be due to the symmetric stretching of the V-O-V bonds in V_2O_5 [14, 15]. The band at 400 cm^{-1} could be related to the Li-O stretching. Another band at 279 cm^{-1} is assigned to the deformational mode of the surface vanadyl groups. The other band around 689 cm^{-1} is due to the stretching vibration of oxygen ion in bridging position between three vanadia centres [14, 15]. Finally, Raman band at 191 and 139 cm^{-1} are associated to the [VO_5]-[VO_5] vibrations and strongly accompanying with the layered structure. They are observed at low wavenumbers due to the heavy [VO_5] units [16]. Presence of all these vibrations (Fig. 4.4, 4.5 and 4.6) substantiate the structural changes and formation of multiphase lithium vanadate in the as-quenched samples as discussed in X-ray diffraction and FTIR analysis sections.

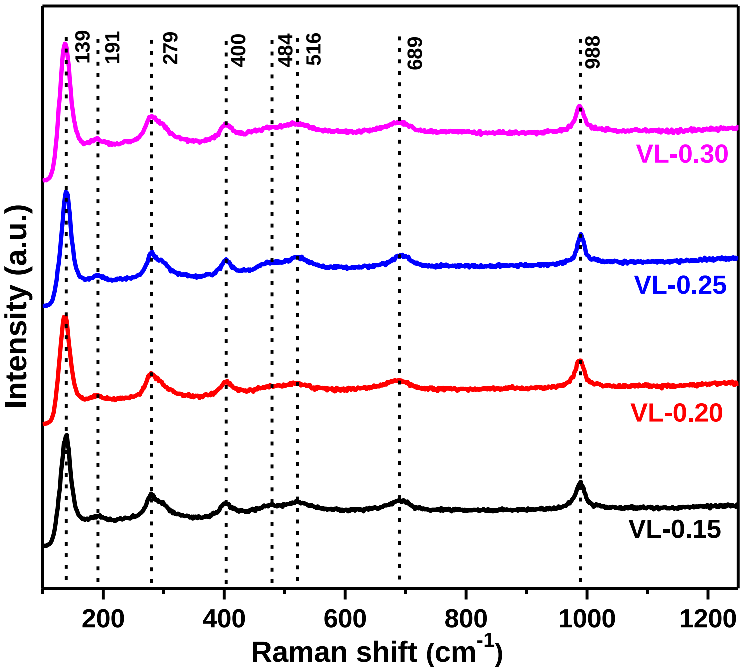

Fig. 4.6. Raman spectra of Li_2O doped vanadium pentoxide as quenched samples.

4.1.5 UV-visible spectroscopy analysis

Fig. 4.7 (a) represents the UV-visible diffused reflectance spectra (DRS) as a function of wavelength for all the samples. The reflectance for VL-0.15, VL-0.20, VL0.25 and VL-0.30 samples are 18.5%, 17%, 15.6% and 13.2%, respectively. The quenched reflectivity could be ascribed to the optical phonon confinement, which leads to the light trapping in the samples [17]. This decrement in reflectivity with increasing Li^{1+} dopant into V_2O_5 lattice can be due to the reflectance onset/absorption edge towards longer wavelengths (red shift). It is good agreement with reported literature [17, 18]. This reflectance data is used to calculate the optical band gap by Kubelka-Munk function [34].

$$F(R) = K/S = (1-R)^2/2R \tag{4.1}$$

Where, $F(R)$, K and S are the Kubelka-Munk function, absorption coefficient and scattering coefficient, respectively. The optical band gap is obtained from DRS using following equation.

$$(F(R)h\nu) = k(h\nu - E_g)^n \tag{4.2}$$

Where, k, E_g and $h\nu$ are the proportionality constant, optical band gap and incident photon energy, respectively. The exponent 'n' depends on the transition, where n=1/2, 2, 3/2 and 3 for allowed direct, allowed indirect, forbidden direct and forbidden indirect transition, respectively [19].

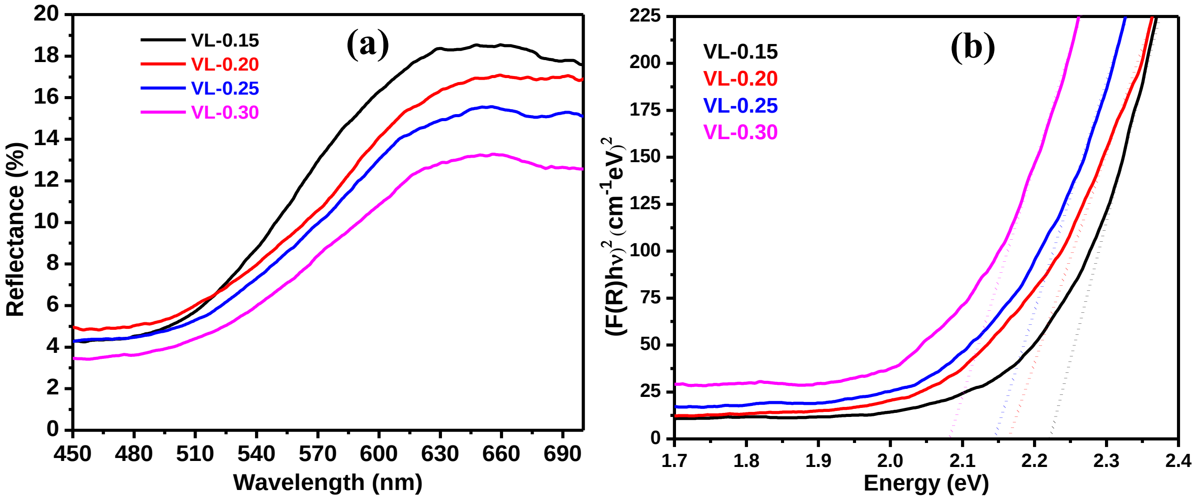

Fig. 4.7. (a) UV-vis spectra and (b) Tauc plots for $V_{2-x}Li_xO_{5-\delta}$ (0.15≤x≤0.30) samples.

The direct optical band gap of all the samples is obtained using the Tauc plot (Fig. 4.7(b)) by extrapolating the straight-line portion of the plots of $(F(R)h\nu)^2$ versus $h\nu$ to energy axis (x-axis) at y=0. The Urbach energy (E_U) of the samples is also calculated using the equation $\alpha(\nu) = \beta\exp(h\nu/E_U)$. The inverse of the slope of the linear portion from $lnF(R)$ versus $h\nu$ is used to measure the Urbach energy of the samples. The optical band gap decreases with increasing content of Li_2O into V_2O_5 for all the samples. The optical band gaps of the present samples are in the semiconductor range (2.22-2.08 eV) and comparable to earlier reported values by another research group [20]. The sample with the lowest concentration of Li_2O (VL-0.15) shows the highest optical band gap (2.22 eV) while the sample with the highest concentration of Li_2O (VL-0.30) shows the lowest optical band gap (2.08 eV). It indicates that the Li_2O concentration increases the defects and impurity bands between valence and conduction band of V_2O_5. The probable existence of variable oxidation states of vanadium as indicated by FTIR, Raman spectroscopy and TG analysis (as discussed in next section) can be responsible for the creation of defects and oxygen vacancies in the present samples. In addition, there is a possibility to create new energy level above the valence band due to doping of Li_2O. So, the filled valence band electrons easily excited to new generated energy level by dopant led to decrease the optical band gap of the samples [21]. The Urbach energy (E_U) of the samples increases with increasing Li_2O content (Table 4.2). VL-0.30 sample shows the highest E_U with the lowest optical band gap signifying the presence of higher disorder as compared to other samples [19]. The optical band gap and Urbach energy both are following opposite trend to each other. It indicates that defects increase with an increase in the doping of Li_2O in place of V_2O_5.

4.1.6 Thermal properties

Fig. 4.8 (a) represents the DTA curves of Li_2O-doped V_2O_5 as-quenched samples in the temperature range of 30-800 °C. In DTA curves, all the samples exhibit three distinct endothermic peaks at a higher temperature (≥571 °C), which result from the melting points (Tm_1, Tm_2 and Tm_3) of three different phases i.e. orthorhombic $Li_{0.04}V_2O_5$, monoclinic $Li_4V_{10}O_{27}$ and monoclinic $Li_{0.30}V_2O_5$, respectively as also observed in XRD patterns of these samples (4.1.2). Fig. 4.8 (b) shows the TG curves of the lithium doped V_2O_5 as-quenched samples, which exhibit typical weight loss behavior. TGA thermograph shows a total weight loss of ~5% in the temperature range of 30-800 °C. The weight loss can be considered in three steps as marked I (30-120 °C), II (120-600 °C) and III (600-700 °C) in the TGA graph. The I step is assigned to the evaporation of adsorbed species and loss of water molecules [19]. The II step could be associated to the reduction of V^{5+} to V^{4+}/ V^{3+} ions as given in the following equation [9, 19].

$$2V^{5+} + O^{2-} \rightarrow 2V^{4+} + O_2 \uparrow \qquad (4.3)$$

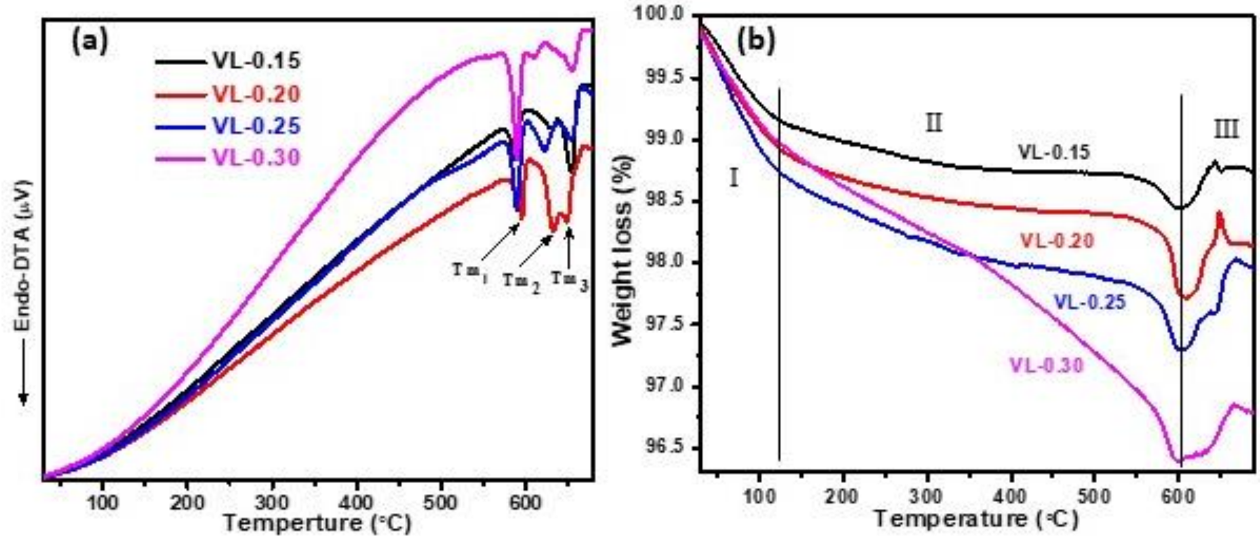

Fig. 4.8 (a) DTA thermographs; and (b) thermal stability nature of Li_2O modified V_2O_5 systems measured at 10 °C heating rate.

In the III step, a little weight gain is observed in all the samples which might be related to the oxidation of V^{3+} to V^{5+} as written by the following equation [22, 23].

$$V_2O_3 + O_2 = V_2O_5 \qquad (4.4)$$

This weight gain during the oxidation at the higher temperature can be associated with the combination of O_2 and its vacancies in the present samples. The reduction of these systems is expected due to vanadium is believed to have a mixed valence state (V^{3+}, V^{4+} and V^{5+}) [9, 22, 23]. It is also observed that weight loss increases with the addition of Li_2O on the cost of V_2O_5 which leads to a decrease in the thermal stability of the present samples (I and II steps). It is manifestation of waterphilic nature of the samples and it increases with an increase in dopant (Li_2O) concentration. The reduction of vanadium from V^{5+} state to lower valance state is also increases with the addition of Li_2O content. The chemical stability also decreases with Li_2O concentration which is also manifested by Urbach energy and FTIR analysis of the samples. All the samples exhibit good thermal and chemical stability in the temperature range of ~300-550 °C without any phase transition as observed in Fig. 4.8 (a) & (b) except VL-0.30 sample. However, sample with the lowest content of Li_2O (7.5 mol%, VL0-.15) shows the highest thermal and chemical stability in the temperature range of ~300-550 ^{o}C in comparison to other samples. Therefore, these samples can be used as electrolytes for solid oxide fuel cells or batteries applications.

4.1.7 Conducting studies

It is a well-known fact that hopping mechanism is responsible for the electrical conduction in these types of materials [1, 24]. The frequency dependent conductivity, σ_{ac} of the samples is determined using the following relation [1, 24].

$$\sigma_{ac}(\omega) = \varepsilon_0 \omega \varepsilon'' = 2\pi f \varepsilon' tan\delta \tag{4.5}$$

Where, ε_0 ε', ε'', f and $tan\delta$ are the permittivity of free space (8.854×10^{-12} Fm^{-1}), dielectric constant, dielectric loss, frequency (in Hz) of the applied electric field and tangent of loss, respectively. Fig. 4.9 (a)-(d) illustrates the AC conductivity (σ_{ac}) variation with frequency and temperatures (50-450 °C, step size of 50 °C).

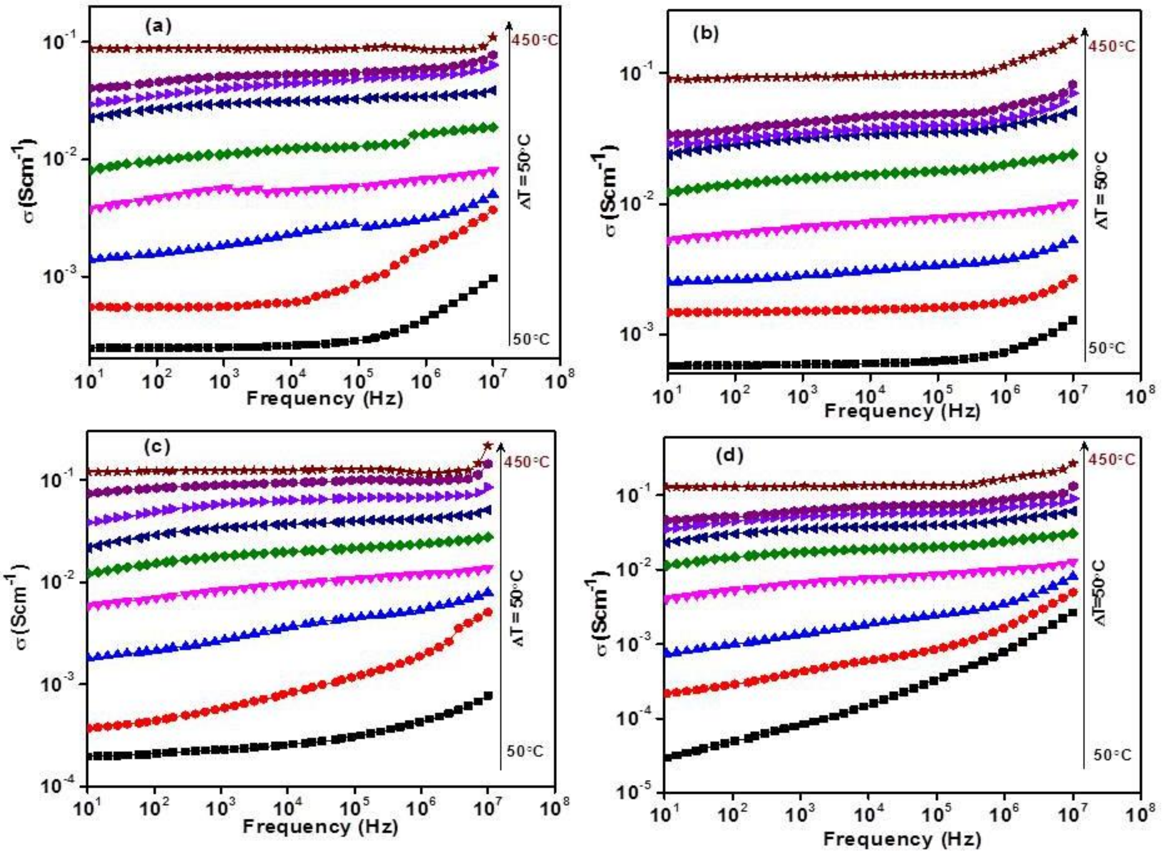

Fig. 4.9 Change in conductivity as a function of frequency and temperatures for (a) VL-0.15 (b) VL-0.20 (c) VL-0.25 (d) VL-0.30 samples

The conductivity is almost frequency independent at low frequency region (plateau region) and corresponds to the DC conductivity (σ_{dc}) as also reported by Thakur *et al.* [25]. At the same time, the conductivity is dependent on frequency (σ_{ac}) at higher frequency region (dispersion region) and increases with increasing frequency [1, 24-26]. The plateau region signifies the randomness of ionic diffusion which is due to the long-range order transport and appreciable diffusion of mobile ions in response to the applied ac field while the dispersion region signifies the conductivity relaxation phenomena in these types of samples [1, 25-28]. It is also observed that σ_{ac} increases with increasing temperature (50-450 ^{o}C) for all the samples which supports the semiconductor nature of the samples [1, 29]. Generally, the conductivity in such type of materials depends on the concentration and mobility of mobile ions/charge carriers i.e. electrons and holes [1, 29]. The mobility of mobile ions/charge carriers increases with increasing temperature which leads to increasing overall conductivity as observed in the present samples. It can be understood by the fact that thermal energy (temperature) excites more electrons from valence band to conduction band resulting in higher conductivity. Further, according to the Jonscher's universal power law, σ_{ac} can be written as [30, 31]:

$$\sigma_{ac}(\omega, T) = \sigma_{dc}(T) + A\omega^{s} \tag{4.6}$$

Where, A is the temperature dependent constant of the material, ω is the angular frequency and s is the frequency and temperature dependent exponent that lies between 0-1. DC conductivity ($\sigma_{dc}(T)$) is calculated to extrapolate AC conductivity at the lowest frequency (Fig. 4.9) and given in Table 4.2. The activation energy (E_a) of the conduction is calculated using the Arrhenius plot (Fig. 4.10 (a)) between $\ln \sigma_{dc}$ and reciprocal of temperature (1000/T) by the following equation.

$$\sigma_{dc} = \sigma_{o} \exp\left(-E_a/k_B T\right) \tag{4.7}$$

Where, σ_o and k_B are the pre-exponential factor, and Boltzmann's constant, respectively. The values of σ_{ac} and σ_{dc} show an increasing trend with an increase in lithium content as shown in Fig. 4.10 (b).

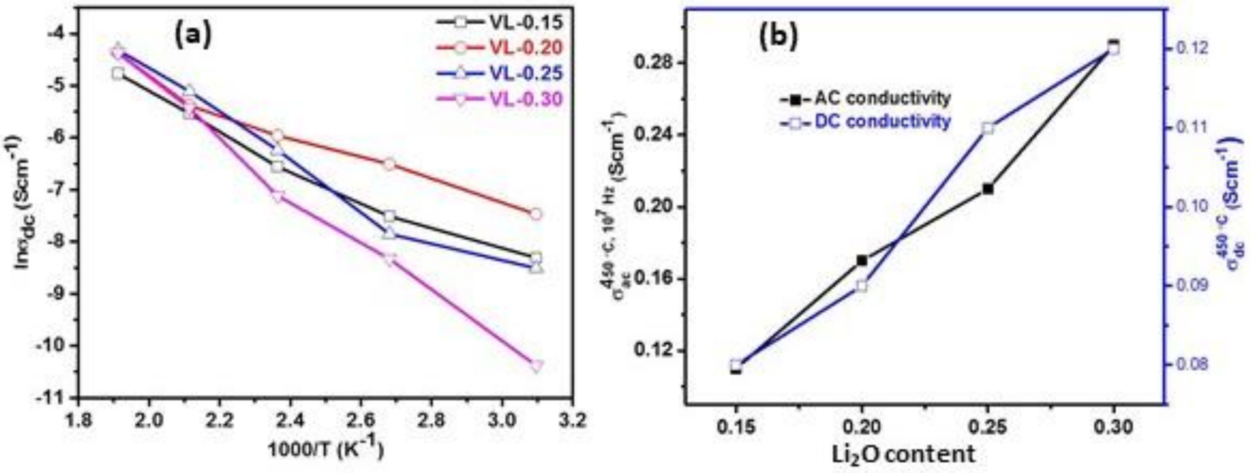

Fig. 4.10 (a) Change in dc conductivity as a function of the reciprocal temperature (b) Change in AC and DC conductivity with Li_2O content in V_2O_5 for VL-0.15 to VL-0.30 samples.

AC conductivity lies in the range of $0.11\text{-}0.29\times10^{2}$ Sm^{-1} at 450 ^{o}C and 10^{7} Hz whereas DC conductivity lies in the range of $0.08\text{-}0.12\times10^{2}$ Sm^{-1} at 450 ^{o}C. In vanadate materials, conductivity depends on the small polarons hopping (SPH) between V^{4+} site to the neighbouring V^{5+} site [1, 27, 24], SPH directly affects by the mobility and number of mobile charge carriers. On the replacement of V^{5+} by Li^{+}, structure of the systems becomes more open due to transition from VO_4 tetrahedral to VO_5 trigonal bipyramid as discussed in section of physical parameters and structural properties sections. This structural change is responsible for a significant increase in oxygen vacancies with an increase in hopping of ions which leads to an increase in conductivity [29, 32-33]. In addition, decrement in density, inter-ionic distance, polaron radius and optical band gap of the samples also support this increasing trend of conductivity with the addition of Li_2O on the cost of V_2O_5 [27]. The calculated activation energy values of DC conduction are depicted in Table 4.2. The activation energy increases with increasing content of Li_2O except VL-0.20 sample and lies in the range of 0.26-0.43 eV (Table 4.2). These activation energy values clearly suggest that the ionic conduction increases with Li_2O concentration into V_2O_5 in the present samples.

4.2 Magnesium doped V_2O_5 ($V_{2-x}Mg_xO_{5-\delta}$; $0.05 \leq x \leq 0.30$)

4.2.1 Physical properties

The measured density (ρ) and evaluated molar volume (V_m) of the as-quenched samples with MgO content are shown in Fig. 4.11.

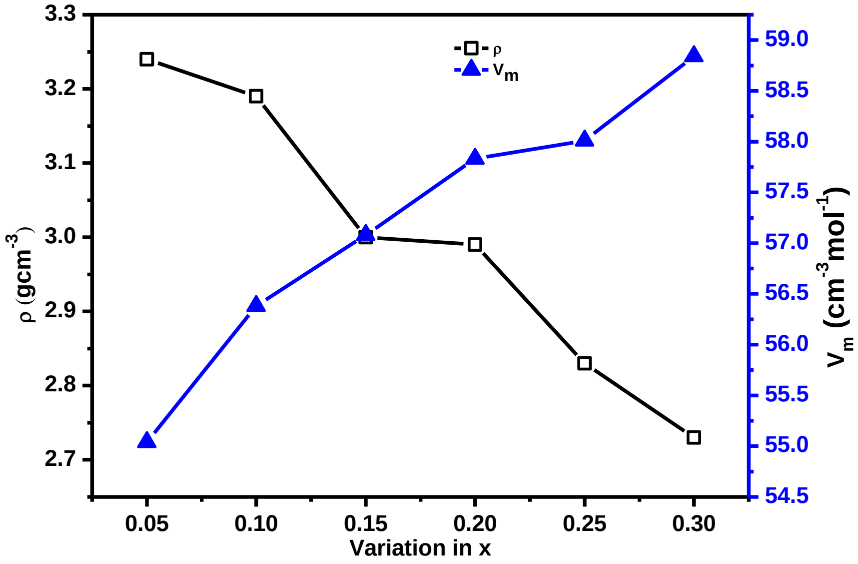

Fig. 4.11 Change in density and molar volume of $V_{2-x}Mg_xO_{5-\delta}$.

It is observed that the density of the as-quenched samples decreases with the increase in MgO at the cost of V_2O_5. Basically, the change in density is related to the change in mass and volume of the sample. Since the difference between the mass of V (181.88 gmol^{-1}) and Mg (40.30 gmol^{-1}) is higher than the difference between the volume of V (179.54 Å^3) and Mg (74.72 Å^3). So, the density of the as-quenched samples decreases with the addition of MgO as also reported for other melt and quench samples [34]. The molar volume of all the as-quenched samples increases with increasing MgO content, due to the creation of non-bridging oxygens (NBOs) and lower cross-linking, which breaks the bonds and increase space in the glass network as also reported by other researchers [12]. It is observed that the ionic concentration increases with the addition of MgO content, while the inter-ionic distance decreases (Table 4.3). This is obvious as the ionic characteristic of MgO is higher than V_2O_5. Moreover, MgO modifies the glass network and increases the ionicity with increasing NBOs in the systems [35].

Table 4.3 Physical parameters of the as prepared samples

Sample ID	ρ (gcm^{-3})	V_m (cm^{3}mol^{-1})	N ($\times10^{23}$ cm^{-3})	R (nm)
VM-0.05	3.24	55.04	0.54	0.26
VM-0.10	3.19	56.38	1.06	0.21
VM-0.15	3.00	57.08	1.58	0.18
VM-0.20	2.99	57.83	2.08	0.16
VM-0.25	2.83	58.01	2.59	0.15
VM-0.30	2.73	58.84	3.07	0.14

4.2.2 X-ray diffraction (XRD) analysis

The XRD patterns of the as-quenched samples are depicted in Fig. 4.12. It is observed that VM-0.05, VM-0.10, and VM-0.15 are crystalline as confirmed by the presence of sharp diffraction peaks in the XRD patterns. While the XRD patterns of x=0.20-0.30 (VM-0.20, VM-0.25, and VM-0.30) show glassy nature with a broad halo between ~20-30°.

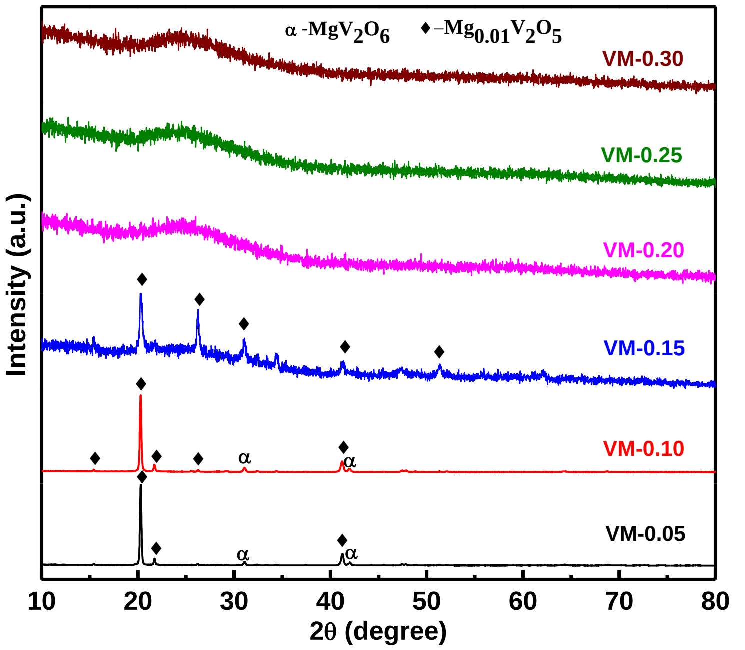

Fig. 4.12 XRD patterns of $V_{2-x}Mg_xO_{5-\delta}$ ($0.15\leq x\leq0.30$) as quenched samples.

The absence of any sharp peak indicates that MgO has entirely entered in the V_2O_5 and disrupts the long-range translational order of V_2O_5 crystalline units. The XRD peaks of VM-0.05, VM-0.10, and VM-0.15 are indexed with $Mg_{0.01}V_2O_5$ (ICDD-01-089-0610) and MgV_2O_6 (ICDD-00-034-0013). The volume fraction of $Mg_{0.01}V_2O_5$ phase increases with MgO content, and VM-0.15 sample becomes monophasic ($Mg_{0.01}V_2O_5$) in nature. Moreover, the diffraction peaks become broader with the addition of MgO content, which indicates that the addition of MgO in V_2O_5 increases the glass formation tendency in the present samples. The MgO-V_2O_5 phase diagram shows the eutectic point around 25 mol% MgO at 604 °C [36]. It is reconfirmed that the higher MgO content has a better probability for forming the glasses with conditional glass former (V_2O_5).

4.2.3 FTIR spectroscopy analysis

IR spectroscopy gives valuable information about molecular vibration/rotation about to the materials bonds. The IR spectra are associated with the change in the dipole moment of the molecule in any materials. It is reported that vanadate group plays a dominant role in the IR spectra. The FTIR spectra of all the samples are represented in Fig. 4.13.

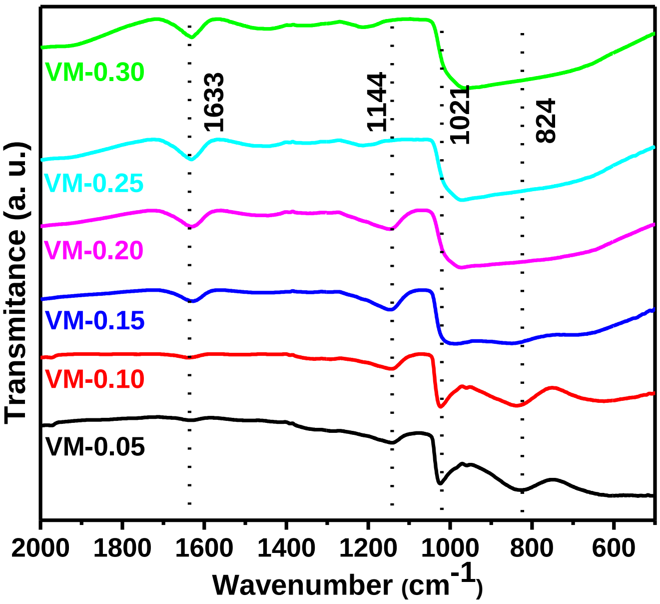

Fig. 4.13 FTIR spectra of $V_{2-x}Mg_xO_{5-\delta}$ ($0.15 \leq x \leq 0.30$) as quenched samples.

These samples show IR absorption band at ~824, ~1021, ~1144, and ~1633 cm^{-1}. There are some changes in band position and intensity with respect to each other as the MgO is introduced. The intensity of the band at ~824 cm^{-1} decreases with increasing concentration of MgO. This band disappears when the system changes from crystalline to amorphous nature with the increasing MgO content. This band is assigned to the stretching modes of V-O-V chains [37]. The band at ~1021 cm^{-1} is associated with the isolated V=O vanadyl groups in VO_5

trigonal bi-pyramids and becomes broader with MgO content [38, 39]. It can be due to the conversion of VO_5 trigonal to VO_4 or VO_2 structural units. It is well reported in the literature that broader band is associated with the presence of multiple structural units of the same element with variable oxygen. It is observed that the IR band at ~1021 cm^{-1} is shifted to a lower wave number with the increasing content of MgO. It indicates the weakening of the bonds of that particular functional group. On the other hand, the IR band at ~1144 cm^{-1} is shifted to the higher wave number with MgO content, which indicates to the strengthening of this functional group. Besides these bands, a band at ~1633 cm^{-1} is also observed which is due to the bending mode of O-H stretching in water [39]. This band becomes more prominent for samples with higher MgO content. According to the IR structural model, Mg ions can take a position in the vanadate chain or might be located between vanadate chains and layers. In the first condition, Mg ions break V-O-V bonds and try to form new V-O-Mg bridges. The influence of Mg ions on the V=O bond is restricted, and hence this band is preserved at ~1021 cm^{-1}. The second case, Mg ions will interact with V=O bond and leads to longer bond length, resulting in shifts towards a lower wave number (~1021 cm^{-1}), as observed in the present case. This shifting confirms that Mg ions can be located between vanadate chains, layer and the glass structure made up of VO_4 polyhedra. Thus, The IR band at ~1144 cm^{-1} might be due to the V-O-Mg bridges [39]. Based on FTIR study, we have proposed the mechanism for glass formation as depicted in Fig. 4.14. Further, the weight loss in TGA curves (as discussed in section 4.2.4.) also supports the change of oxygen state of vanadium ions in the presence of MgO.

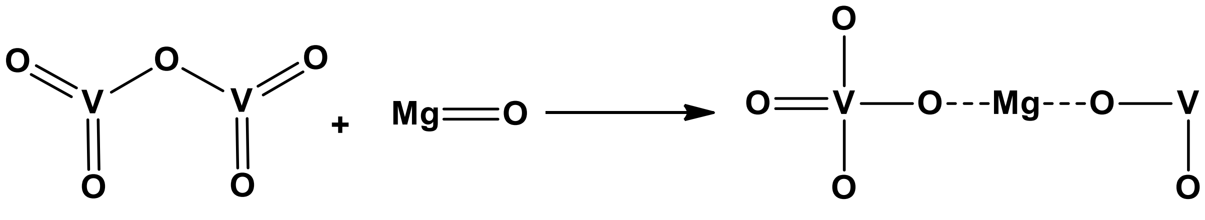

Fig. 4.14 The proposed mechanism of formation of VO_4 and VO_5 structural units with the doping of MgO in V_2O_5.

4.2.4 Thermal properties

Fig. 4.15 represents the differential thermal analysis (DTA) thermograph of MgO modified V_2O_5 samples. VM-0.05 and VM-0.10 samples exhibit two endothermic peaks at high temperature (≥634 °C).

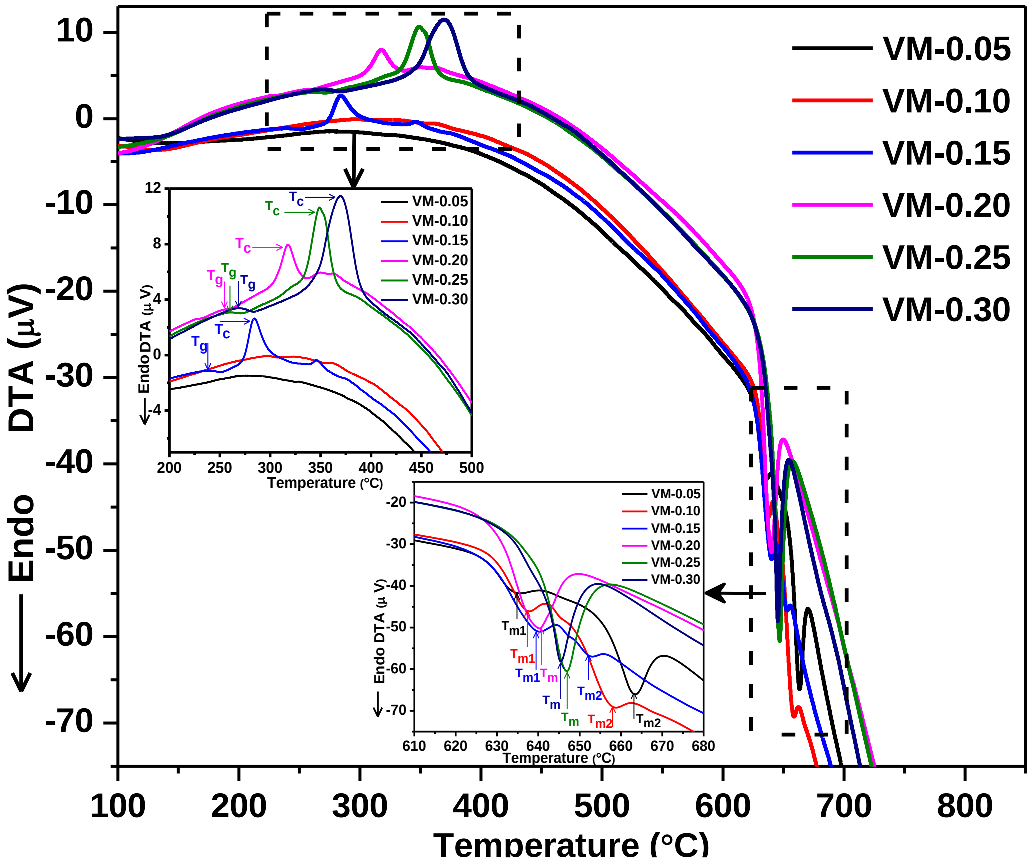

Fig. 4.15 DTA thermographs of the samples recorded with 10 °C heating rate. Inset shows magnified view of T_g, T_c and T_m of samples.

These endothermic peaks correspond to the double melting point T_{m1} and T_{m2} due to two different phases present in the samples, as also observed in case of lithium doped V_2O_5 samples (section 4.1.6). On the other hand, VM-0.15, VM-0.20, VM-0.25, VM-0.30 samples show endothermic peaks correspond to the glass transition temperature (T_g). After this temperature, exothermic peaks correspond to the glass crystallization temperature (T_c) followed by endothermic peaks related to the melting point (T_m) are observed [40]. A single dip corresponds to the T_g in VM-0.15, VM-0.20, VM-0.25 and VM-0.30 samples is observed. It can be concluded that VM-0.05 and VM-0.10 samples are crystalline in nature and VM-0.20, VM-

0.25, VM-0.30 samples are glass (amorphous) in nature whereas VM-0.15 sample is glass-ceramic, which is also supported by XRD results. The obtained values of characteristic temperatures (T_g, T_c, and T_m) and glass transition width (ΔT_g) from DTA thermograph of all the samples are given in Table 4.4.

Table 4.4 Thermal parameters of MgO doped V_2O_5 samples obtained from the DTA

Sample ID	T_g (°C)	T_c (°C)	T_m (°C)	T_c-T_g (°C)	T_m-T_c (°C)	ΔT_g (°C)	F	T_c-T_g/ T_m-T_c
VM-0.05	-	-	T_{m1}=634, T_{m2}=663	-	-	-	-	-
VM-0.10	-	-	T_{m1}=637, T_{m2}=658	-	-	-	-	-
VM-0.15	243	283	T_{m1}=640, T_{m2}=652	40	356	20	0.29	0.11
VM-0.20	256	318	640	62	322	16	0.41	0.19
VM-0.25	263	348	646	85	298	22	0.28	0.28
VM-0.30	274	370	645	96	275	26	0.22	0.34

Among these glasses, the VM-0.15 glass shows two close exothermic crystallization peaks (T_{c1} and T_{c2}). Amongst which, the T_{c1} is more pronounced and used for the further thermal studies. This also indicates that VM-0.15 sample is phase separated and has two mechanisms of crystallization in the glass [41]. It is interesting to notice that the T_g and T_c both increase with the MgO content. It is associated to the higher bond length, better cross-linking density, the closeness of packing and rigidity of glass units [30, 39, 42, 43]. In addition to this, T_g exhibits a direct correlation with a coordination number of glass former and formation of NBOs, which supports to the depolarization of the network structure [6]. Hence, it seems that gradual change of V^{5+} to V^{4+} ions lead to the formation of a glassy network with VO_4 tetrahedral units. The higher MgO content may lead to the formation of the VO_3 units to disturb the glass network and formed NBOs [6]. Additionally, T_c-T_g, which is proportional to the glass forming ability increases, whereas, T_m-T_c, which is inversely proportional to the glass forming ability decreases with MgO content as shown in Table 4.4. Further, the glass forming ability parameter, i.e. Hruby’s parameter (T_c-T_g/ T_m-T_c) is calculated and found to increase with the MgO content.

VM-0.30 glass shows the highest Hruby's parameter (0.34), which indicates its highest glass forming ability as compared to other glasses [41].

Thermodynamic fragility recognizes how rapidly the dynamics of a material slow down as it is cooled to the glass transition temperature. Higher fragility glasses have relatively low T_g range or vice-versa. Thermodynamic fragility (F) is also calculated using the following relation and is depicted in Table 2 [44].

$$F = \frac{0.151 - \Delta T_g / T_g}{0.151 + \Delta T_g / T_g} \tag{4.8}$$

The thermodynamic fragility of MgO doped V_2O_5 samples have been calculated using equation (4.8) and found to decrease with MgO content except for VM-0.20 sample as shown in Table 2, which is attributed to the glass network getting closely packed [44, 45].

The TGA curves of the as-quenched samples are shown in Fig. 4.16.

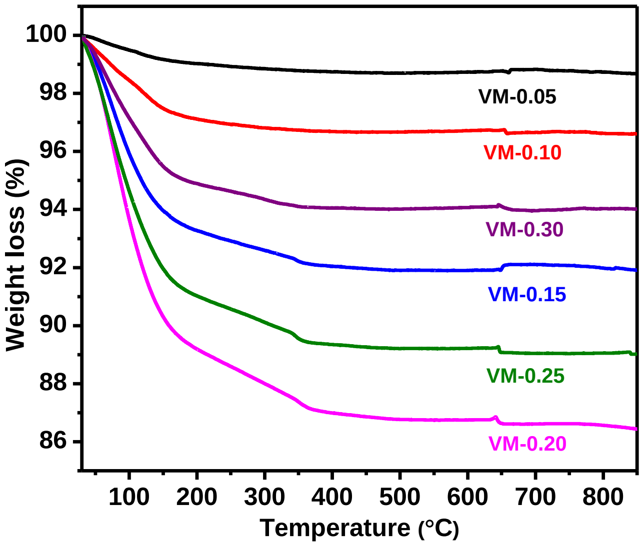

Fig. 4.16 Thermal stability behavior of the $V_{2-x}Mg_xO_{5-\delta}$ (0.15≤x≤0.30) as quenched samples.

The TGA curves exhibit weight loss from ~1 % to 12 % in all the samples within the temperature range of 30-350 °C. It is assigned to the loss of water molecule and reduction of V^{5+} to V^{4+} or V^{3+} ions [46, 47]. The loss of water molecules creates more porosity in the samples, which leads to a decrease in the overall conductivity as discussed in section 4.2.5. Weight loss increases with MgO content, and it is also a manifestation of reduction of V^{5+} to

V^{4+} and V^{3+} as confirmed in the FTIR spectra. Thereafter (>350 °C), with the addition of MgO, there is no change in the mass of all the samples. This suggests that MgO content decreases the thermal stability of the samples.

4.2.5 Conductivity studies

AC conductivity is a parameter which quantifies the electrical conduction of materials on the application of an electrical ac field. The frequency-dependent ac conductivity (σ_{ac}) of the samples is calculated with the help of dielectric data using the following relation [45]:

$$\sigma_{ac}(\omega) = \varepsilon_0 \omega \varepsilon'' = \omega \varepsilon' tan\delta \qquad (4.9)$$

Where, $\varepsilon_{0,}$ ε', ε'' and $tan\ \delta$ are the permittivity of free space, real permittivity, imaginary permittivity and tangent of loss, respectively. The variation of AC conductivity with frequency at a discrete temperature (50-300 °C, step size 50 °C) is represented in Fig. 4.17. All samples have approximately the same behavior in AC conductivity with temperature and frequency. It is observed that the conductivity is static (frequency independent) till ~10^6 Hz called a plateau region, which suggests that the ionic diffusion is random in the present samples [25]. It is due to the long range order transport and diffusion of mobile ions on the application of an electric field [48, 49]. Thereafter (>1MHz), a sudden increase in σ_{ac} is observed, which increases with temperature (Fig. 4.17(a)-(f)). The nature of the curve resembles with the conducting properties of the semiconductor. It is due to the fact that heat is sufficient to excite more electrons, consequently, more hoping from the valence band to the conduction band takes place and then σ_{ac} increases. Generally, in these types of glasses, the conductivity depends on the concentration of mobile ions [29]. The movement of mobile ions increases with increasing temperature resulting in the increase of the overall conductivity of glasses [49]. On the other hand, σ_{ac} decreases from 1.1×10^{-1} to 8.3×10^{-4} Sm^{-1} at 300 °C as the MgO content increases. It is assumed that this decrease in σ_{ac} is due to the structural changes occurs by replacement of V^{5+} ions by Mg^{2+} ions, which leads to significant decrease in nearest free pair O_2 ions, resulting in a disturbance in the polaronic conduction of vanadium ions [48]. This sort of hindrance in the path of polaron is responsible for the decrease in σ_{ac} of the samples [50, 51].

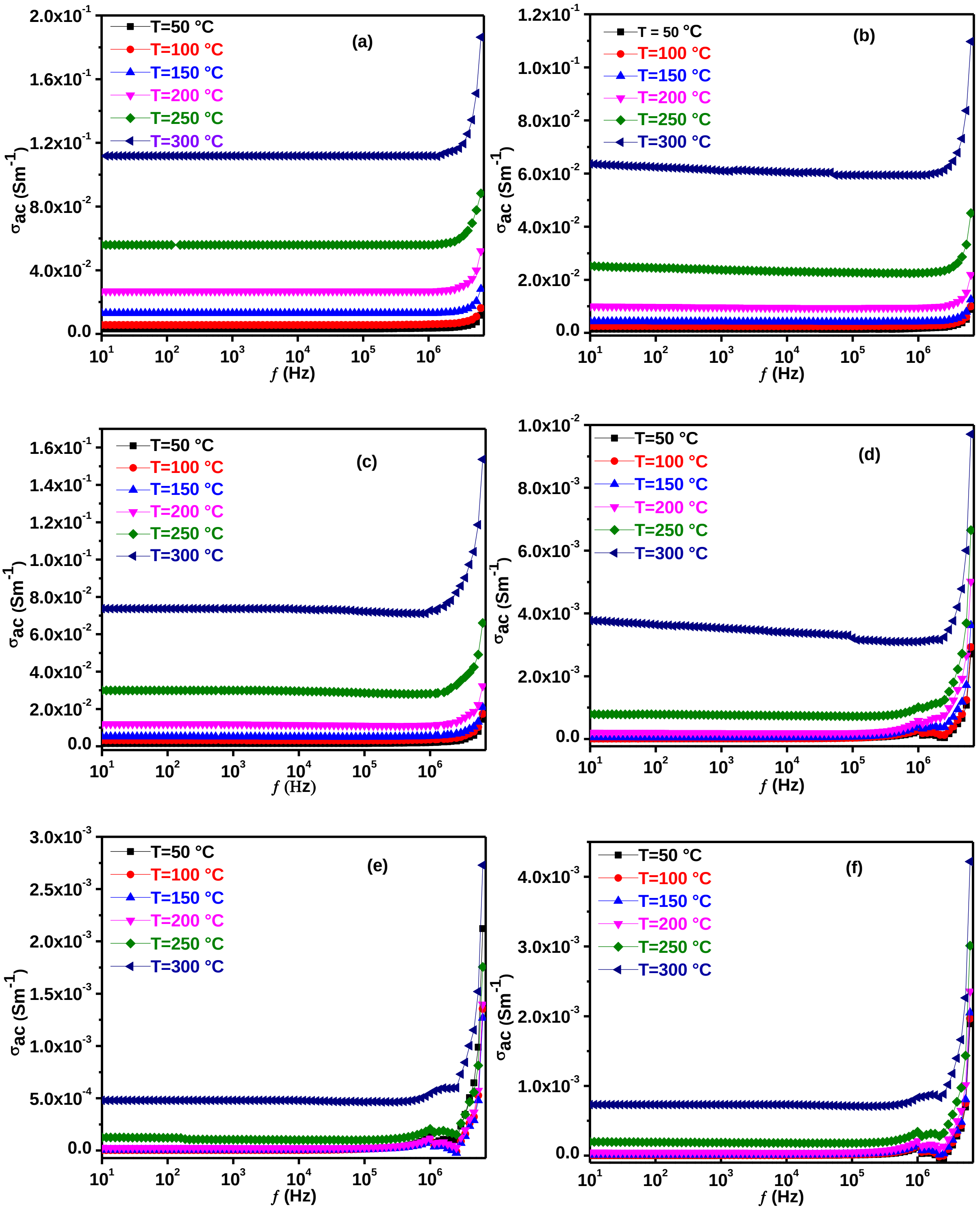

Fig. 4.17. AC conductivity behavior with frequency at different temperatures for (a) VM-0.05 (b) VM-0.10 (c) VM-0.15 (d) VM-0.20 (e) VM-0.25 (f) VM-0.30 samples.

We observed a very small increase in σ_{ac} value at *x*=0.15 and *x*=0.30 of MgO content (Table 4.5) and it may be due to the mixed transition effect (MTE) of V^{2+} and Mg^{2+} ions at the higher temperature [48, 50-52]. Both the samples (VM-0.15 and VM-0.30) are unique in the sense of VM-0.15 is a glass-ceramic and VM-0.30 exhibits the highest MgO content. So, it can be related to the presence of higher oxygen vacancies and NBOs. The conductivity behavior of the MgO modified V_2O_5 samples follows the Jonscher's universal power law as follows.

$$\sigma_{ac} = \sigma_{dc} + A\omega^n \tag{4.10}$$

where, σ_{ac} is the total conductivity, σ_{dc} is the dc conductivity (extrapolated); A is a temperature dependent constant of the material, ω is the angular frequency and n is a frequency and temperature dependent exponent that lies between 0 to 1 [53, 54]. The dc conductivity is calculated to extrapolate σ_{ac} at the lowest frequency (Fig. 4.17) and listed in Table 4.5.

Table 4.5 Summary of conducting parameters of all the samples.

Sample ID	E_a (eV) between 100-300 °C	σ_{ac} (Sm^{-1}) at 300 °C and 1MHz	σ_{dc} (Sm^{-1}) at 300 °C
VM-0.05	0.27	1.1×10^{-1}	1.1×10^{-1}
VM-0.10	0.29	5.9×10^{-2}	6.0×10^{-2}
VM-0.15	0.28	7.2×10^{-2}	7.3×10^{-2}
VM-0.20	0.40	3.1×10^{-3}	3.3×10^{-3}
VM-0.25	0.44	5.4×10^{-4}	5.0×10^{-4}
VM-0.30	0.38	8.3×10^{-4}	6.7×10^{-4}

Arrhenius plot between 1000/T and σ_{dc} were plotted and the following equation is used to find out the activation energy (E_a) of conduction:

$$\sigma_{dc} = \sigma_o \exp\left(-E_a/k_BT\right) \tag{4.11}$$

where, σ_o, E_a and k_B are a pre-exponential factor, activation energy and Boltzmann's constant, respectively [55]. The temperature dependent dc conductivity is investigated in the temperature range of 100 to 300 °C for in-depth analysis of conduction mechanism. Fig. 4.18 illustrates the variation of dc conductivity with a temperature of as-quenched samples. It is observed that the dc conductivity increases with increasing temperature, which is a typical semiconducting behavior and supports to the thermally activated mechanism in the present samples.

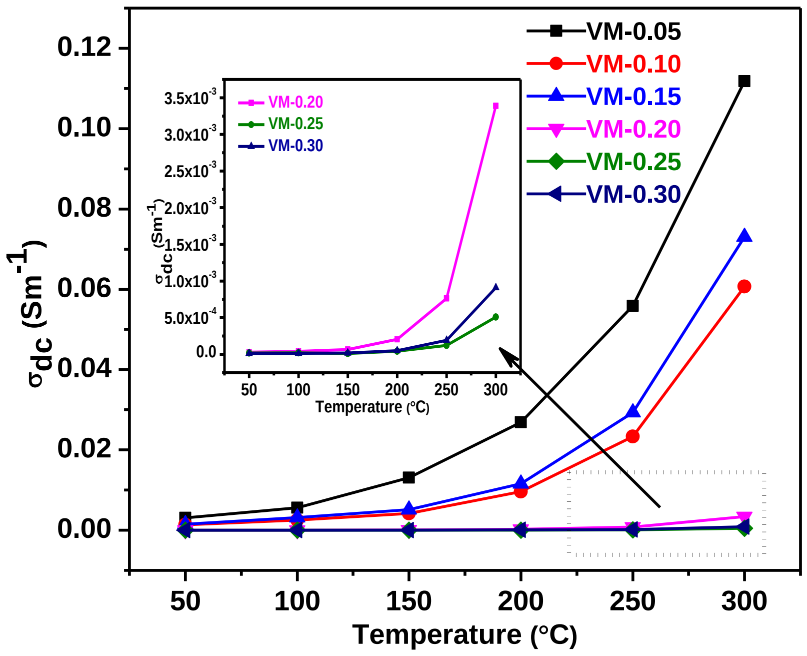

Fig. 4.18 DC conductivity behavior of the samples measured at different temperatures. Inset shows magnified view of dc conductivity behavior with temperature of VM-0.20, VM-0.25 and VM-0.30 samples.

Fig. 4.19 shows the variation of $ln\ \sigma_{dc}$ as a function of temperature and found to be linear up to a critical temperature $\theta_D/2$ (θ_D: Debye temperature). Thereafter, a change in slope from linearity is observed, which indicates temperature dependent E_a of conduction. This behavior supports to the small polaron hopping (SPH) conduction, which gives the non-adiabatic regime for such type of materials [56, 57, 58]. In other words, this non-linearity is due to the process involving activation energies, and movement of polaron or variable range carriers hopping [9]. The activation energy has been computed from the Arrhenius plots (Fig. 4.19) and the values are found different the high and low temperature regions (Table 3). The value of σ_{dc} is found to decrease from 1.1×10^{-1} to 9.9×10^{-4} Sm^{-1} at 300 °C with increasing concentration of MgO, whereas the activation energy increases from 0.27 to 0.38 eV. VM-0.25 glass shows the lowest conductivity as compared to other samples. The anomaly in the conductivity might be associated with the ordering of oxygen vacancies leads to decrease ionic conductivity [59]. Interestingly, the eutectic point of the $MgO-V_2O_5$ composition is also observed around 25 mol% MgO. At the eutectic point, the microstructure becomes more ordered. The ordering in oxygen vacancies and microstructure exhibits an opposite effect on overall conductivity. The ionic conductivity decreases whereas electronic conductivity increases in mixed electronic-ionic conductors. The dominance of ionic conductivity may be decreased the overall conductivity of this particular glass [60]. This can be explained based on the ratio of V^{4+} ion (V^{4+}/V_{total}) and disordering, which decreases with the addition of MgO content at the cost of V_2O_5. This results in an increase of the activation energy for conduction and decrement in the dc conductivity (Table 4.5).

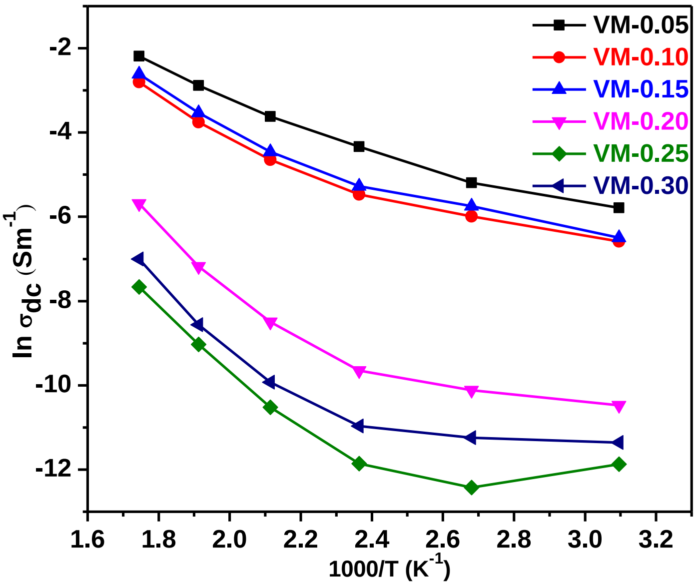

Fig. 4.19 Variation of ln(σ_{dc}) with 1000/T to find out the activation energy of the samples.

This means Mg^{2+} ions hinder the carrier transport and acts as a barrier in the hopping mechanism due to lack of O_2 bonds [61, 62]. A similar behavior is also reported by other researchers [62-64].

4.2.6 Correlation of dc conductivity with thermal parameters

Many ionic materials show a correlation of conductivity with their fragility index and T_g [65]. Low T_g denotes low viscosity, and in such type of materials, viscosity and conductivity can be coupled. The degree of coupling can vary with viscosity [66, 67]. Hence, the conductivity can be enhanced with decreasing T_g. According to glass physics, the fragility also has a remarkable effect on conductivity [65]. Fig. 4.20 illustrates the dependence of the dc conductivity at 300

°C on F and T_g as a function of the composition of the samples. It exhibits a clear trend of dc conductivity to become reduced at a high value of T_g and low value of F [64, 67]. T_g and F of the samples are obtained using DTA thermograph as discussed in section 4.2.4. The higher T_g and lower F are responsible for reducing the conductivity of these samples [65, 68]. Although, the variation of conductivity with T_g and F is not sufficient without taking care of the other parameters [65]. In summary, these materials can be potential candidates for applications in batteries. Though, more investigations are required to verify the applicability of this approach for such type of systems [65].

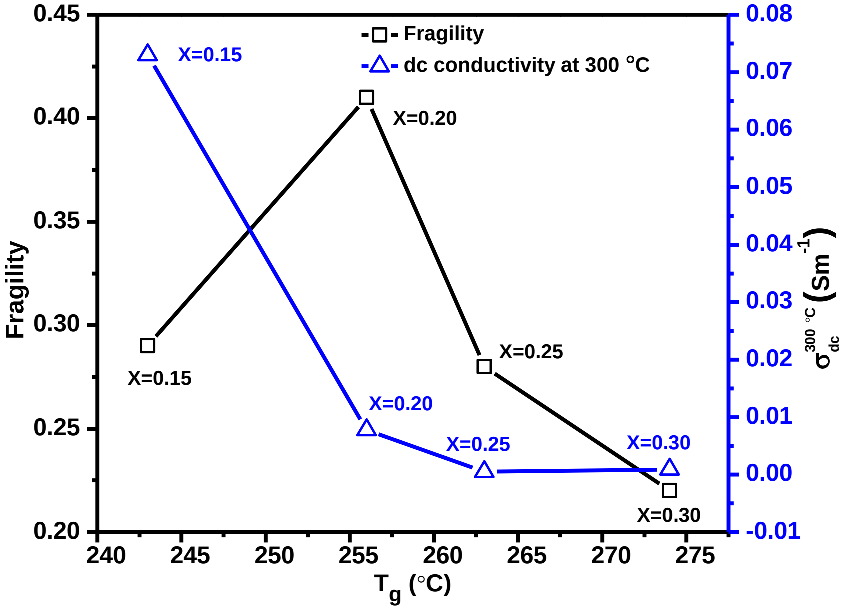

Fig. 4.20 Correlation of dc conductivity and fragility with the glass transition temperature of MgO modified $V_{2-x}Mg_xO_{5-\delta}$ systems.

4.3 Aluminium doped V_2O_5 ($V_{2-x}Al_xO_{5-\delta}$; $0.0 \le x \le 0.20$)

4.3.1 Physical properties

Various physical parameters such as apparent density, molar volume, ionic concentration and their inter-ionic distance of $V_{2-x}Al_xO_{5-\delta}$ (x=0-0.20) samples are obtained and depicted in Table 4.6. Variation in apparent density and molar volume as a function of Al_2O_3 ion concentration is also shown in Fig. 4.21 (a). It is observed that both the apparent density and molar volume decrease with the doping of Al_2O_3 in place of V_2O_5 (Table 4.6.). This decrement in apparent density is ascribed to the decrease in the molecular weight of the samples owing to the doping of lighter Al_2O_3 (101.96 $gmol^{-1}$) in place of heavier V_2O_5 (181.88 $gmol^{-1}$) [1].

Table 4.6 The obtained physical parameters of the prepared samples.

Sample ID	**Apparent density, ρ (gcm^{-3})**	**Molecular weight, M ($gmol^{-1}$)**	**Molar volume, V_m (cm^3mol^{-1})**	**Ionic concentration, N_i ($\times 10^{23} cm^{-3}$)**	**Inter-ionic distance, R_i (Al-O) (nm)**
VA-0.0	3.29	363.76	110.56	-	-
VA-0.05	3.26	359.76	110.35	0.81	23.0
VA-0.10	3.24	355.76	109.80	1.65	18.2
VA-0.15	3.22	351.77	109.24	2.48	15.9
VA-0.20	3.21	347.77	108.34	3.34	14.4

Density and molar volume exhibit the opposite trend to each other. But, in the present case, apparent density and molar volume decrease with the increasing doping of Al_2O_3 on the cost of V_2O_5. The molar volume is governed by molecular weight and density. In the present case, the change in molecular weight is taken place due to the fraction change in density for the same quantity of Al_2O_3 in V_2O_5. Consequently, the molar volume decreases with the increasing content of Al_2O_3 [20]. This anomalous behavior for different samples is also reported by other research groups [34, 69, 70]. On the other hand, the ionic concentration increases (0.81-3.3×10^{23} cm^{-3}) whereas their inter-ionic distance (Al-O) decreases (2.3-1.4×10^{-8} Å) as aluminum content increases as shown in Fig. 4.21(b). The concentration of ions is increased due to the increasing amount of Al^{3+} ions in place of V^{5+} ions [1].

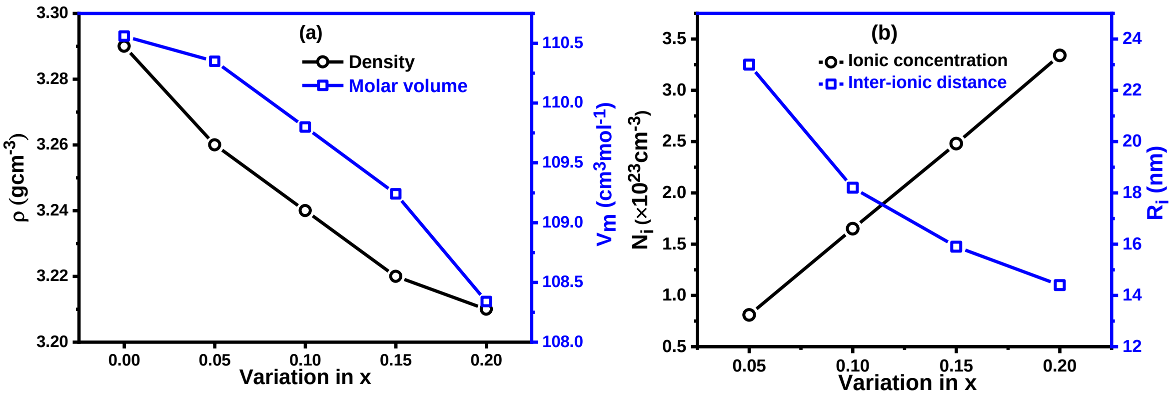

Fig. 4.21 Change in (a) density and molar volume and (b) ionic concentration and their inter-ionic distance as a function of x in $V_{2-x}Al_xO_{5-\delta}$.

The decrement in the inter-ionic distance can be associated with the Al^{3+}cation (0.53 Ǻ) replaces the V^{5+}cation (0.54 Ǻ) [34]. The increment in the ionic-concentration and decrement in the inter-ionic distance can be improved the hopping among ions. These physical parameters can be key factors to govern the conduction mechanism in the present samples as discussed in the next sections.

4.3.2 X-ray diffraction (XRD) analysis

XRD analysis is done to examine the effect of Al_2O_3 doping on the crystal structure of V_2O_5. Fig. 4.22 represents the XRD patterns of the $V_{2-x}Al_xO_{5-\delta}$ (x=0-0.20) ceramics. Several strong and weak diffraction peaks are detected in the XRD patterns of prepared samples. These diffraction peaks are indexed to the orthorhombic V_2O_5 phase (ICDD-01-086-2248). There is no secondary phase is observed in all the samples. The relative intensity of the diffraction peaks changes with the Al_2O_3 doping, suggesting a modification of the unit cell parameters [71]. The relative intensity ratio of (010) and (020) peaks become larger with the doping of Al_2O_3 into V_2O_5, which is associated with the positions of vanadium-ions in the unit cell [70].

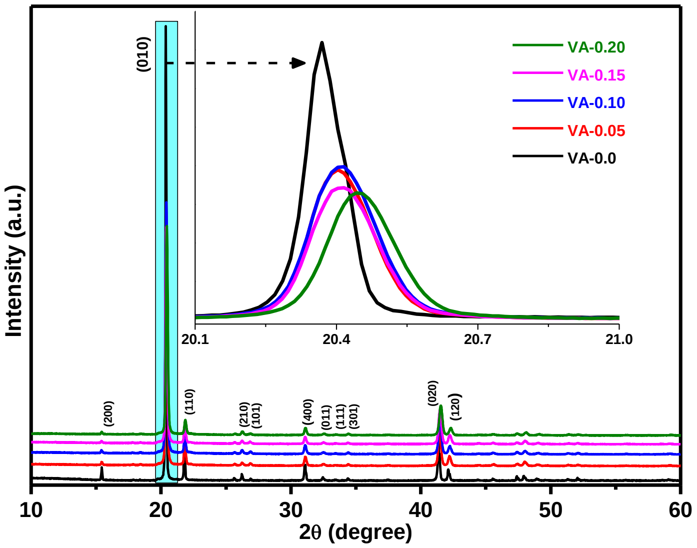

Fig. 4.22 XRD patterns of the undoped and aluminium doped V_2O_5 samples. inset shows the magnified view of high intense (010) diffraction peak.

Therefore, it is estimated that the conductivity of $V_{2-x}Al_xO_{5-\delta}$ (x=0-0.20) systems can be altered on the doping of Al^{3+} ions in place of V^{5+} ions in the crystal lattice of the system [71]. Also, for a distinct view of diffraction peaks shifting with the Al^{3+} doping in place of V^{5+}, the magnified view of the highest intense diffraction peak (010) is depicted in the inset of Fig. 4.22. The peak (010) shifts to a higher angle marginally due to the smaller ionic radii of Al^{3+} ion (0.53 Å) with VI coordination than V^{5+} ion (0.54 Å) with VI coordination. The higher angle shifting of peak (010) on the doping of Al^{3+} ions in V^{5+} ions suggest a compressive strain in the present samples [4]. To estimate the strain and microstructure parameters of the present samples, Williamson-Hall analysis has been done and discussed in the following section.

4.3.3 Williamson-Hall analysis (USM)

XRD profile analysis provides information about the phases, crystallite size and strain of the prepared ceramic samples. Pearson's VII peak function is used to obtain the peak position (2θ) and full width at half maxima (FWHM, β_{hkl}) of the X-ray diffraction peaks. Pearson's VII peak function gives more realistic results than the Lorentzian and Gaussian functions with the assumption of symmetry of Bragg's peaks. The representative curve fitting of the high intense (010) diffraction peak by Pearson's VII function is shown in Fig. 4.23 (a) and the obtained results are given in Table 4.7. Scherrer criterion is the volume-weighted quantity and used to obtain the crystallite size associated with the β_{hkl} as follows [47].

$$t = k\lambda / \beta_{hkl} cos\theta_{hkl} \tag{4.12}$$

where, k is the shape factor, λ is the wavelength of x-ray (1.540 Å), β_{hkl} is the full width at half maxima (FWHM) of diffraction peak in radians and θ_{hkl} is the Bragg's angle. Here, crystallite size merely depends on the broadening of the diffraction peaks. On the other hand, Stokes and Wilson have suggested the mathematical formulation for peak broadening associated with the strain in the materials as follows [72].

$$\beta_{hkl} = 4\,\varepsilon\, tan\theta_{hkl} \tag{4.13}$$

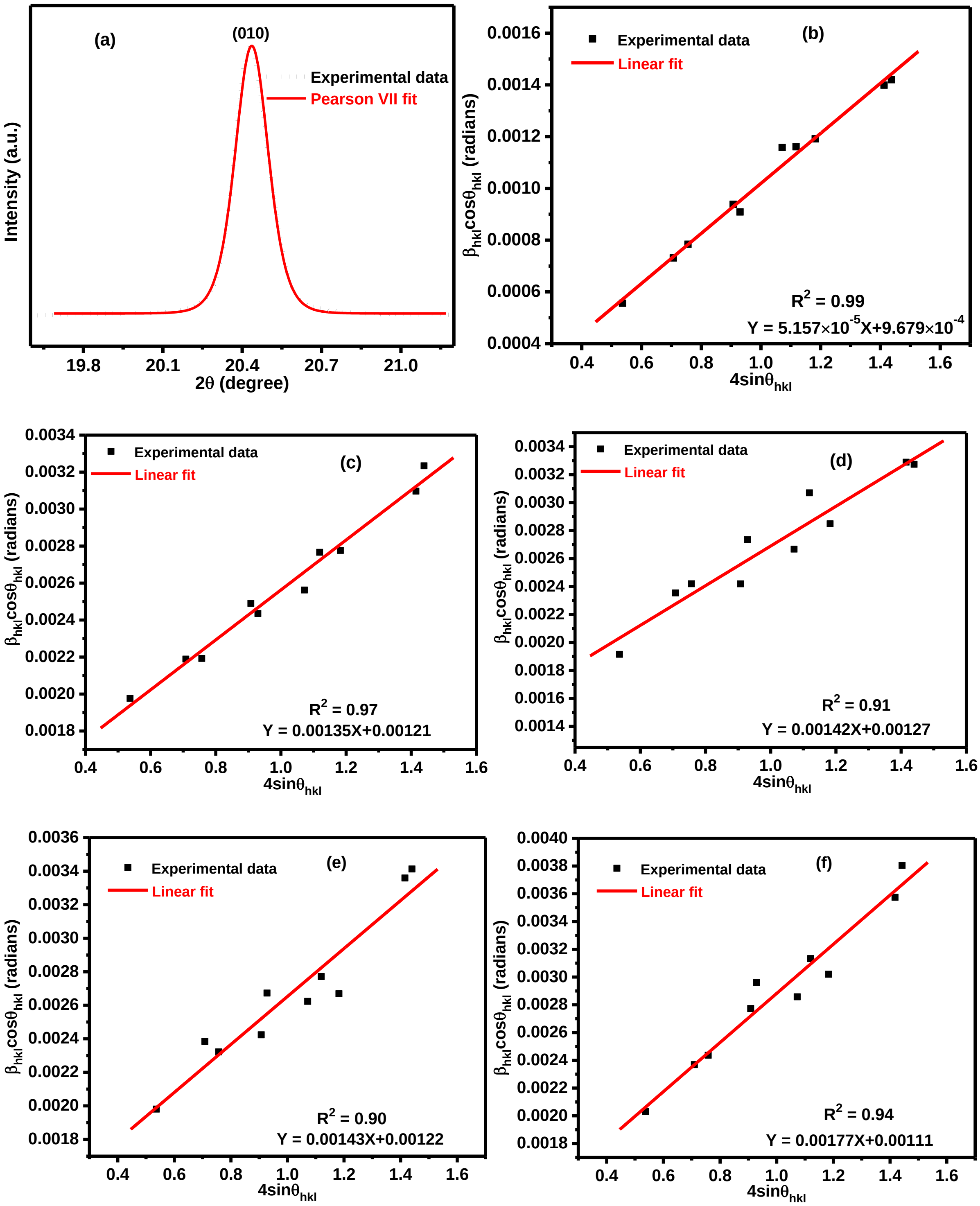

Fig. 4.23 The W-H analysis for all the samples, the crystallite size is extracted from the y-intercept of the fit. The strain is extracted from the slope (a) Pearson VII fitted data, (b-f) USM.

here, the obtained β_{hkl} value is the combination of both equations (Eq^n (4.12) & Eq^n (4.13)).

Williamson-Hall plot is employed to separate the individual effect as follows.

$$\beta_{hkl}\,cos\theta_{hkl} = {}^{k\lambda}/_{t} + 4\;\varepsilon\;sin\theta_{hkl} \tag{4.14}$$

The above-mentioned equation shows the uniform strain model (USM) of Williamson-Hall analysis. In this model, the strain distribution in the crystal is assumed to be isotropic. The crystallite size and strain are obtained by the intercept and the slope of the graphs plotted between $\beta_{hkl}\ cos\theta_{hkl}$ and 4 $sin\theta_{hkl}$, respectively, as shown in Fig. 4.23 (b)-(f). The estimated results from the USM model of the present samples are given in Table 4.7. The estimated crystallite size firstly decreases with increasing Al_2O_3 doping up to x=0.10 and then increases. The estimated crystallite size lies in the range of 143.25-124.92 nm. On the other hand, the estimated strain shows an increasing trend with increasing doping of Al_2O_3 into V_2O_5. This increasing trend of strain can be due to the peak broadening and size difference of Al^{3+} and V^{5+} ions [71, 72]. The positive value of strain also supports the existence of compression in the lattice in the present samples.

Table 4.7 Microstructural parameters of the prepared samples obtained by Williamson-Hall analysis.

Sample ID	**USM**		**FWHM (°)**
	ε ×10^{-5}	**t (nm)**	
VA-0.0	06	143.25	0.073
VA-0.05	135	114.59	0.138
VA-0.10	142	109.14	0.147
VA-0.15	143	113.65	0.148
VA-0.20	177	124.92	0.149

4.3.4 FTIR spectra analysis

The infrared spectra of $V_{2-x}Al_xO_{5-\delta}$ (x=0.0-0.20) ceramics exhibit absorption bands at 1629, 1382, 1026, 913, 808, 580, 531, 480 cm^{-1} as shown in Fig. 4.24. The bands located at 1629 and 1382 cm^{-1} are due to the H-O-H bending mode of the adsorbed water molecules, signifying the hygroscopic nature of the as-quenched samples [1, 39]. The characteristic vibration band located at 1026 cm^{-1} attributes isolated V=O vanadyl groups inVO_5 trigonal bi-pyramids [1]. This absorption band slightly shifts to a lower wavenumber with the doping of Al^{3+} ions in place of V^{5+} ions. It might be associated with the reduction of V_2O_5 from V^{5+} to V^{4+}/V^{3+} on Al^{3+} doping into V^{5+}. Therefore, the strength of the V=O bond decreases owing to the increasing V-O length due to the radius of vanadium ion increases as the oxidation state changes from V^{5+} to V^{4+}/V^{3+}. A shoulder generates at 913 cm^{-1} and becomes more prominent with the doping of Al^{3+} ions. The broadness of this band also decreases with Al^{3+} ions doping on the cost of V^{5+}. This band is assigned to the symmetric and asymmetric stretching vibrations of the isolated VO_2 groups in VO_4 polyhedra. Another band at 808 cm^{-1} is associated with the vibrations of isolated [VO_4] tetrahedral [72, 73]. The band at 580 cm^{-1} is assigned to the bending of V-O-V bonds and this band is more resolved with the highest aluminum doping (x=0.20) [74, 75].

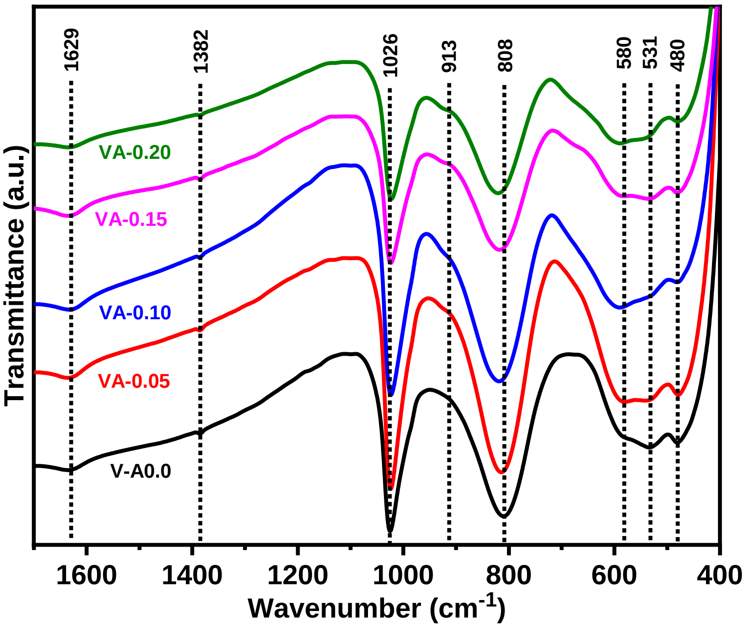

Fig. 4.24 FTIR spectra of the undoped and aluminium doped vanadium oxide samples.

The band at 531 and 480 cm^{-1} are assigned to the symmetric stretching vibration of V-O-V bonds [75, 76]. The sharpness of the band (480 cm^{-1}) decreases with aluminum doping in the present samples. On the other hand, the IR bands located at 913, 808, 580 cm^{-1} shifts to a higher wavenumber on the Al^{3+} ions doping in V^{5+} ions due to the decreasing V-O bond length, which leads to the strengthening of this lattice vibration. According to the IR assumptions, Al^{3+} ions can be located in the V-O-V chain or might be positioned between V-O-V chains and layers [1, 73]. In the first case, Al^{3+} ions break V-O-V bonds and try to form V-O-Al bridges. The impact of Al^{3+} ions on the V=O bonds is restricted. Therefore, this band is conserved at ~1026 cm^{-1} [1, 73]. In the second case, Al^{3+} ions can interact with V=O bonds causing the longer bond length of V-O which leads to the shifting of the band (~1026 cm^{-1}) to a lower wavenumber as observed in the FTIR spectra [1]. This shifting approves the location of Al^{3+} ions between vanadate chains and layers. Based on the shifting and shape of the IR band as discussed above, it can be concluded that vanadium exists in the mixed state in the present samples.

4.3.5 Raman spectra analysis

Raman spectra of $V_{2-x}Al_xO_{5-\delta}$(x=0.0-0.20) ceramics are shown in Fig. 4.25. Raman spectra can be described in two modes. The low-frequency modes are described as external modes of V_2O_5 units. These low-frequency modes are generated due to the translational modes of V_2O_5 units and the relative motion of V_2O_5 layers [77].

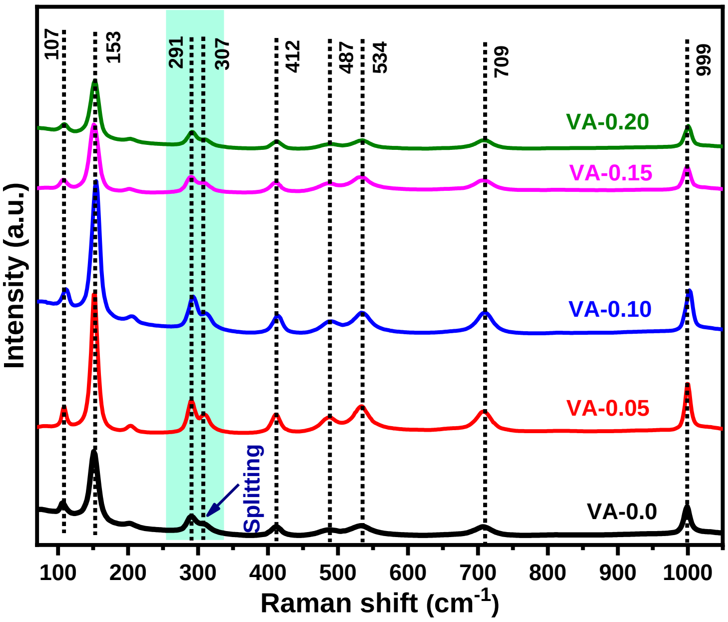

Fig. 4.25 Polarized Raman spectra of the undoped and aluminium doped V_2O_5 samples.

On the other hand, medium and high-frequency modes (internal modes) are related to the O-V-O and V-O-V bending and V-O stretching [77]. The translational modes at 107 and 153 cm^{-1} are assigned to the vibration in a V-O-V atomic chain. The strong intensity of the translational mode at 153 cm^{-1} signifies the long-range order in the planes of V_2O_5 [78]. The intensity of this translational mode (153 cm^{-1}), first increases with Al_2O_3 doping up to x=0.10 and then decrease. The mode at 291 and 412 cm^{-1} are associated with the bending vibration of the V=O while a low-intensity mode at 487 cm^{-1} is assigned to the stretching of the V-O-V bonds [79]. The mode at 291 cm^{-1} splits into 307 cm^{-1} which is associated with the stretching of the V-O-V bonds. Another two modes at 534 and 709 cm^{-1} are attributed to the stretching and bending of the V-O bonds, respectively [79]. Another mode at 999 cm^{-1} is ascribed to the terminal oxygen (V=O) stretching due to the unshared oxygen [79]. The intensity of this mode first increases with Al_2O_3 doping up to x=0.10 and then decreases. It might be related to the formation of minor glassy phase at higher doping of Al_2O_3 i.e. VA-0.15 and VA-0.20 samples. The presence of all the vibrations suggesting the structural changes on the doping of Al_2O_3 into V_2O_5 in the present samples.

4.3.6 Optical properties

The optical properties of $V_{2-x}Al_xO_{5-\delta}$ (x=0-0.20) ceramics are examined by diffused reflectance spectra as shown in Fig. 4.26 (a)-(b). The undoped sample exhibits the highest reflectance (25%) whereas the sample with the highest doping of Al_2O_3 (x=0.20) has the minimum reflectance (21%) in the wavelength range of 420-600 nm. This quenching in reflectivity may be associated with optical phonon confinement in the present samples [17].

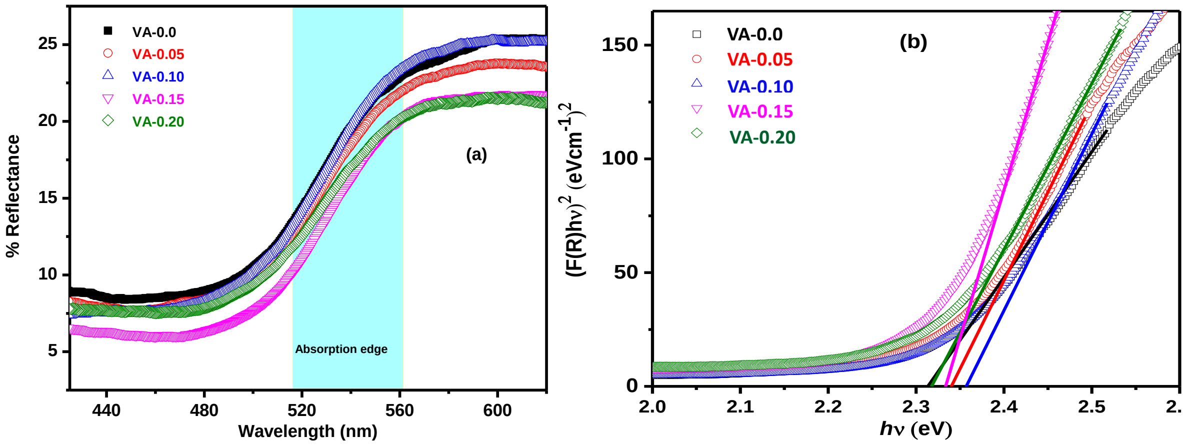

Fig. 4.26 (a) Diffused reflectance spectra and (b) Tauc plots to find out the optical band gap of the aluminium doped V_2O_5 samples.

These samples absorb visible radiation at ~550 nm wavelength. However, this absorption edge slightly shifts with aluminium doping in place of vanadium. Also, the absorption edges are sharply defined (Fig. 4.26(a)), which is associated with the crystalline nature of the samples as evident from the XRD patterns of the samples. The Kubelka-Munk function ($F(R) = (1-R)^2/2R$) was used to obtain the optical band gap energy E_g of the samples [19, 31]. The optical band gap energy was calculated by applying Tauc plots (Fig 4.26 (b)) between $(F(R)h\nu)^2$ and photon energy ($h\nu$). The change in the optical band gap is governed by the structural changes with aluminum doping on the cost of vanadium [80, 81]. The obtained band gap energy values lie in the range of 2.31-2.35 eV (Table 4.8). The optical band gap increases with an increase in aluminium doping up to x=0.10 and then decreases. VA0 sample exhibits the lowest band gap (2.31 eV) while VA-0.10 sample shows the highest band gap (2.35 eV). The increasing band gap reduces electron-hole (e-h) recombination probabilities [81, 82]. The higher doping of Al_2O_3 (x=0.20) in place of V_2O_5 leads to an enrichment in the degree of localization of electrons, resulting in an increase in donor centers. This increment in donor centers due to doping of Al_2O_3 (x>0.10) could be responsible for decreasing the optical band gap energy of the samples [81, 82].

Table 4.8 Conductivity and optical band gap energy of Al_2O_3 doped V_2O_5 samples.

Sample ID	**σ_{dc} (Sm^{-1}) at 400 ^{o}C**	**E_a (eV)**	**E_g (eV)**
VA-0.0	0.36	0.22	2.31
VA-0.05	0.37	0.26	2.34
VA-0.10	0.44	0.28	2.35
VA-0.15	0.34	0.27	2.33
VA-0.20	0.22	0.26	2.31

4.3.7 Thermal properties

Fig. 4.27 (a) displays the typical differential thermal analysis (DTA) thermographs of the as-quenched powder samples. An endothermic peak at ~650 ^{o}C temperature corresponds to the melting of the orthorhombic V_2O_5 phase as identified in the XRD result. The endothermic peak initially shifts to a higher temperature with increasing doping of Al_2O_3 up to x=0.10 then shifts marginally to a lower temperature. Also, this endothermic peak becomes broader with increasing doping of Al_2O_3 up to x=0.10, which signifies disordering in the present samples. Fig. 4.27 (b) represents the thermogravimetric analysis (TGA) thermographs to investigate the structural changes and reduction behavior of the $V_{2-x}Al_xO_{5-\delta}$(x=0.0-0.20) systems. TGA graphs show weight loss from ~1 to 2.5 % in the temperature range of 40-650 °C. This weight loss can be associated with the loss of adsorbed water molecules and the reduction of vanadium oxide from V^{5+} to V^{4+} $(2V^{5+} + O^{2-} \rightarrow 2V^{4+} + O_2 \uparrow)$ [1]. The weight loss increases as the doping of Al_2O_3 increases. The increase in weight loss can be associated with the structural changes in oxidation states of vanadium due to the Al_2O_3 doping on the cost of V_2O_5.

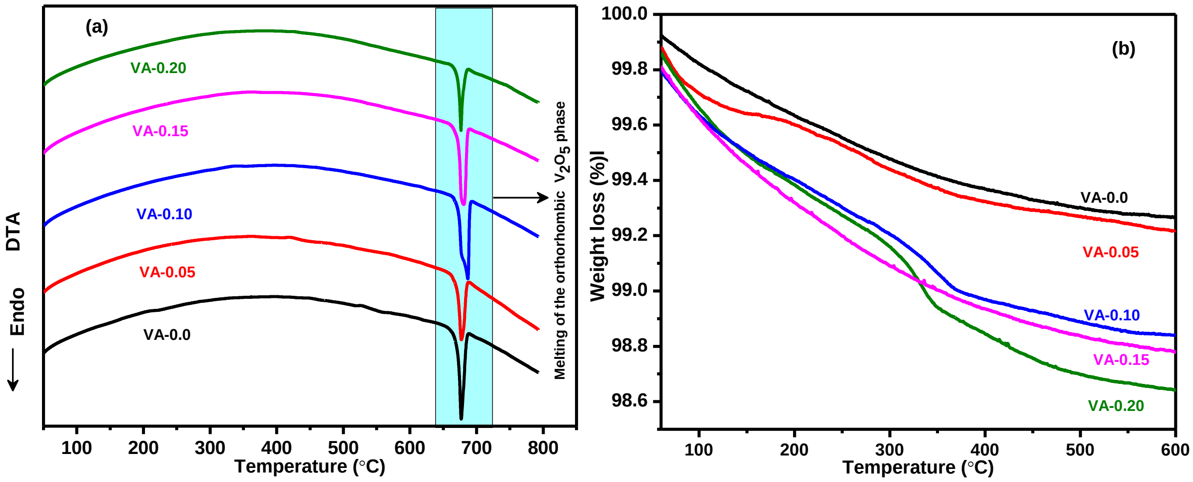

Fig 4.27 (a) DTA thermographs; and (b) thermal stability nature of undoped and aluminium doped V_2O_5 samples measured at 10 °C heating rate.

4.3.8 Conductivity studies

Fig. 4.28 (a)-(e) represents the change in conductivity with frequency at discrete temperatures (50-450 °C, ΔT=50 °C) for the prepared samples. It is observed that conductivity is frequency independent up to ~10^5 Hz (plateau region). This plateau region signifies the random diffusion of ions owing to the long-range order transport on the application of the AC field [1]. On the other hand, conductivity is frequency-dependent (dispersion region) at a higher frequency (>10^5 Hz) and increases with increasing frequency due to the hopping of carriers increases [81].

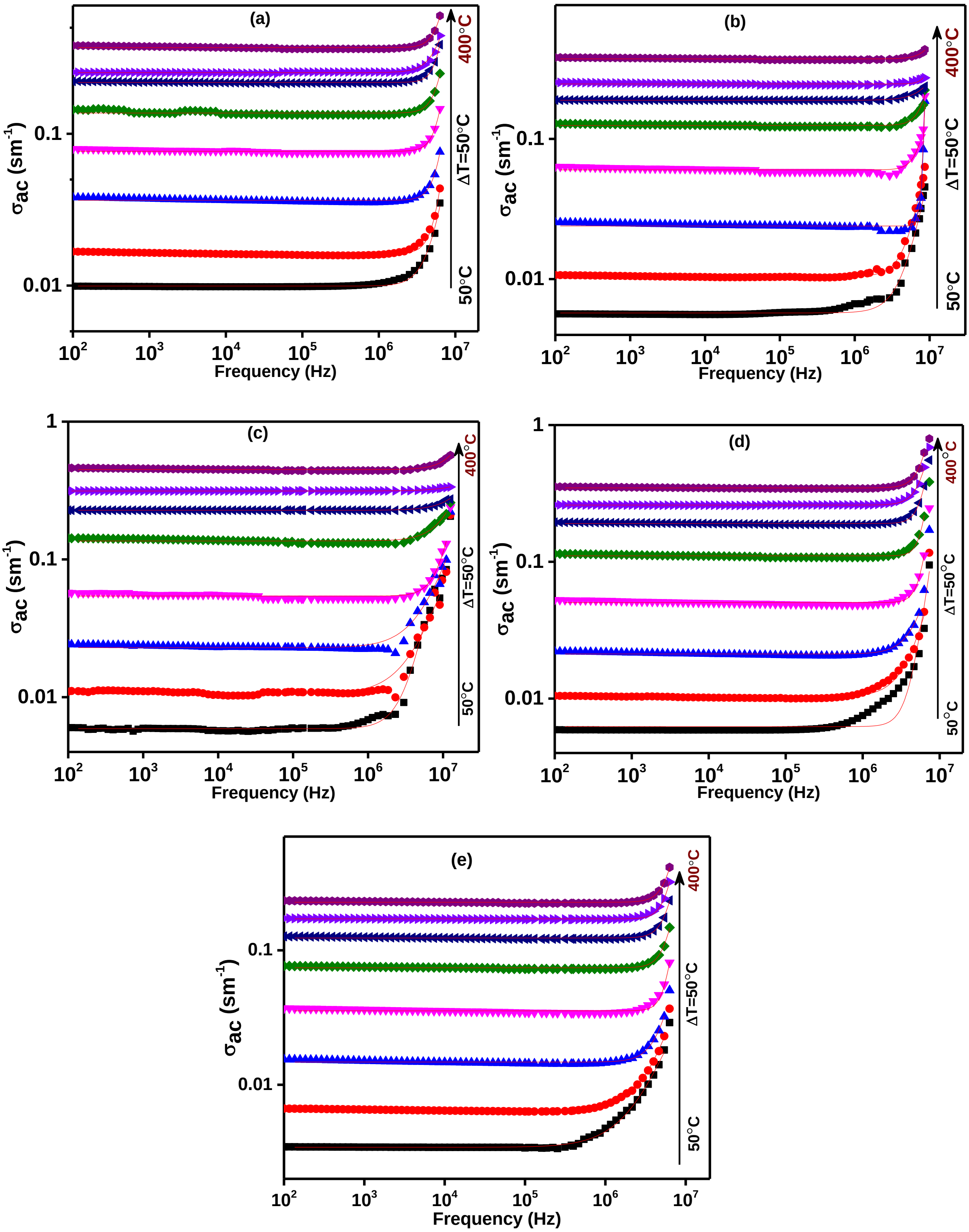

Fig. 4.28 Variation of AC conductivity as a function of frequency at discrete temperatures (50-400 °C, Δt=50 °C) for (a) VA-0.0 (b) VA-0.05 (c) VA-0.10 (d) VA-0.15 and (e) VA-0.20 samples.

The change in conductivity from frequency-independent to frequency-dependent signifies the establishment of conductivity relaxation phenomenon in the present samples [83]. It is observed that the dispersion frequency (at which the dispersion occurs) shifts to a higher frequency with increasing temperature. It is also observed that ac conductivity increases with increasing temperature which suggests a semiconductor nature of the samples as mentioned in the optical properties section [1]. In general, conductivity is governed by the types, concentration and mobility of charge carriers. The mobility of charge carriers increases with increasing temperature, which leads to an increase in conductivity [84, 85]. This behavior of conductivity satisfies Jonscher's power law in which AC conductivity (σ_{ac}) can be written with DC conductivity (σ_{dc}) as follows.

$$\sigma_{ac}\,(\omega, T) = \sigma_{dc}(T) + A\omega^{s} \tag{4.15}$$

where, A is the temperature-dependent constant, ω is the angular frequency and s is the temperature and frequency-dependent exponent and generally lies in the range of 0 to 1. The DC conductivity is obtained by applying Jonscher's power law as shown in Fig. 4.28 (a)-(e) and the obtained values are given in Table 4.8. This thermally activated DC conductivity can be described by the Arrhenius equation as follows [84]:

$$\sigma_{dc} = \sigma_0 \exp\,(-E_a/k_B T) \tag{4.16}$$

where, σ_0 is the pre-exponential factor, E_a is the activation energy and k_B is the Boltzmann's constant. Fig. 4.29 represents the Arrhenius plots of the $V_{2-x}Al_xO_{5-\delta}$ (x=0-0.20) ceramics. The obtained activation energy values of the prepared samples are given in Table 4.8. The DC conductivity increases with an increase in temperature due to the thermally activated nature of the prepared samples [84, 85]. The movement of mobile ions increases as temperature increases which leads to an increase in the overall conductivity of the present samples [85, 30]. The DC conductivity and activation energy increase with increasing doping of Al_2O_3 up to x=0.10 and then decreases (Fig. 4.30). VA-0.10 sample exhibits the highest DC conductivity (0.44 Sm^{-1}) whereas VA-0.20 sample shows the lowest DC conductivity (0.22 Sm^{-1}) at 400 ºC. The ordering of oxygen vacancies above the critical doping of Al_2O_3 (x>0.10) can be responsible to decrease the conductivity of the present samples [32, 86].

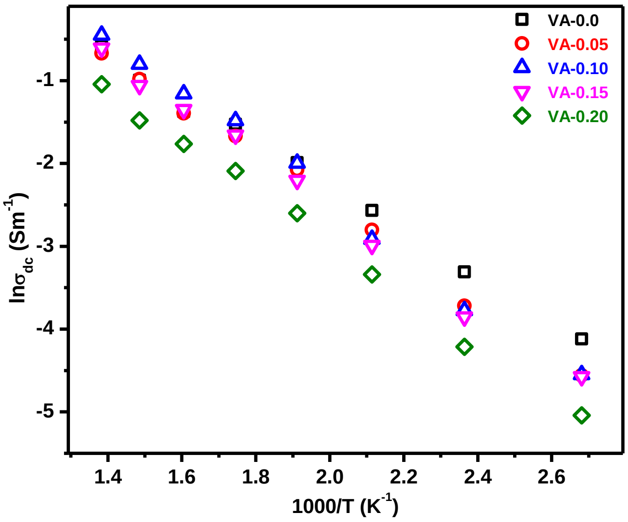

Fig. 4.29 Arrehenius plots (*ln* σ_{dc} vs *1000/T*) to calculate the activation energy of the undoped and Al_2O_3 doped V_2O_5 samples.

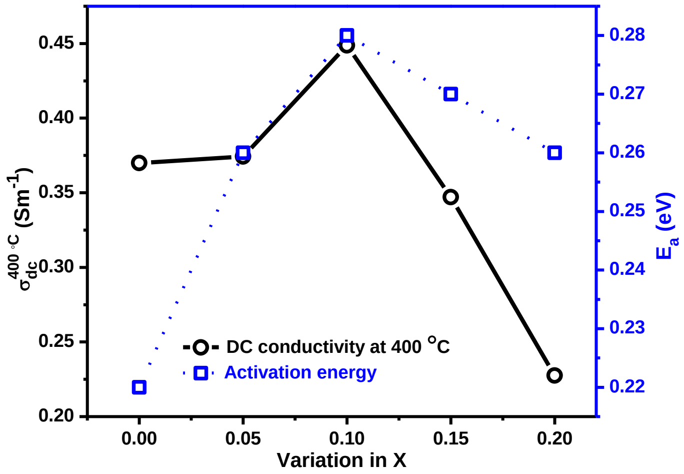

Fig. 4.30 Change in DC conductivity and activation energy with Al_2O_3 doping into V_2O_5.

This anomalous behavior of conductivity is also supported by the estimated crystallite size as discussed in the Williamson-Hall analysis section. In addition, vanadates exhibit the contribution of both electronic and ionic conductivity [87, 80]. In vanadate, conductivity also depends on the ratio $\beta = V^{5+}/V^{4+}$ and decreases with increasing β [88]. There is a possibility to decrease β due to an increase in the reduction of vanadium $(V^{5+} \rightarrow V^{4+})$ after critical doping of Al_2O_3 (x>0.10), resulting in an increase in the electronic contribution. The increase in electronic contribution can be responsible to decrease the overall conductivity of the present samples.

4.4 Titanium doped V_2O_5 ($V_{2-x}Ti_xO_{5-\delta}$; $0.15 \leq x \leq 0.30$)

4.4.1 Physical properties

The density decreases from 3.29 to 3.22 gcm^{-3}, congruent with an increase in molar volume from 54.77 to 55.45 cm^3mol^{-1} as the titanium doping increases on the cost of V_2O_5 as illustrated in Fig. 4.31 (a), and given in Table 4.9. Since, density is an additive property so that the decrement in density can be explained based on the molar mass of V_2O_5 and TiO_2. This decrement in density is due to the lighter molar mass of dopant (TiO_2; 79.86 $gmol^{-1}$) than host (V_2O_5; 181.88 $gmol^{-1}$) [1]. Also, the VO_4 unit increases due to the conversion of VO_5 into VO_4 unit due to the doping of TiO_2 as discussed in FTIR and Raman analysis. The increase in VO_4 units encourages an increase in molar volume, which leads to a decrease in density. In the present case, the decrease in density is lower as compared to the decrease in molecular weight. Consequently, the molar volume increases with the increase in doping of TiO_2.

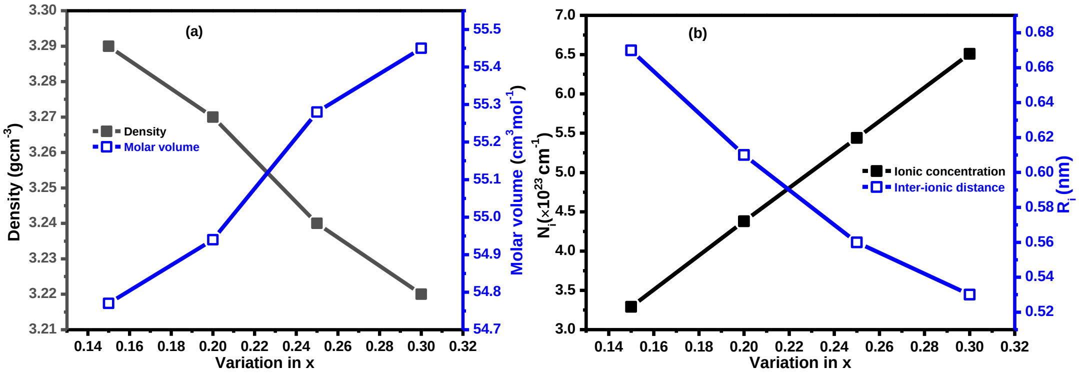

Fig. 4.31 (a) Change in density and molar volume and (b) change in ionic concentration and their inter-ionic distance with variation of x in $V_{2-x}Al_xO_{5-\delta}$

The increase in molar volume supports the formation of oxygen vacancies on the TiO_2 doping in V_2O_5 due to the transformation of VO_5 into VO_4 units. The decrease in density supports an increase in free volume, which directly affects the conduction mechanism by increasing the mobility of charge carriers in the samples. Some other physical parameters (ionic concentration and their inter-ionic distance) are also calculated to confirm the opposite trend of density and molar volume. Fig. 4.31 (b), represents the change in ionic concentration and their inter-ionic distance as a function of TiO_2 doping in the place of V_2O_5. It is observed that ionic concentration increases, whereas inter-ionic distance decreases with the TiO_2 doping in the place of V_2O_5. The decrease in *Ri* can be due to smaller cation (V^{5+}, 0.54 Å) that replaces the bigger one (Ti^{4+}, 0.60 Å).

Table 4.9 Physical parameters of the $V_{2-x}Ti_xO_{5-\delta}$ (x=0.15-0.30) samples.

Sample ID	Density, ρ (gcm^{-3})	Molecular weight, M ($gmol^{-1}$)	Molar volume, V_m (cm^3mol^{-1})	Ionic concentration, N_i ($\times 10^{23}cm^{-3}$)	Inter-ionic distance, R_i (nm)
VT-0.15	3.29	180.21	54.77	3.29	0.67
VT-0.20	3.27	179.66	54.94	4.38	0.61
VT-0.25	3.24	179.11	55.28	5.44	0.56
VT-0.30	3.22	178.55	55.45	6.51	0.53

4.4.2 X-ray diffraction (XRD) analysis

Fig. 4.32 illustrates the XRD patterns of the $V_{2-x}Ti_xO_{5-\delta}$ (x=0.15-0.30) samples. The characteristic XRD patterns of samples are matched with the orthorhombic V_2O_5 phase (ICDD-01-086-2248).

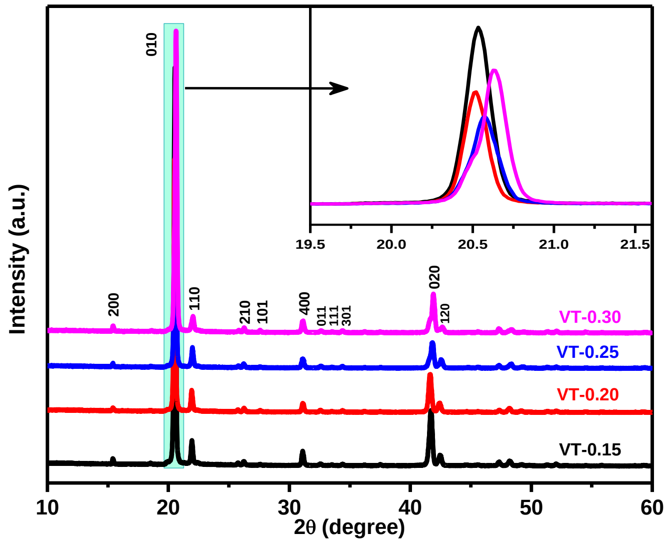

Fig. 4.32 XRD patterns of the titanium doped V_2O_5 samples. Inset shows the magnified view of high intense (010) diffraction peak.

The relative intensity of the observed diffraction peaks is changed with the titanium doping, signifying a modification in the lattice parameters. The relative intensity ratio of (010) and

(020) peaks is changed with Ti doping, suggests a change in the positions of vanadium-ions. So, it is expected that the conduction phenomenon in $V_{2-x}Ti_xO_{5-\delta}$ (x=0.15-0.30) samples may be affected by the Ti^{4+} ions doping in place of V^{5+} ions. In addition, to analyze the Ti doping effect on V_2O_5, a zoomed view of (010) peak is shown in the inset of Fig. 4.32. The position of (010) peak changes (shifting to a higher angle) with the Ti doping owing to the size difference between Ti^{4+} and V^{5+} ion [90].

4.4.3 FTIR spectra analysis

The IR spectrum of $V_{2-x}Ti_xO_{5-\delta}$ (x=0.15-0.30) shows the expected absorbance band of vanadia around 1138, 1020, 832, 607 and 483 cm^{-1} as shown in Fig. 4.33. The sharp band around 1020 cm^{-1} attributes to the isolated V=O vanadyl groups in the $[VO_5]$ trigonal bi-pyramids [1]. This characteristic stretching band also supports the layer structure of V_2O_5 in the present samples. The broad band at 832 cm^{-1} is associated with the vibrations of the isolated $[VO_4]$. Another broad band at 607 cm^{-1} is due to the stretching modes of V-O-V chains [91, 92]. The broadness of the IR bands is associated with the presence of different structural units of the same element with variable oxygen arrangement. Thus, there are several structural units of vanadium with variable oxygen in the present samples. In addition, the bands around 607 and 832 cm^{-1} shift to a higher wavenumber with Ti doping due to the decrease in V-O bond length. This decrease in V-O bond length represents the strengthening of this vibration with Ti doping. Consequently, higher energy is required for these lattice vibrations. The band at 483 cm^{-1} can be assigned to the bending modes of the V_2O_5 network consisting of $[VO_5]$ polyhedral [91, 92]. The sharpness of this band decreases on the doping of Ti in place of V_2O_5. According to the IR assumptions, the shifting of the bands (607 and 832 cm^{-1}) to a higher wavenumber can also be explained by the indirect attack of Ti^{4+} ions on the isolated V=O bonds [91]. It is interesting to notice that, along with the shifting of these bands (607 and 832 cm^{-1}), a band at 1138 cm^{-1} appear, which is an indication of a direct attack of the Ti^{4+} ions on the isolated V=O bonds and the formation of V-O-Ti chains.

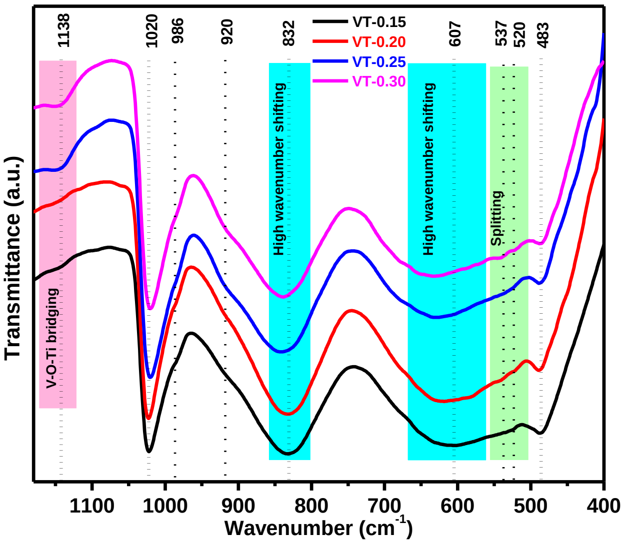

Fig. 4.33 FTIR spectra of $V_{2-x}Ti_xO_{5-\delta}$ (x=0.15-0.30) samples.

Consequently, $[VO_5]$ groups are transformed into $[VO_4]$ groups [91]. Thus, the band at 1138 cm^{-1} might be due to the V-O-Ti bridges and this band becomes more pronounced with increasing doping of TiO_2 into V_2O_5 [1, 92]. The change in positions of bands towards high wavenumber or lower wavenumber signifies the structural changes due to the Ti doping in place of V_2O_5 in the present samples.

4.4.4 Raman spectra analysis

The Raman spectra of $V_{2-x}Ti_xO_{5-\delta}$ (x=0.15-0.30) samples show the expected signals around 107,150, 204, 290, 308, 409, 488, 532, 705 and 998 cm^{-1} as presented in Fig. 4.34. The characteristic Raman band at 998 cm^{-1} occurs due to the stretching of V=O groups in pure V_2O_5 [14]. The intensity of the V=O band decreases with Ti doping on the cost of V_2O_5. The Raman bands at 532 and 705 cm^{-1} are assigned to the stretching and bending of the V-O bond, respectively. While a low-intensity Raman band at 488 cm^{-1} is due to the stretching of the V-O-V bond. Besides these bands, the Raman bands at 409 and 290 cm^{-1} are ascribed to the bending vibrations of the V=O [78, 79, 93].

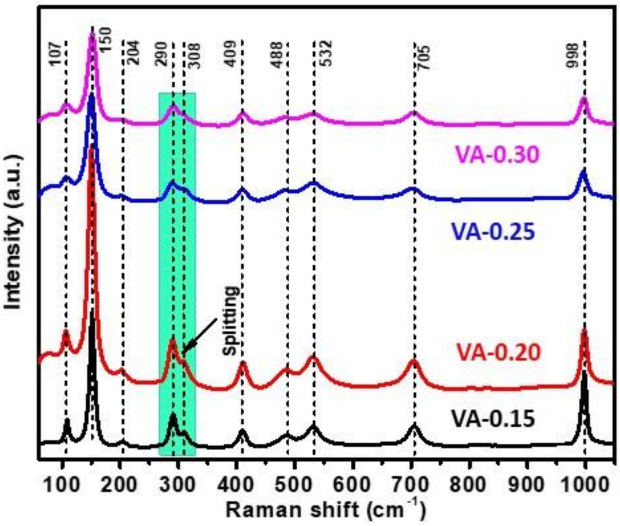

Fig. 4.34 Raman spectra of the Ti doped V_2O_5 samples.

However, the Raman band at 290 cm^{-1} shows splitting into 308 cm^{-1}, which is due to the stretching mode of the V-O-V bond. Raman band at 204 cm^{-1} occurs due to the [VO_5]-[VO_5] vibrations and strongly supports a layer structure of vanadium oxide in the present samples. The Raman bands at 107 and 150 cm^{-1} are associated with the vibration in a V-O-V atomic chain. The intensity range of the band (150 cm^{-1}) indicates long-range order in V_2O_5 planes [78, 93]. Therefore, the presence of all the vibrations as presented in Fig. 4.33 and 4.34 recommends the structural changes on the doping of TiO_2 in place of V_2O_5 as also supported by X-ray diffraction and FTIR results and which may affect the conduction phenomenon in the present samples.

4.4.5 Optical properties

The optical diffused reflectance spectra (DRS) of the $V_{2-x}Ti_xO_{5-\delta}$ (x=0.15-0.30) samples are shown in Fig. 4.35 (a). It is observed that the reflectance decreases from 14.5-12.3% with an increase in the doping of Ti on the cost of V_2O_5. The sample with the lowest doping of Ti (VT0.15) shows the highest reflectance (14.5%) whereas the sample with the highest doping of Ti (VT0.30) exhibits the minimum reflectance (12.3%). The decrement in the % reflectance can be due to the optical phonon confinement, which is accompanying light entrapment properties of the samples [17]. The samples absorb only visible light around a wavelength of

560 nm. However, this absorption edge/reflectance onset exhibits red shifting on the doping of Ti in place of V_2O_5. The shifting in the absorption edge also satisfies the molar volume trend (Table 1), which leads to an increase in free volume on Ti doing in place of V_2O_5. Also, the absorption edges are sharply defined (Fig. 4.35 (a).), which is associated with the crystalline nature of the samples which is also supported by the XRD patterns [81]. These absorption edges play a vital role in obtaining the optical band gaps of the samples.

The absorption edge and optical band gap have an inverse relationship to each other. The optical band gaps of the samples are obtained from reflectance spectra using the following equations [31].

$$F(R) = K/S = (1-R)^2/2R = \alpha \tag{4.15}$$

$$(F(R)h\nu) = k(h\nu - E_g)^n \tag{4.16}$$

where, $F(R)$ is the Kubelka-Munk function, K is the absorption coefficient, S is the scattering coefficient, k is the proportionality constant, E_g is the optical band gap and $h\nu$ is the incident photon energy. The exponent 'n' is subjected to the transitions such as where n=1/2, 2, 3/2 and 3 allowed direct ($n = 1/2$), allowed indirect ($n = 2$), forbidden direct ($n = 3/2$), and forbidden indirect ($n = 3$) transition [34].

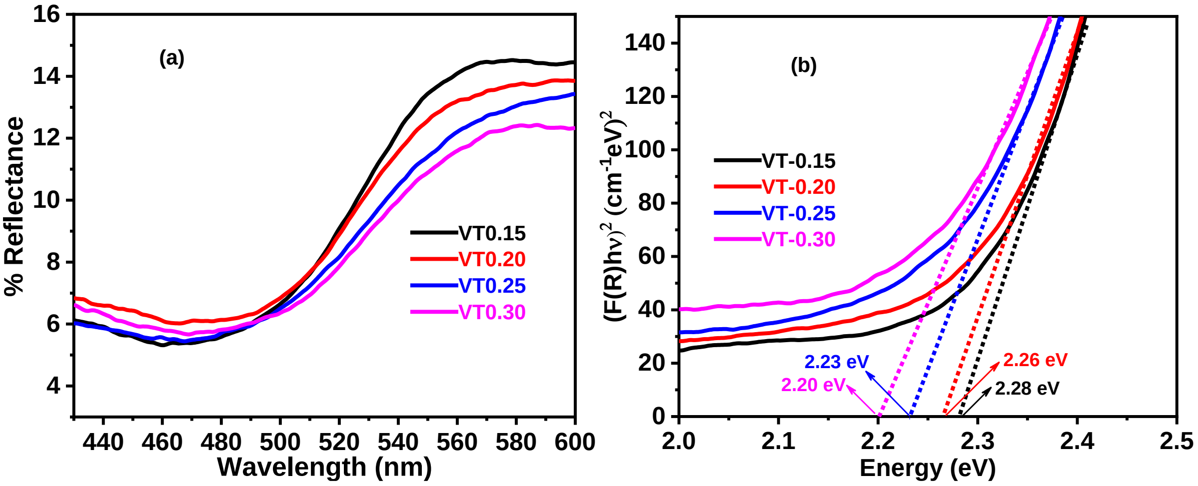

Fig. 4.35 (a) Diffused reflectance spectra and (b) Tauc plots to find out the optical band gap of the Ti doped V_2O_5 samples.

To obtain the direct optical band gaps of the samples, the straight-line portion of Tauc plots ($(F(R)h\nu)^2$ vs $h\nu$) is extrapolated to the x-axis at y=0 as shown in Fig. 4.35 (b). The band tailing parameter i.e. Urbach energy (E_U) is obtained using the equation $\alpha(\nu) = \beta\exp\,(h\nu)/E_U$. The Urbach energy is evaluated by taking the inverse of the slope of the linear portion from *lnF(R)* vs $h\nu$. The obtained optical band gap and Urbach energy values are depicted in Table 4.10. It is observed that the optical band gap decreases from 2.28-2.20 eV with an increase in Ti doping on the cost of V_2O_5. While E_U increases from 0.52-0.59 eV as the doping of Ti increases. The same trend in optical band gap i.e. decreasing (2.22 to 2.08 eV) and Urbach energy i.e. increasing (0.31 to 0.41 eV) is also observed in Li doped vanadium oxide systems [85]. The decreasing trend of the optical band can be explained by the density functional theory (DFT) calculations. According to the DFT studies, the delocalization of 3d states of V contributes to the formation of impurity/defects energy levels just below the conduction band edge of Ti by hybridizing with 3d states of Ti, which leads to the formation of a new conduction band at lower energy, resulting lower band gap [93]. In addition, the electrons from the valance band can be excited at lower energy to generated new energy levels (defects) due to the Ti doping into V_2O_5. Apart from this, the observed redshift in the absorption edge of the samples is also clearly understandable here.

Table 4.10 Optical and conductivity parameters of the $V_{2-x}Ti_xO_{5-\delta}$ (x=0.15-0.30) samples.

Sample ID	E_g (eV)	E_u (eV)	σ_{dc} at 400 °C (Sm^{-1})	E_a (eV)	Temperature range (°C)
VT-0.15	2.28	0.052	0.34	0.14	50-150
				0.27	150-400
VT-0.20	2.26	0.055	0.35	0.10	50-150
				0.22	150-400
VT-0.25	2.23	0.058	0.41	0.14	50-150
				0.27	150-400
VT-0.30	2.20	0.059	1.12	0.16	50-150
				0.23	150-400

E_U is associated with the width of the tail of localized states in the E_g and gives a measure of disorder in the samples. The compositional trend in E_U (increases) is consistent with the corresponding trend in E_g (decreases), which indicates that the defects increase with an increase in Ti doping on the cost of V_2O_5. In other word, the decreasing band gap enhances the electron-hole (e-h) recombination probabilities [31].

4.4.6 Thermal properties

Fig. 4.36 (a) represents the DTA thermographs of the $V_{2-x}Ti_xO_{5-\delta}$ (x=0.15-0.30) samples in the temperature range of 40-800 °C with a heating rate of 10 °C. It is observed that all the samples exhibit a broad endothermic peak at ~ 670 °C temperatures (Fig. 4.36 (a)). It is associated with the melting point of the orthorhombic V_2O_5 phase as confirmed by the XRD analysis of these samples. It is also observed that the endothermic peak marginally shifts to a lower temperature from ~677-670 °C with increasing Ti content as shown in the inset of Fig. 4.36 (a). It suggests that the thermal stability of the samples decreases with the increasing doping of Ti. In addition, to investigate the thermal stability of the $V_{2-x}Ti_xO_{5-\delta}$ ((x=0.15-0.30)) samples, TGA thermographs are taken and shown in Fig. 4.36 (b). From Fig. 4.36 (b), there is a weight loss ~0.6 % in the temperature range of ~25-400 °C. This weight loss can be considered in two steps as marked I (~25-125 °C) and II (~120-375 °C) in the TGA graph. The I step is associated with the departure of adsorbed species and evaporation of moisture.

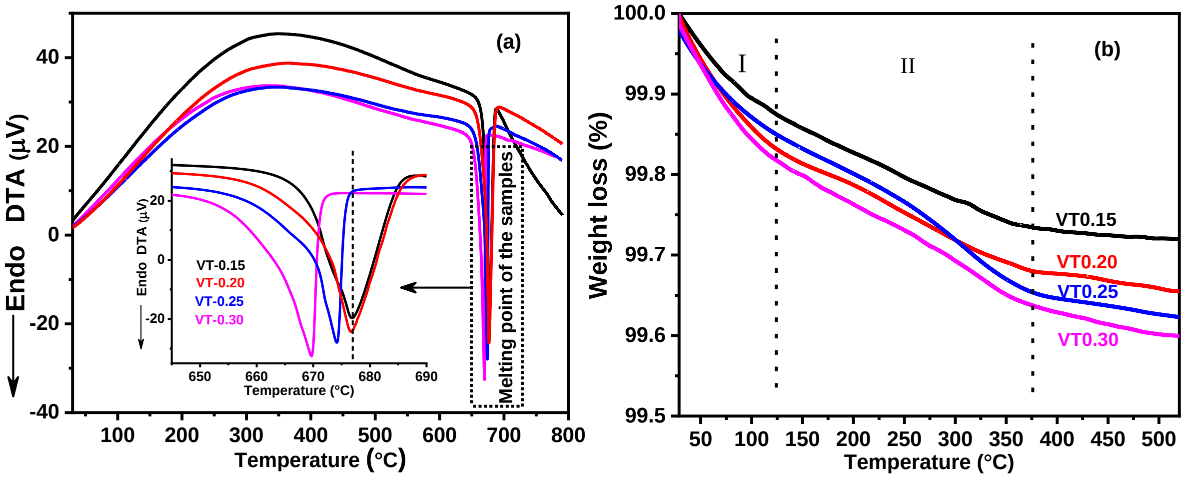

Fig. 4.36 (a) DTA thermographs; and (b) thermal stability behavior of Ti doped V_2O_5 systems measured at 10 °C heating rate.

The II step is assigned to the reduction of the vanadium or titanium state from V^{5+} to V^{4+}/V^{3+}, which can be written as follows [1].

$$2V^{5+} + O^{2-} \rightarrow 2V^{4+} + O_2 \uparrow \tag{4.17}$$

The variation in the oxidation state of vanadium oxide was expected because vanadium oxide has different oxidation states (V^{+3}, V^{+4} and V^{5+} etc.). Thermal stability of the samples decreases (mass loss increases) as the doping concentration of TiO_2 increases. VT0.15 sample exhibits the highest thermal stability whereas the VT0.30 sample shows the lowest thermal stability.

4.4.7 XPS analysis

XPS has been performed on selected samples (VM0.15 and VM0.30) to confirm the presence of oxidation states of vanadium. Fig. 4.37 shows the XPS spectra of VT-0.15 and VT-0.30 samples. For the high content of Ti-doped sample (VT-0.30), the two peaks are observed at the binding energies of 523.80 and 525.3 eV, which are attributed to V^{4+} and V^{5+} states, respectively, as shown in Fig. 4.37 (b).

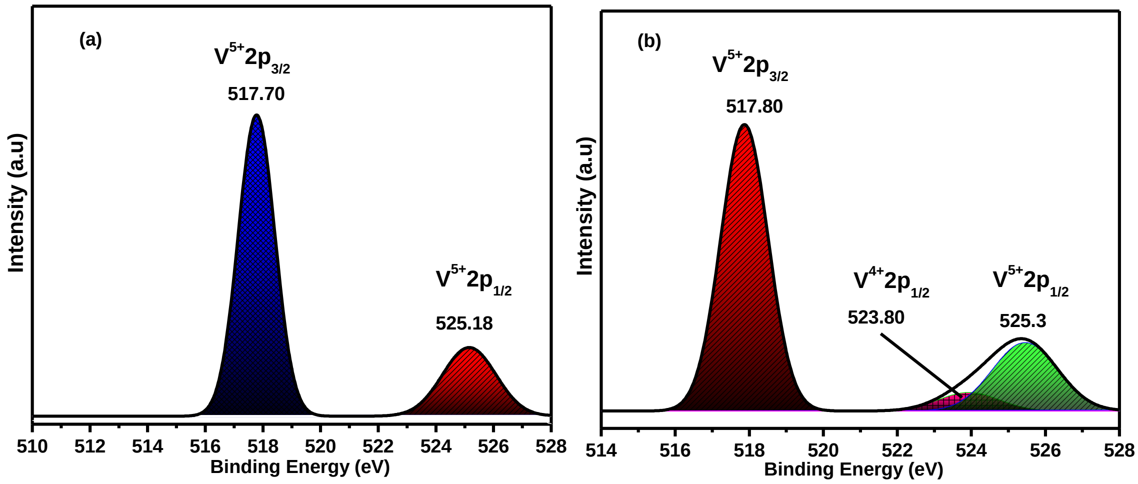

Fig. 4.37 XPS spectra of (a) VT-0.15 and (b) VT-0.30 samples. A survey spectrum of V2p of TiO_2-doped V_2O_5.

It is obvious that the V lies in V^{5+} state mainly in VT-0.15 sample. On the other hand, the higher concentration of TiO_2 supports in the reduction of vanadium states from V^{5+} to V^{4+}. In view of this, the presence V^{4+} state in the V_2O_5 matrix can be enhanced the conductivity of the present samples due to polaron hopping from V^{5+} to V^{4+} and creation of oxygen vacancies [94].

As the V^{4+} sites increases in the samples the hopping probability also increases in doped samples. The XPS measurement confirms that the dopants in the present samples is converted V^{5+} to V^{4+} states.

4.4.8 Conductivity studies

Fig. 4.38 represents the variation of conductivity (σ_{ac}) with frequency for $V_{2-x}Ti_xO_{5-\delta}$ (x=0.15-0.30) samples at discrete temperatures in the range of 50-400 ºC. It is observed that the AC conductivity behavior of all the samples with frequency and temperature is qualitatively similar. The conductivity is almost static up to ~1000 Hz frequency i.e. called DC conductivity (plateau region) and then increases with increasing frequency (dispersion region) [1, 95]. The plateau region is related to the randomness of ionic diffusion, caused by long-range order transport and substantial mobile ions diffusion on the application of the AC field. On the other hand, dispersion region (high frequency) supports conductivity relaxation phenomena with following Jonscher's power law [1, 11, 24].

$$\sigma_{ac}(\omega, T) = \sigma_{dc}(T) + A\omega^{s} \tag{4.18}$$

Here, ω is the angular frequency, A is the temperature-dependent constant and s is the temperature and frequency-dependent exponent (lies between 0-1). The DC conductivity values of the samples were extracted by extrapolating σ_{ac} at a minimum frequency (Fig. 4.38) and the obtained values are listed in Table 4.10. It is observed that the DC conductivity follows the Arrhenius equation [30].

$$\sigma_{dc} = \sigma_{o} \exp\left(-E_a/k_B T\right) \tag{4.19}$$

Here, σ_o is a pre-exponential factor, k_B is the Boltzmann's constant, E_a is the activation energy of the conduction and T is the absolute temperature. For in-depth analysis of the conduction mechanism in the samples, the temperature-dependent conductivity is examined over the temperature range 100-400°C. Arrhenius plots ($\frac{1000}{\mathrm{T}}$ vs $ln\,\sigma_{dc}$) are used to obtain the activation energy of the DC conduction as shown in Fig. 4.39.

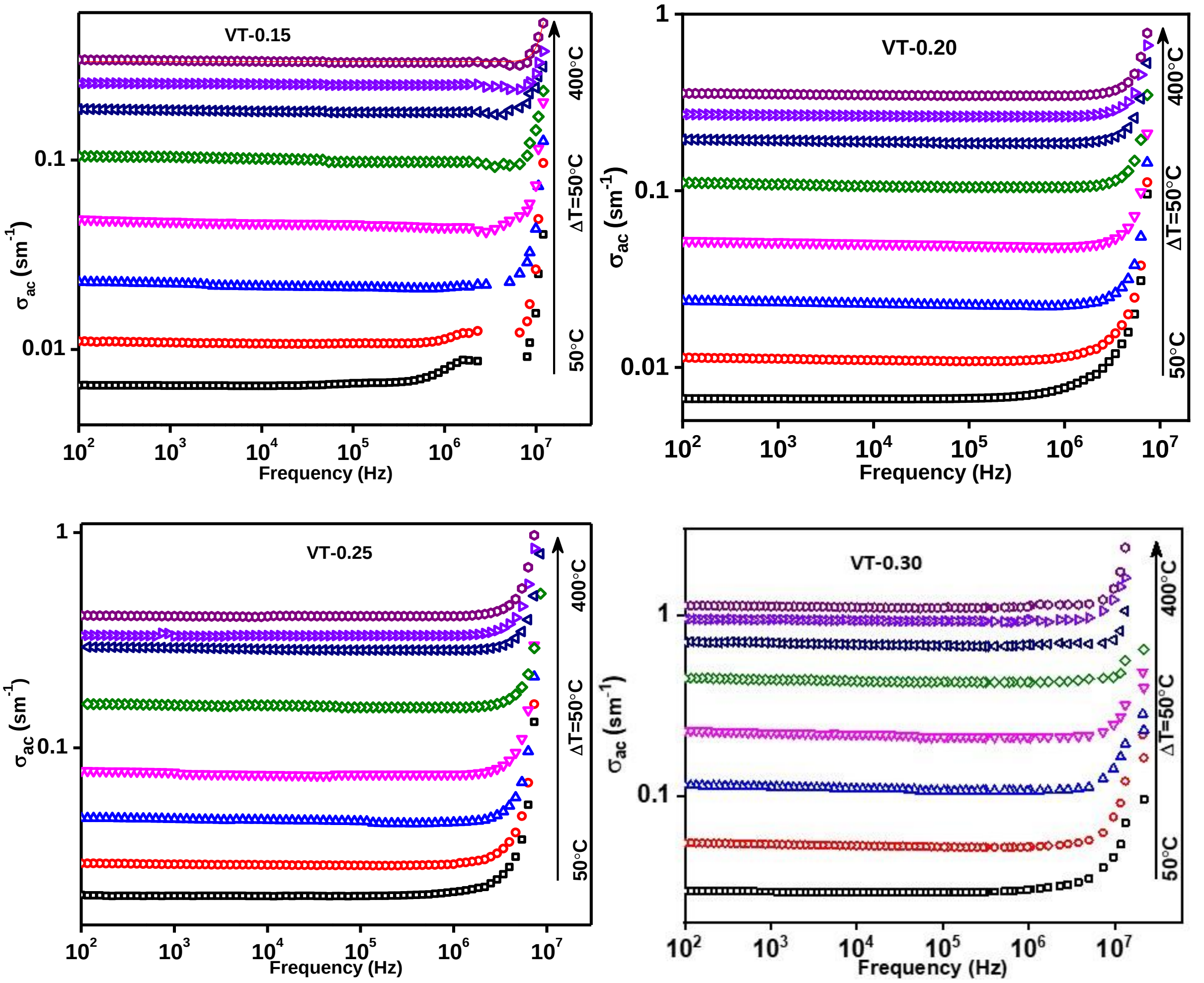

Fig. 4.38 Change in AC conductivity with frequency and temperature for Ti doped V_2O_5 samples.

It is observed that the σ_{dc} increases as temperature increases (50-400 °C) which is associated with the semiconductor character of the present samples [1, 95]. This semiconductor nature is also seen in MgO doped V_2O_5 systems [1]. The conductivity governs by the concentration of the charge carriers/mobile ions and mobility as well. The mobility of the charge carriers or mobile ions increases as temperature increases, resulting in increased conductivity as observed in the present samples. In addition, the excitation of electrons from the valence band to the conduction band also increases with increasing temperature, leading to an increase in the conductivity of the samples. The DC conductivity of the samples increases from 0.34 to 1.12 Sm^{-1} at 400 °C with increasing content of Ti as shown in Table 4.10. In previous study, the DC conductivity lies in the range of 0.11 to 6.7×10^{-4} Sm^{-1} in Mg doped V_2O_5 systems [1]. In vanadium-based materials, the conduction mechanism depends on the small polaron hopping (SPH) between V^{4+} and V^{5+} states [1].

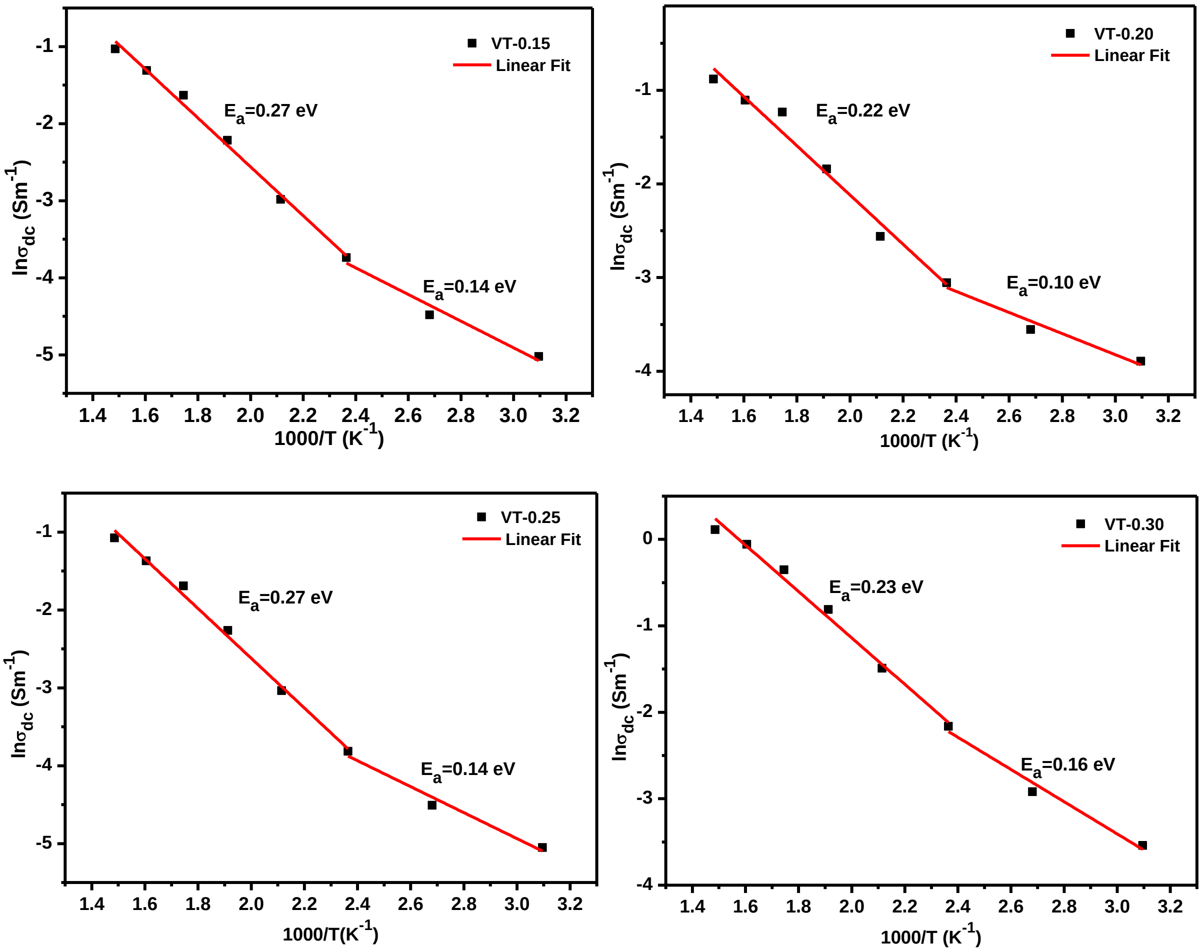

Fig. 4.39 Variation in DC conductivity with inverse temperature for VT-0.15, VT-0.20, VT-0.25 and VT-0.30 samples.

The SPH is governed by the mobility and concentration of the charge carriers. In the present case, the structure of the samples becomes more open as VO_5 changes into VO_4 unit on the doping of Ti^{4+}, leading to an increase in oxygen vacancies in the system. The increase in oxygen vacancies encourages the polaron hopping between V^{4+} and V^{5+} states, consequently, an increase in the conductivity [93, 33, 96]. In addition, a decreasing trend of the optical band gap and physical parameters (density and inter-ionic distance) also supports the increasing trend of conductivity with Ti doping into V_2O_5. The inverse temperature DC conductivity plots i.e. Arrhenius plots clearly show the two slopes in all the samples as shown in Fig 4.39. Both slopes are least square fitted (Arrhenius equation) for all the samples and obtained activation energy values of the DC conduction for different temperature range are given in Table 4.10. The slope change or transition temperature in Arrhenius plots represents the change in conduction phenomena. The low temperature conduction is known as extrinsic conduction whereas high temperature conduction is associated with the intrinsic conduction phenomena. The low temperature range (50-150 ºC) activation energies are found in the range of 0.14 to 0.16 eV whereas high temperature range (150-400 ºC) activation energy lies in the range of 0.27 to 0.23 eV. The high temperature activation energy values (150-400 ºC) decrease as the doping of Ti increases except for VT-0.25 sample. This decrement in activation energy values also supports the increasing trend of DC conductivity values with the doping of Ti in place of V_2O_5 as discussed above.

4.5 Interaction study

Interaction study between electrolyte and interconnect is important due to the inter-diffusion among various components, is taken place during SOFC operation. Thus, some selected samples have been used to check the chemical compatibility with AISI 430 steel as interconnect material. Based on the study as carried out on the doped V_2O_5 with different dopants samples, Mg doped V_2O_5 samples were selected due to their better conductivity at low temperature, thermal and other properties as compared to other doped samples. Moreover, Mg doped V_2O_5 was also formed glass.

The selection of steel 430 have been done based on their suitability as interconnect material for intermediate temperature solid oxide fuel cell.

4.5.1 $V_{1.80}Mg_{0.20}O_{5-\delta}$ (VM-0.20)/AISI 430 steel

The obtained interfaces between VM-0.20 glass sample and AISI 430 steel after heat treatment of 1 h, 10 h and 100 h at 620 ˚C are shown in Fig. 4.40. The smooth interface with good adherence has been formed between VM-0.20 glass sample and AISI 430 steel interconnect after heat treatment of 1 h, 10 h and 100 h for 620 ˚C as clearly seen in Fig.

4.40. However, at 1 h, glass sample shows some pits. On the other hand, at 100 h, the VM-0.20 glass sample shows highest crystallization as compared to heat treatment for 1h and 10 h as clearly seen in the Fig. 4.40. The X-ray dot mapping (Fig. 4.41) clearly shows that all the elements have been diffused from AISI steel 430 to glass and vice versa. Maximum diffusion of silicon is observed from AISI 430 steel to glass followed by Cr and Fe.

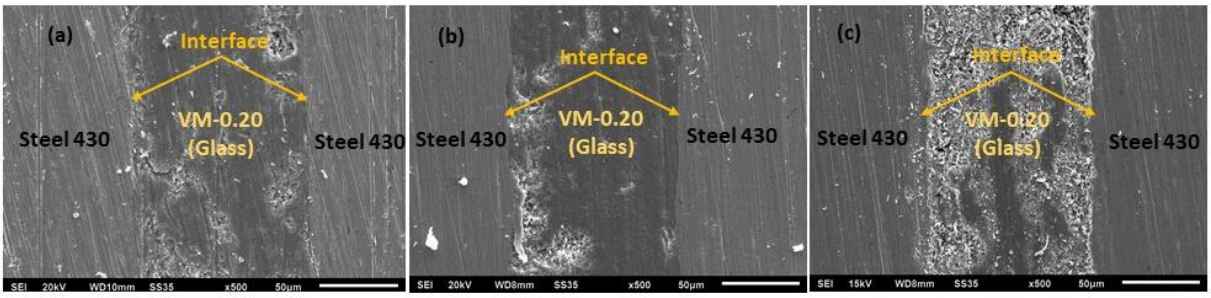

Fig. 4.40 Interfaces between steel 420 and VM-0.20 glass heat treated at 620 ˚C for (a) 1h (b) 10 h (c) 100 h.

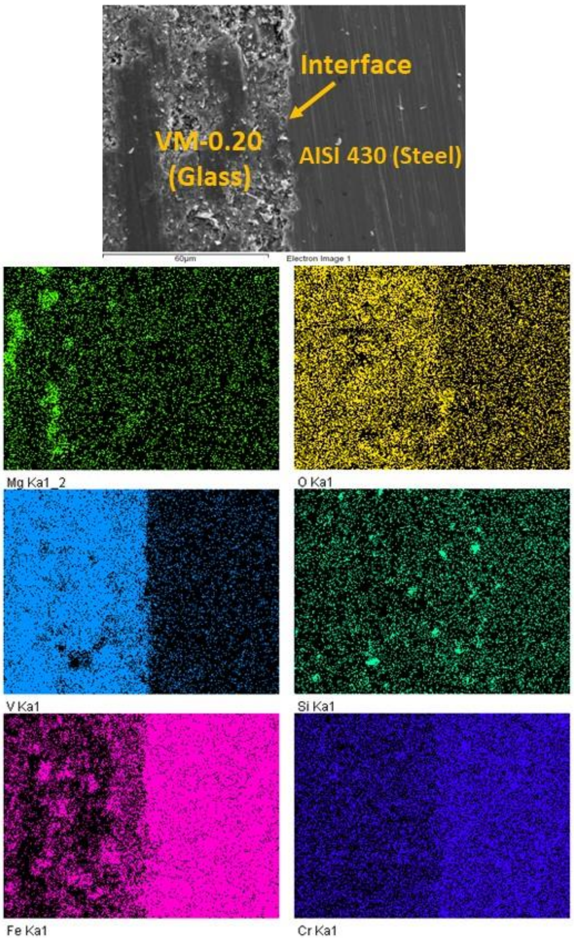

Fig. 4.41 SEM and X-ray dot mapping of VM-0.20/AISI 430 steel after 100 h heat treated at 620 ˚C.

The elements from the VM-0.20 glass side have also been diffused into AISI 430 steel interconnect side. On the other hand, Mg is diffused maximum in AISI 430 steel followed by O and V. The minimum diffusion has been ocurred of V element from VM-0.20 glass side into AISI 430 steel interconnecy as compared to other elements. Obviously, vanadium is having high charge and act as glass former in the sample.

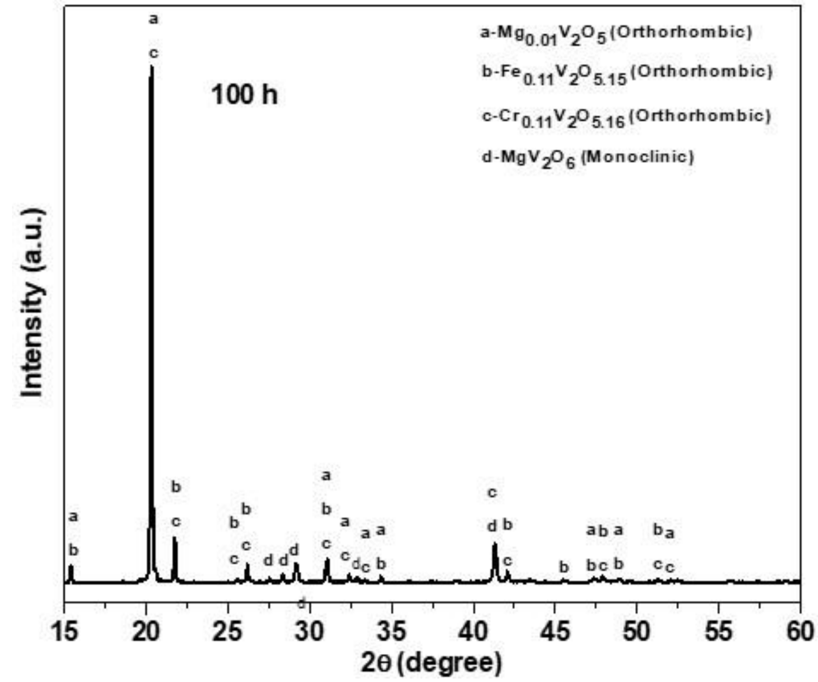

Fig. 4.42 XRD patterns of the VM-0.20/AISI 430 steel after 100 h heat treatment for 620 ˚C.

The XRD patterns of VM-0.20/AISI 430 steel system after 100 h and heat treated at 620 ˚C is given in Fig. 4.42 to confirm the crystalline phases formation during interaction study. Two major phases and two minor phases are formed after interaction at 620 ˚C for 100 h. The formed major phases are $Mg_{0.01}V_2O_5$ (ICDD No.:01-089-0610) and $Cr_{0.11}V_2O_{5.16}$ (ICDD No.:01-089-1323). On the other hand, the formed minor phases are $Fe_{0.11}V_2O_{5.15}$ (ICDD No.:01-082-1871) and MgV_2O_6 (ICDD No.:00-045-1050).

4.5.2 $V_{1.75}Mg_{0.25}O_{5-\delta}$ (VM-0.25)/AISI 430 steel

The obtained interfaces between VM-0.25 glass sample and AISI 430 steel after heat treatment of 1 h, 10 h and 100 h at 620 ˚C are shown in Fig. 4.43. The interface has been occurred between VM-0.25 glass and AISI 430 steel interconnect as shown in Fig. 4.43.

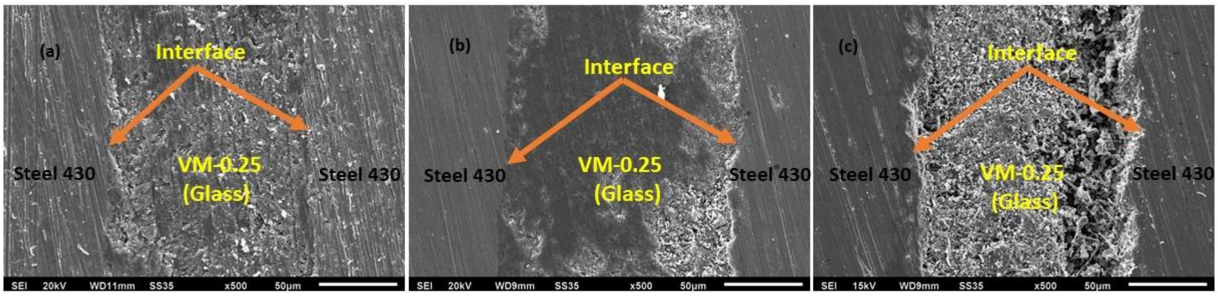

Fig. 4.43 Interfaces between AISI 430 steel and VM-0.25 glass heat treated at 620 ˚C for (a) 1h (b) 10 h (c) 100 h.

The glass sample heat treated for 10 h shows smooth interface with good adherence as compared heat treated 100 h. As heat treatment duration increases the crystallization also increases as seen in the Fig. 4.43. The VM-0.25 glass sample with AISI 430 steel interconnect shows some delamination at the interface which may be due to the coefficient of thermal expansion mismatch between VM-0.25 glass sample and AISI 430 steel. The diffusion couple of VM-0.25 and AISI 430 steel is formed better interface and adherence as compared to diffusion couple of VM-0.20 and AISI 430 steel interconnect. The X-ray dot mapping (Fig. 4.44) clearly shows the diffusion into each other side of all the elements. The maximum diffusion of silicon occurs followed by Fe and Cr from AISI 430 steel side into VM-0.25 glass side. On the other hand, the maximum diffusion occurs of Mg followed by O and V from VM-0.25 glass side into AISI 430 steel interconnect side. The VM-0.25 glass sample shows higher diffusion into into each other of all the elements as compared to VM-0.20 glass sample heat traeted for 620 ˚C at 100 C. In selected samples VM-0.20 is better than VM-0.25 sample. The XRD patterns of VM-0.25/AISI 430 steel system after 100 h and heat treated at 620 ˚C are shown in Fig. 4.45. Similarly, as observed in the interaction between AISI 430 steel and $V_{1.80}Mg_{0.20}O_{5-\delta}$, four crystalline phases are observed. The formed major phases are $Mg_{0.01}V_2O_5$ (ICDD No.:01-089-0610) and $Cr_{0.11}V_2O_{5.16}$ (ICDD No.:01-089-1323). While the formed minor phases are $Fe_{0.11}V_2O_{5.15}$ (ICDD No.:01-082-1871) and MgV_2O_6 (ICDD No.:00-045-1050). However, this diffusion couple shows more crystallization as compared to the VM-0.20/AISI 430 steel same time duration and heat treatment temperature.

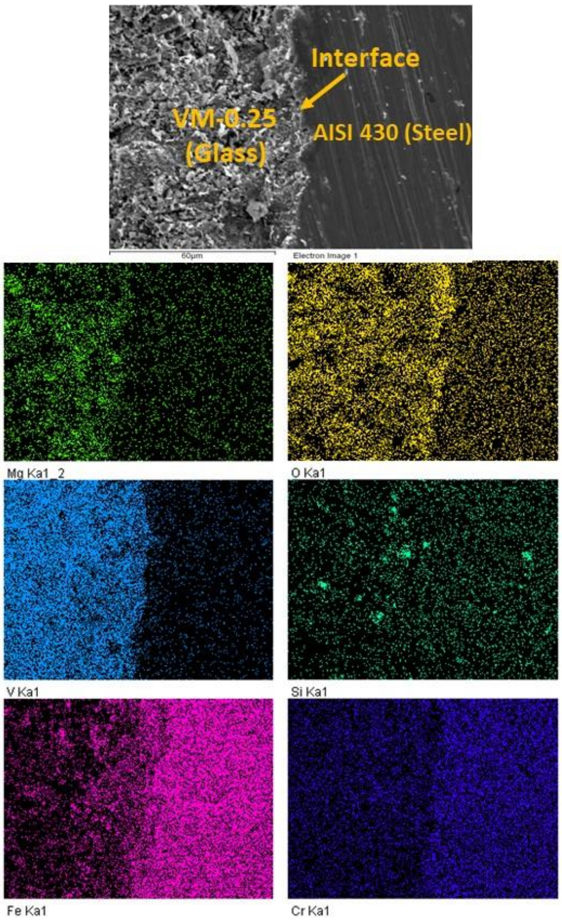

Fig. 4.44 SEM and X-ray dot mapping of VM-0.25/AISI 430 steel after 100 h heat treated at 620 ˚C.

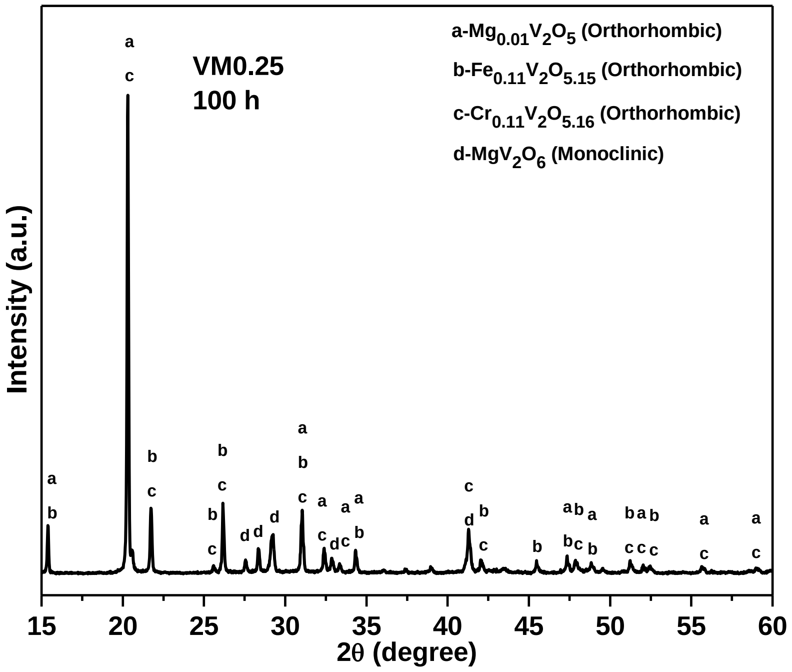

Fig. 4.45 XRD patterns of the VM-0.25/AISI 430 steel after 100 h heat treatment at 620 ˚C.

It is clearly seen more intense XRD peak with lower full width at half maxima (FWHM) and more resolved peaks than the VM-0.20/AISI 430 steel system. Overall, both the diffusion couple exhibit good diffusion of Cr and Fe from steel side. However, the diffusion of Cr is higher than Fe whereas Mg is diffused from glass to steel.

References

1. S. Khan, K. Singh, Ceram. Int. 45 (2019) 695.
2. M.G. Moustafa, M.Y. Hassaan, J. Alloy. Compd. 710 (2017) 312.
3. A. Tsuzuki, K. Kani, K. Watari, Y. Torii, J. Mater. Sci. 28 (1993) 4063.
4. P.M. Shirage, A.K. Rana, Y. Kumar, S. Sen, S.G. Leonardi, G. Nerib, RSC Adv. 6 (2016) 82733.
5. K. Jeyalakshmi, S. Vijayakumar, S. Nagamuthu, G. Muralidharan, Mater. Res. Bull., 48 (2013) 760.
6. S. Mandal, A. Ghosh, Phys. Rev. B 48 (1993) 9388.
7. L.S. Rao, M.S. Reddy, M.R. Reddy, N. Veeraiah, J. Alloy. Compd. 464 (2008) 472.
8. R. Iordanova, Y. Dimitriev, V. Dimitrov, D. Klissurski, J. Non-Cryst. Solids 167 (1994) 74.
9. S. Ibrahim, M.A. Marzouk, G.M.E. Komy, Silicon 9 (2017) 403.
10. M. Vijayakumar, S. Selvasekarapandian, R. Kesavamoorthy, K. Nakamura, T. Kanashiro, Mat. Lett. 57 (2003) 3618.
11. Y. Dimitriev, V. Dimitrov, M. Arnaudov, D. Topalov, J. Non-Cryst. Solids, 57 (1983) 147.
12. G. Padmaja, P. Kistaiah, J. Phys. Chem. A 113 (2009) 2397.
13. X. Zhou, G. Wu, J. Wu, H. Yang, J. Wang, G. Gao, Phys. Chem. Chem. Phys. 16 (2014) 3973.
14. S. Lee, H.M. Cheong, M.J. Seong, P. Liu, C.E. Tracy, A. Mascarenhas, J.R. Pitts, S.K. Deb, Solid State Ionics 165 (2003) 111.
15. D. Sethi, N. Jada, A. Tiwari, S. Ramasamy, T. Dash, S. Pandey, J. Photoch. Photobio. B 144 (2015) 68.
16. S. Zhan, G. Chen, D. Liu, A. Li, C. Wang, Y. Wei, J. Alloy. Compd. 479 (2009) 652.
17. A. Ghosh, R.R. Juluri, P. Guha, R. Sathyavathi, A. Dash, B.K. Jena, P.V. Satyam, J. Phys. D: Appl. Phys. 48 (2015) 055303.
18. S.H. Lee, G.E.J. Jr, C.E. Duty, J. Xu, Appl. Phys. Lett. 99, (2011) 153113.
19. S. Khan, G. Kaur, K. Singh, Ceram. Int. 43 (2017) 722.
20. S.K. Kumar, C.S. Menon, phys. stat. sol. (a) 153 (1996) 439.
21. J.C.S. Kumari, S.T. Nishanthi, J. Dhanalakshmi, M. Ahila, D.P. Padiyan, Appl. Surf. Sci. 44, (2018) 530.
22. S. Hui, A. Petric, Solid State Ionics 143 (2001) 275.

23. Z. Cheng, S. Zha, L. Aguilar, M. Liu, Solid State Ionics 176 (2005) 1921.
24. A. Yadav, M.S. Dahiya, P. Narwal, A. Hooda, A. Agarwal, S. Khasa, Solid State Ionics 312 (2017) 21.
25. S. Thakur, O.P. Pandey, K. Singh, Ceram. Int. 39 (2013) 6165.
26. T.F. Khoon, J. Hassan, Z.A. Wahab, R.S. Azis, Results Phys. 6 (2016) 420.
27. A. Al-Hajry, A. Al-Shahrani, M.M. El-Desoky, Mater. Chem. Phys. 95 (2006) 300.
28. N. Tashtousha, A.M. Qudaha, M.M. El-Desoky, J. Phys. Chem. Solids 68 (2007) 1926.
29. A. Dutta, T.P. Sinha, P. Jena, S. Adak, J. Non-Cryst. Solids 354 (2008) 3952.
30. N. Kaur, G. Kaur, S. Khan, K. Singh, Ionics 24 (2017) 2343.
31. S. Jaidka, S. Khan, K. Singh, Physica B 550 (2018) 189.
32. R. Kant, K. Singh, O.P. Pandey, Int. J. Hydrogen Energ. 33 (2008) 455.
33. S. Gupta, K. Singh, Solid State Ionics 278 (2015) 233.
34. M.G. Moustafa, Ceram. Int._42 (2016) 17723.
35. P. Jha, K. Singh, Silicon 3 (2016) 437.
36. A. Miyauchi, T.H. Okabe, Mater. Trans. 51 (2010) 1102.
37. R. Iordanova, Y. Dimitriev, V. Dimitrov, S. Kassabov, D. Klissurski, J. Non-Cryst. Solids 204 (1996) 141.
38. R. Iordanova, V. Dimitriev, V. Dimitrov, D. Klissurski, J. Non-Cryst. Solids 167 (1994) 74.
39. S. Sen, A. Ghosh, J. Mater. Res. 15 (2000) 995.
40. G.L. Flower, G.S. Baskaran, N.K. Mohan, N. Veeraiah, Mater. Chem. Phys. 100 (2006) 211.
41. P. Jha, S.S. Danewalia, K. Singh, J. Therm. Anal. Calorim. 128 (2017) 745.
42. A. Alhajry, A.A. Shahrani, M.M.E. Desoky, Mater. Chem. Phys. 95 (2006) 300.
43. S. Sen, A. Ghosh, J. Non-Cryst. Solids 258 (1999) 29.
44. D. Souri, Measurement 44 (2011) 1904.
45. T. Kumatso, T. Noguchi, Y. Benino, J. Non-Cryst. Solids 222 (1997) 206.
46. R.V. Barde, S.A.Waghuley, Ceram. Int. 39 (2013) 6303.
47. A. Gupta, G. Singla, O.P. Pandey, Ceram. Int. 42 (2016) 13024.

48. A. Yadava, M.S. Dahiyab, P. Narwala, A. Hoodaa, A. Agarwalc, S. Khasa, Solid State Ionics 312 (2017) 21.

49. S. Rani, S. Sanghi, N. Ahlawat, A. Agarwal, J. Alloys Compd. 619 (2015) 659.

50. R.B. Rao, N.O. Gopal, N. Veeraiah, J. Alloys Compd. 368 (2014) 25.

51. T. Sankarapp, M.P. Kumar, G.B. Devidas, N. Nagaraja, R. Ramakrishnareddy, J. Mol. Struct. 889 (2008) 308.

52. A. Yadav, S. Khasa, A. Hooda, M.S. Dahiya, A. Agarwal, P. Chand, Spectrochim. Acta A 157 (2016) 129.

53. A.K. Jonscher, Nature 267 (1977) 673.

54. S. Seethalakshmia, B. Subramanian, A. Bendavid, A.K.N. Kumar, Ceram. Int. 43 (2017) 3202.

55. B. Yuan, X. He, L. Chen, W. Wang, T. Cheng, E. Liang, Ceram. Int. 44 (2018) 21621.

56. S. Sen, A. Ghosh, J. Appl. Phys. 87 (2000) 3355.

57. I.G. Austin, N.F. Mott, Adv. Phys. 18 (1969) 41.

58. N.F. Mott, J. Non-Cryst Solids 1 (1968) 1.

59. R. Kant, K. Singh, O.P. Pandey, Ionics 16 (2010) 277.

60. W.D. Callister, Materials Science and Engineering, 2nd edn. New Delhi, India: Wiley Pvt. Ltd.; 2014.

61. M.M.E. Desoky, J. Non-cryst Solids 351 (2005) 3139.

62. M.M.E. Desoky, J. Mater. Sci. Mater. Electron 14 (2003) 215.

63. K. Sega, Y. Kuroda, H.D.C. Sakta, J. Mater. Sci. 33 (1998) 1303.

64. H. Sakata, K. Sega, B.K. Chaudhuri, Phys. Rev. B 50 (1999) 3230.

65. P. Sippel, P. Lunkenheimer, S. Krohns, E. Thoms, A. Loidl, Sci. Rep. 5 (2015) 13922(1-8).

66. W. Xu, E.I. Cooper, C.A. Angell, Phys. Rev. B 107 (2003) 6170.

67. P.J. Griffin, A.L. Agapov, A.P. Sakalov, Phys. Rev. E 86 (2012) 021508(1-9).

68. E. Thomas, P. Sippel, D. Reuter, M. Weib, A. Loidl, S. Krohns, Sci. Rep. 7 (2017) 7663(1-9).

69. A.A. Bahgat, M.G. Moustafa, E.E. Shaisha, J. Mater. Sci. Technol. 29 (2013) 1166.
70. S. Sindhu, S. Sanghi, A. Agarwal, V.P. Seth, N. Kishore, Mater. Chem. Phys. 90 (2005) 83.
71. T.F. Yia, J. Shub, Y.R. Zhua, X.D. Zhuc, C.B. Yuea, A.N. Zhoua, R.S. Zhua, Electrochimica Acta 54 (2009) 7464.
72. S. Vives, E. Gaffet, C. Meunier, Mater. Sci. Eng. A 366 (2004) 229.
73. K. Jeyalakshmi, S. Vijayakumar, S. Nagamuthu, G. Muralidharan, Mater. Res. Bull. 48 (013) 760.
74. D. Sethi, N. Jada, A. Tiwari, S. Ramasam, T. Dash, S. Pandey, J. photoch. photobio. B 144 (2015) 68.
75. M. Farahmandjou, N. Abaeiyan, J. Nanomed. Res. 5 (2017) 00103 (1-4).
76. M. Wu, X. Zhang, S. Gao, X. Cheng, Z. Rong, Y. Xu. H. Zhaoa, L. Huo, Cryst. Eng. Comm. 15 (2013) 10123.
77. R.B. Hadjean, E. Raekelboom, J.P.P. Ramos, Chem. Mater. 18 (2006) 3548.
78. X. Wu, F. Lai, L. Lin, Y. Li, L. Lin, Y. Qu, Z. Huang, Appl. Surf. Sci. 255 (2008) 2840.
79. D.S. Bhaskaram, R. Cheruku, G. Govindaraj, J. Mater. Sci.: Mater. Electron. 27 (2016) 10855.
80. P.P. Pawar, S.R. Munishwar, R.S. Gedam, J. Alloy. Compd. 660 (2016) 347.
81. P.P. Pawar, S.R. Munishwar, S. Gautam, R.S. Gedam, J. Lumin. 183 (2017) 79.
82. A.E.M. Gomez, J. Sacanell, C. Huck-Iriart, C.P. Ramos, A.L. Soldati, S.J.A. Figueroa, M.H. Tabacniks, M.C.A. FantinI, A.F. Craievich, D.G. Lamas, J. Alloy. Compd. 817 (2020) 153250.
83. R. Das, T. Sarkar, K. Mandal, J. Phys. D: Appl. Phys. 45 (2012) 455002.
84. M.S. Dahiyaa, S. Dalal S. Khasa, J. Non-Cryst. Solids 485 (2018) 24.
85. S. Khan, K. Singh, Sci. Rep. 10 (2020) (1089) (1-11).
86. I. Abraham, F. Krok, J. Nelstrop. Solid State Ionics 90 (1996) 57.
87. N. Shash, Ionics 19 (2013) 1825.
88. A. Ghosh, B.K. Chaudhary, J. Non-Cryst. Solids 103 (1988) 83.
89. R.V. Barde, K.R. Nemade, S.A. Waghuley, J. As. Ceram. Soc. 3 (2015) 116.
90. T.F. Yi, J. Shu, Y.R. Jhu, X.D. Zhu, C.B. Yue, A.N. Jhou, R.S. Jhu, Electrochimica acta, 54 (2009) 7464.
91. K. Jeyalakshmi, S. Vijayakumar, S. Nagamuthu, G. Muralidharan, Mater. Res. Bull. 48 (2013) 760.
92. Y. Dimitriev, V. Dimitrov, M. Arnaudov, D. Topalov, J. Non-Cryst. Solids 57 (1983) 147.

93. D. Sethi, N. Jada, A. Tiwari, S. Ramasamy, T. Dash, S. Pandey, J. Photoch. Photobio B 144 (2015) 68.
94. H. Yu, J. Zeng, W. Hao, P. Zhou, X. Wen, J. Nanopart. Res. 20 (2018) 135 (1-14).
95. T.F. Khoon, J. Hasan, Z.A. Wahab, R.S. Azis, Results Phys 6 (2016) 420.
96. R. Kant, K. Singh, O.P. Pandey, Int. J. Hydrogen Energ. 33 (2008) 455.

Chapter 5 Conclusion and future scope

5.1 Conclusion

In the present study, undoped and Li, Mg, Al and Ti doped V_2O_5 materials are synthesized by melt and quench method. The structural, optical, thermal and electrical properties of $V_{2-x}M_xO_{5-\delta}$ (M= Li, Mg, Al and Ti, with variation of x) systems are studied using different experimental techniques. The structure-properties correlations of the as prepared samples and interaction study are discussed in the light of oxygen vacancies and processing parameters. The conclusions of the present study are as follows:

In the $V_{2-x}M_xO_{5-\delta}$ (M= Li, Mg, Al and Ti, x=0-0.30) system, the substitution of Mg^{2+} on the cost of V^{5+} is formed glasses above ≥10 mol% of MgO concentration. Below this concentration, V_2O_5 conditional glass former could not form the glass. While other dopants such as Li, Al, Ti do not form glasses in any concentration range of dopants. The substitution of Li^{1+} leads to form three crystalline phases i.e. orthorhombic $Li_{0.04}V_2O_5$, monoclinic $Li_4V_{10}O_{27}$ and monoclinic $Li_{0.30}V_2O_5$ whereas Al^{3+} and Ti^{4+} doped vanadium shows formation of a single orthorhombic V_2O_5 phase for all the concentration of these dopants. In addition, the highest intense diffraction peak shifts to higher diffraction angle with Li_2O, Al_2O_3 and TiO_2 dopant concentration for all the samples. This is due to the size difference between dopants and host that creates the compressive strain in the crystalline lattice.

In the $V_{2-x}M_xO_{5-\delta}$ (M= Li, Mg, Al and Ti, x=0-0.30) system, all the samples show decreasing trend in density with dopant concentration. The highest density is observed for undoped sample i.e. 3.29 gcm^{-1}. The lowest density is observed in Mg doped V_2O_5 i.e. 2.73 gcm^{-1}. The molar volume shows increasing trend in Li, Mg, and Ti doped V_2O_5 samples. On the other hand, Al doped V_2O_5 samples show decreasing trend in molar volume with dopant concentration.

FTIR and RAMAN spectra confirms the transformation of VO_5 structural units into VO_4 units on the doping of Li, Mg, Al and Ti in place of V in V_2O_5. In addition, the FTIR and Raman bands confirms the layer structure of V_2O_5 in the present samples. The appearance of new FTIR band and shifting of some FTIR bands clearly suggest the disordering in the doped samples than undoped sample. The conversion of VO_5 units in VO_4 units leads to glass formation tendency in the present samples. Moreover, this conversion also increases the hopping mechanism between V^{5+} and V^{4+}.

The lowest reflectance (13.2%) is observed for VL-0.30 sample at x=0.30. While the highest reflectance (25%) is observed for undoped samples. The optical band gap energy of undoped and doped systems lies in the wide semiconductor range (2.31-2.08 eV). All the doped samples exhibit the lower optical band gap values as compared to undoped samples (2.31 eV). The lowest optical band gap (2.08 eV) is observed for VL-0.30 sample at x=0.30.

The MgO in conditional glass former; V_2O_5 acts as a glass former in some concentration (x=0.20, 0.25, 0.30). The glass transition temperature and crystallization temperature show an increasing trend from 243-274 ˚C and 283-370 ˚C, respectively with increasing dopant concentration of Mg into V_2O_5. The TGA results confirms that all the samples exhibit reduction from V^{5+} state into V^{4+} state due to doping of various dopants (Li, Mg, Al and Ti). The TGA results also confirms that the thermal stability decreases with dopant concentration and dopants. However, Ti doped V_2O_5 samples exhibit the highest thermal stability as compared to other doped samples.

The Li-doped series show the highest conductivity 0.12×10^{2} Sm^{-1} at 450 ^{o}C whereas the Mg-doped sample shows the lowest conductivity 6.7×10^{-4} Sm^{-1} at 300 ^{o}C. The highest activation energy (0.43 eV) is found in Li-doped sample whereas the lowest activation energy (0.14 eV) is observed for Ti-doped sample. Based on the activation energies, it can be concluded that Mg and Ti doped samples exhibit the mixed conduction behaviour.

Based on interaction study, it is concluded that $V_{1.80}Mg_{0.20}O_{5-\delta}$ with AISI 430 steel (interconnect) is formed good interface as compared to $V_{1.75}Mg_{0.25}O_{5-\delta}$ with AISI 430 steel. However, extreme diffusion of C from steel and Mg from electrolyte is taken place.

These materials can be used as electrolyte for IT-SOFC due to their good conductivity range and good thermal stability in 500-600 ˚C.

5.2 Future scope

The future scope of the present work is as follows:

- In all the studied samples, the Mg doped V_2O_5 samples were formed glasses in the range of $V_{2-x}Mg_xO_{5-\delta}$ ($0.15\leq x=\leq 0.30$). Further doping of alkali metal oxides like Li_2O, K_2O and transition metal oxide like CuO in these glasses will be interested to study their electrical and structural properties to use them as electrolytes/cathodes for fuel cell/battery application.
- The photocatalytic study could be very useful due to the presence of mixed vanadium states in the studied samples as confirmed by the X-ray photoelectron spectroscopy on some selected samples.
- The performance of the as prepared samples could be checked in reducing oxygen atmosphere to study the effect of reducing atmosphere on the conductivity and stability.
- These samples should be checked for their compatibility with interconnect/cathode/anode materials.